Old Dominion University
ODU Digital Commons

Mechanical & Aerospace Engineering Theses & Dissertations

Mechanical & Aerospace Engineering

Winter 1999

Computational Modeling of Airborne Noise Demonstrated Via Benchmarks, Supersonic Jet, and Railway Barrier

Moumen Idres
Old Dominion University

Follow this and additional works at: https://digitalcommons.odu.edu/mae_etds

Part of the Acoustics, Dynamics, and Controls Commons, and the Structures and Materials Commons

Recommended Citation

Idres, Moumen. "Computational Modeling of Airborne Noise Demonstrated Via Benchmarks, Supersonic Jet, and Railway Barrier" (1999). Doctor of Philosophy (PhD), dissertation, Mechanical & Aerospace Engineering, Old Dominion University, DOI: 10.25777/g3ex-w494
https://digitalcommons.odu.edu/mae_etds/183

This Dissertation is brought to you for free and open access by the Mechanical & Aerospace Engineering at ODU Digital Commons. It has been accepted for inclusion in Mechanical & Aerospace Engineering Theses & Dissertations by an authorized administrator of ODU Digital Commons. For more information, please contact digitalcommons@odu.edu.

COMPUTATIONAL MODELING OF AIRBORNE NOISE DEMONSTRATED VIA BENCHMARKS, SUPERSONIC JET, AND RAILWAY BARRIER

by
Moumen Idres
B.S. June 1992, Cairo University, Egypt
M.S. December 1995, Cairo University, Egypt

A Dissertation Submitted to the Faculty of
Old Dominion University in Partial Fulfillment of the
Requirement for the Degree of

DOCTOR OF PHILOSOPHY

ENGINEERING MECHANICS

OLD DOMINION UNIVERSITY

December 1999

Approved by:

Oktay Baysal (Director)

Osama Kandil

Ponnampalam Balakumar

Fang Hu

ABSTRACT

COMPUTATIONAL MODELING OF AIRBORNE NOISE DEMONSTRATED VIA BENCHMARKS, SUPERSONIC JET, AND RAILWAY BARRIER

Moumen Idres
Old Dominion University
Director: Dr. Oktay Baysal

In the last several years, there has been a growing demand for mobility to cope with the increasing population. All kinds of transportation have responded to this demand by expanding their networks and introducing new ideas. Rail transportation introduced the idea of high-speed trains and air transportation introduced the idea of high-speed civil transport (HSCT). In this expanding world, the noise legislation is felt to inhibit these plans. Accurate computational methods for noise prediction are in great demand.

In the current research, two computational methods are developed to predict noise propagation in air. The first method is based on the finite differencing technique on generalized curvilinear coordinates and it is used to solve linear and nonlinear Euler equations. The dispersion-relation-preserving scheme is adopted for spatial discretization. For temporal integration, either the dispersion-relation-preserving scheme or the low-dispersion-and-dissipation Runge-Kutta scheme is used. Both characteristic and asymptotic nonreflective boundary conditions are studied. Ghost points are employed to satisfy the wall boundary condition. A number of benchmark problems are solved to validate different components of the present method. These include initial pulse in free space, initial pulse reflected from a flat or curved wall, time-periodic train of waves reflected from a flat wall, and oscillatory sink flow. The computed results are compared

with the analytical solutions and good agreements are obtained. Using the method developed, the noise of Mach 2.1, perfectly expanded, two-dimensional supersonic jet is computed. The Reynolds-averaged Navier-Stokes equations are solved for the jet mean flow. The instability waves, which are used to excite the jet, are obtained from the solution of the compressible Rayleigh equation. Then, the linearized Euler equations are solved for jet noise. To improve computational efficiency, flow-adapted grid and a multi-block time integration technique are developed. The computations are compared with the experimental results for both the mean flow and the jet noise. Good agreement is obtained. The method proved to be fast and efficient.

The second computational method is based on the boundary element technique. The Helmholtz equation is solved for the sound field around a railway noise barrier. Linear elements are used to discretize the barrier surface. Frequency-dependent grids are employed for efficiency. The train noise is represented by a point source located above the nearest rail. The source parameters are estimated from a typical field measurement of train noise spectrum. Both elevated and ground-level train decks are considered. The performance of the noise barrier at low and high frequencies is investigated. Moreover, A-weighted sound pressure levels are calculated. The computed results are successfully compared with field measurements.

ACKNOWLEDGMENTS

I would like to thank the faculty and staff of the Aerospace Engineering Department at Old Dominion University for providing me with an outstanding educational experience. Particularly, I would like to express my deep thanks and appreciation to my advisor Dr. Oktay Baysal, for introducing me to the field of computational aeroacoustics. His support, guidance, and motivation during this research were invaluable.

I would also like to recognize my dissertation committee; Dr. Osama Kandil and Dr. P. Balakumar. Their sincere effort in and out of the classroom did much to define my understanding of scientific computing. Also, their valuable comments and support were of great help to me.

Special thanks are due to my wife, Heba, for her extreme patience. She has been and continues to be a constant source of inspiration, motivation, and strength.

Finally, I would like to thank my parents for their endless encouragement and support over the years. They are responsible for there being anything positive in me.

NOMENCLATURE

English Symbols

C	Speed of sound
C_p	Specific heat constant
D_j	Jet Diameter
e, E, e'	Energy; total, mean, and perturbation
f	frequency
H^n_m	Hankel function of the nth kind and order m
h, H	Enthalpy; static and stagnation
J	Jacobian
J_m	Bessel function of the first kind and order m
k	Thermal Conductivity
M_j	Jet Mach number
n	Helical wave numer
p, P, p'	Pressure; total, mean, and perturbation
Pr, Pr_T	Prandtl number; laminar $(\mu\, C_p/k)$, Turbulent $(\mu_T\, C_p/k)$
r	Radial distance
Re	Reynolds number
R_g	Gas constant
SPL	Sound pressure level; $10\ \log(p^2_{avg}\,/\,p^2_{ref})$
St	Strouhal number; $f\, D_j/U_j$

t	time
T, T_m, T'	Temperature; total, mean, and perturbation
u, U, u'	Axial velocity; total, mean, and perturbation
v, V, v'	Radial velocity; total, mean, and perturbation
V_g	Group velocity of acoustic waves
w, W, w'	Azimuthal velocity; total, mean, and perturbation
x	Axial distance
Y_m	Bessel function of the second kind and order m

Greek Symbols

θ	Azimuthal angle
α	Axial wave number
ℓ	Mixing length
δ	Fractional time step
ω	Angular frequency; $2\pi f$
Ψ	Stream function
ρ, ρ_m, ρ'	Density; total, mean, and perturbation
μ, μ_T, μ_a	Viscosity; laminar, turbulent and artificial
ξ, η	Curvilinear coordinates
Δ_i	Dirac delta function at point 'i'

Vector Quantities

D	Dissipation vector
F	Flux vector in x-direction.
G	Flux vector in r-direction
H	Flux vector in θ-direction
Q	Conservative flow variables vector; $[\rho' \quad (\rho u)' \quad (\rho v)' \quad (\rho w)' \quad (\rho e)']^T$
q	Primitive flow variables vector; $[\rho \quad u \quad v \quad w \quad p]^T$
S	Source vector
x	Position vector

Subscripts

∞	Free stream conditions, or far field
j	Jet exit conditions, or grid point number
t	Derivative with respect to time
r	Derivative with respect to r
x	Derivative with respect to x
y	Derivative with respect to y

Superscripts

*	Dimensional quantity or fundamental solution

TABLE OF CONTENTS

Page

LIST OF TABLES....xi

LIST OF FIGURES....xii

Chapter

I. INTRODUCTION....1
  1.1 Computational Aeroacoustics....1
  1.2 Motivation and Objectives....3
  1.3 Overview of the Current Work....4
  1.4 Outline of the Dissertation....7

II. LITERATURE SURVEY....10
  2.1 Computational Aeroacoustics....10
    2.1.1 Schemes....10
      2.1.1.1 Spatial Discretization....10
      2.1.1.2 Temporal Integration....14
    2.1.2 Boundary Conditions....15
      2.1.2.1 Nonreflecting Inflow and Outflow Boundary Conditions..15
      2.1.2.2 Wall Boundary Conditions....18
  2.2 Supersonic Jet Noise....19
    2.2.1 Numerical Studies....20
    2.2.2 Experimental Studies....26
  2.3 Noise Barrier....29
    2.3.1 Experimental Studies....29
    2.3.2 Theoretical Studies....30
    2.3.3 Numerical Studies....31

III. BENCHMARK CASES....34
  3.1 Introduction....34
  3.2 Governing Equations....34
  3.3 Boundary Conditions....37
    3.3.1 Radiation Boundary Condition....37
    3.3.2 Outflow Boundary Condition....37
    3.3.3 Characteristic Boundary Condition....38
    3.3.4 Wall Boundary Condition....39
  3.4 Discretized Equations....40
    3.4.1 Linearized Euler Equations....41
    3.4.2 Nonlinear Euler....41
    3.4.3 Fully Discretized Equations....42
  3.5 Sound Source....42

Chapter Page

3.6 Linear Cases 44
  3.6.1 Pulse in Free Space 44
  3.6.2 Pulse Reflected by a Flat Wall 46
  3.6.3 Time Periodic Acoustic Wave Train Reflected by a Solid Wall 49
3.7 Nonlinear Cases 51
  3.7.1 Pulse in Free Space 51
  3.7.2 Pulse Reflected by a Flat Wall with Bump 51
  3.7.3 Oscillatory Sink Flow 52
    3.7.3.1 Mean Flow Computation 54
    3.7.3.2 Acoustic Field Computation 54

IV. SUPERSONIC JET 58
4.1 Introduction 58
4.2 Mean Flow Analysis 59
  4.2.1 Governing Equations 59
  4.2.2 Turbulence Model 61
  4.2.3 Equations in Stream Function Coordinates 62
  4.2.4 Boundary Conditions 63
  4.2.5 Computational Method 64
  4.2.6 Initial Profile 68
4.3 Stability Analysis 68
  4.3.1 Governing Equations 68
  4.3.2 Boundary Conditions 69
  4.3.3 Computational Method 71
4.4 Acoustic Field Analysis 73
  4.4.1 Governing Equations 73
  4.4.2 Computational Method 76
  4.4.3 Flow Adapted Grid 77
  4.4.4 Multiple Time Scales 79
  4.4.5 Boundary Conditions 80
    4.4.5.1 Characteristic Inflow Boundary Condition 80
    4.4.5.2 Radiation Boundary Condition 82
    4.4.5.3 Outflow Boundary Condition 82
    4.4.5.4 Centerline Boundary Condition 83
4.5 Mean Flow Results 84
4.6 Stability Results 86
4.7 Acoustic Field Results 88

V. RAILWAY NOISE BARRIER 97
5.1 Introduction 97
5.2 Railway Noise 99
5.3 Governing Equation 100
5.4 Boundary Element Method 102
  5.4.1 Formulation 102
  5.4.2 Computational Method 105

Chapter Page

5.4.2.1 Surface Approximation 105
5.4.2.2 Solution Approximation 107
5.4.2.3 Evaluation of Integrals 107
5.5 Noise Source Modeling 110
5.6 Geometry and Grid 112
5.7 Straight Single Track at Zero-Elevation 116
5.8 Straight Single Track on Elevated Deck 117
5.9 Comparison with Experiment 122

VI. CONCLUSIONS 123
6.1 Summary of the Present Work 123
6.2 Concluding Remarks 125
6.3 Recommendations and Future Work 127

REFERENCES 130

APPENDICES
A. FINITE DIFFERENCE SCHEME 139
B. EXACT SOLUTIONS OF THE LINEARIZED EULER EQUATIONS 144
C. TROUTT & MCLAUGHLIN 2.1 MACH JET 152
D. TURBULENCE MODEL 155
E. ENVIRONMENTAL ACOUSTICS TERMINOLOGY 156

VITA 158

LIST OF TABLES

Table Page

3.1 Benchmark cases. 45

4.1 Percentage error in SPL peak location. 93

5.1 Train noise source parameters. 111

5.2 Results of grid refinement study for on-ground configuration. 115

A.1 DRP coefficients for 7-point stencil fourth-order scheme. 142

A.2 Time integration coefficients. 142

A.3 Selective damping coefficients. 143

A.4 Multiple time integration coefficients. 143

LIST OF FIGURES

Figure Page

2.1 Imperfectly expanded supersonic jet. 20

3.1 Benchmark cases 35

3.2 Computational Domain. 40

3.3 H-grid (141×71 points) for initial value problems. 47

3.4 Pressure waveforms of an acoustic pulse in free space along the line y=0; numerical solution of LEE compared with the exact solution. 47

3.5 Pressure contours of an acoustic pulse reflected by a flat wall at y=0. 48

3.6 Comparison of pressure contours computed using asymptotic boundary condition and characteristic boundary condition 48

3.7 Pressure contour patterns adjacent to a solid wall generated by a time periodic acoustic source. 50

3.8 Pressure waveforms of an acoustic pulse in free space along the line y=0; linear and nonlinear solutions. 50

3.9 O-grid for flat wall with bump problem. 53

3.10 Pressure contours of an acoustic pulse reflected by a flat wall with bump 53

3.11 Time history of the maximum residual. Arrows indicate the application of the canceling-the-residual technique for accelerated convergence. 56

3.12 Mean flow solution of sink 56

3.13 Acoustic wave propagation along x-axis. 57

4.1 Schematic drawing of perfectly expanded jet flow. 58

4.2 The stream function grid for mean flow calculations 64

4.3 Multi-block time integration zones. 79

4.4 Mach number and centerline velocity of T&M Mach 2.1 jet. 85

Figure Page

4.5 Radial velocity of T&M Mach 2.1 jet. 86

4.6 Instability wave solution.. 87

4.7 Flow adapted multi-block grid for multiple time scales 89

4.8 Time history of the density signal at nine monitoring points for the axisymmetric case. 90

4.9 Density history and its spectra at two fixed field points for the axisymmetric case..91

4.10 Simulation of axisymmetric instability generated jet noise. 94

4.11 Simulation of helical instability generated jet noise. 95

4.12 Comparison of sound-pressure-level contours.. 96

5.1 Acoustic zones around a barrier. 98

5.2 Average relative octave-band spectra for railcars and rubber-tired transit cars in the open electrically powered passenger railcars. 99

5.3 Acoustic domain. 100

5.4 Surface discretization. 106

5.5 Linear element definitions. 106

5.6 Geometry of barrier and train deck. 114

5.7 Surface and domain grids.. 115

5.8 Grid refinement study for on-ground barrier at *f*=125 Hz. 116

5.9 Straight single track at zero-elevation. Pressure contours and insertion loss in dB 118

5.10 Straight single track at zero-elevation. Sound pressure levels in dBA without and with barrier and insertion loss in dBA 119

5.11 Straight single track on elevated deck. Pressure contours: (a) *f*=250 Hz, (b) *f*=1000 Hz. 120

5.12 Straight single track on elevated deck. Sound pressure levels in dBA. 121

Figure Page

5.13 Measured sound pressure levels for white noise source.. 121

C.1 Axial distribution of mean velocity profile parameter, *b*(x).................................. 152

E.1 Weighting function for A-weighted sound pressure level.............................. 157

CHAPTER I

INTRODUCTION*

1.1 Computational Aeroacoustics

The year 1952 was a very special year for aerodynamic sound research, for it was this year when Sir James Lighthill published the first of his two-part paper (Lighthill 1952, 1954) on aerodynamic sound. This paper has since been regarded as marking the birth of the discipline known as "Aeroacoustics." Lighthill's approach was to consider the exact Navier-Stokes equations and to recast them into an inhomogeneous wave equation for the fluctuations in density. The physical interpretation of Lighthill's equation is expressed as an acoustic analogy, whereby the complete flow field is replaced by an equivalent distribution of acoustic sources in an otherwise uniform medium at rest having a density and speed of sound equal to that in the uniform external flow.

Twenty years later, computational aeroacoustics (CAA) has emerged as an essential element in the study of aerodynamic sound. It is concerned with the application of computational methods to those flow problems that involve acoustic wave generation or propagation. The nature, characteristics and objectives of aeroacoustic problems are quite different from the commonly encountered aerodynamics problems. There are computational issues that are unique to aeroacoustics. These issues are:

1. Most aerodynamic problems are time independent whereas aeroacoustic problems are, by definition, time dependent. The frequency scales in aeroacoustic problems are extremely sparse. This is true due to the fact that the audible frequency range is from

---

* This manuscript is based on the style of *Journal of Fluids Engineering*.

20Hz to 20kHz. To resolve these scales accurately, severe limitations on both mesh resolution and the time integration step have to be imposed.

2. The amplitude of the fluctuations associated with the radiated sound is usually quite small compared to that of the mean flow. This large disparity presents a severe challenge to direct numerical simulation. The small magnitude of the acoustic disturbances can, perhaps, be better appreciated by noting that it is usually smaller than the error incurred in the mean flow computations. There is a fear that the acoustic solutions may be hopelessly corrupted by computational noise. This issue raises the question of whether it is more appropriate to solve for the perturbations after the mean flow has first been determined or solve the full nonlinear equations to capture the sound field directly.
3. The quantities of interest in aeroacoustics problems are the directivity and spectrum of the radiated sound in the far field. Thus, the computed solution must be accurate throughout the entire computational domain. This is in sharp contrast to aerodynamics problems where the primary interest is in determining the loads and moments acting on an airfoil or aerodynamic body. In this class of problems, a solution, which is accurate only in the vicinity around the airfoil or body, would be sufficient.
4. The distance from the noise source to the boundary of the computational domain is usually quite long. To ensure that the computed solution is uniformly accurate over such long propagation distance, the numerical scheme must be almost free of numerical dispersion, dissipation and anisotropy. If a large number of mesh points per wavelength is used, this is not difficult to accomplish but the computational cost is high.

5. A computational domain is finite in size. Because of this, radiation and outflow boundary conditions are required at its artificial boundaries. These boundary conditions allow the acoustic and flow disturbances to leave the domain with minimal reflection. It is well-known that the Euler equations support three types of small amplitude disturbances. These are the acoustic, the vorticity and entropy waves. Locally, the acoustic waves propagate at a velocity equal to the vector sum of the sound speed and the mean flow velocity. The vorticity and entropy waves, on the other hand, are convected downstream at the same speed and direction as the mean flow. Radiation boundary conditions are required along boundaries with inflow to allow the acoustic waves to propagate out without spurious reflections. Along outflow boundaries, a set of outflow boundary conditions is required to facilitate the exit of the acoustic, vorticity and entropy disturbances.
6. The imposition of wall boundary conditions is necessary whenever there are solid surfaces present in a flow or sound field. For high-order schemes, the order of the resulting finite difference equations would be higher than the original partial differential equations. The set of physical boundary conditions, appropriate for the original partial differential equations, is no longer sufficient. Thus, additional boundary conditions are needed. Also, the use of high-order scheme implies the generation of spurious numerical solutions near the wall boundaries.

1.2 Motivation and Objectives

In the last several years, the noise pollution due to automobiles on motorways, trains on railways, and airplanes landing or taking-off has become an important problem in densely populated, urban areas. An increasing need for an environmentally friendly means of transport to cope with the growing demand for mobility has been established. The railways have responded to this need by building new lines and extending their existing networks and by introducing new concepts, such as high-speed passenger transports. Also, air transportation has introduced the idea of high-speed civilian transports (HSCT). In this expanding world, noise legislation is felt to inhibit these plans.

The primary goal of the present work is to develop efficient computational methods to predict noise and evaluate noise suppression methods based on the current advances of CAA. The computational aspects mentioned in the previous section are considered thoroughly in these methods. Both finite-difference-based and boundary-element-based methods are developed. The notion is application orientation, i.e., use of the best method for a given application. Present study includes: benchmarking of computational aeroacoustics methods, supersonic jet noise prediction, and railway noise barrier evaluation.

1.3 Overview of the Current Work

Since the birth of computational aeroacoustics, benchmarking is used as a way to test and develop both schemes and boundary conditions. The idea is to use a number of model problems that mimic the real aeroacoustic problems in certain aspects. Usually, low computational effort is needed to solve such problems. In that way, different issues can be tested separately or collectively. For example, the nonreflective boundary conditions can be tested with or without the existence of nonuniformity in the mean flow. These simulations give clear cause-effect combinations. In the current work, various benchmark problems are considered. These problems are used to investigate initial or time-periodic problems, uniform or nonuniform mean flow, wall boundary conditions, cartesian or curvilinear coordinates, and linear or nonlinear waves.

For supersonic jet noise, present study focuses on a perfectly expanded supersonic round jet issuing into a quiescent ambient environment. It has been observed experimentally that the acoustic radiation from such jets is dominated by Mach waves. Turbulent structures travelling at supersonic speeds within the jet are generally thought to be responsible for these waves. Particularly, large-scale structures are identified as the major source of noise in such jets. A way to model this mechanism mathematically is to use the instability waves to perturb the jet flow at nozzle exit. Many methods have been used to solve this problem using different equations. These include the instability wave analysis, linearized Euler, full Euler, large eddy simulation, and direct numerical simulation approaches. In the present work, the linearized Euler equation (LEE) approach is adopted. This approach is computationally less demanding. It is based on neglecting both viscosity and nonlinear effects. The viscous effects can be neglected since the large scale dynamics in free shear flows are essentially inviscid. In this approach, it is assumed that the mean flow is obtained using another method. The Reynolds averaged Navier-Stokes equations are used to obtain the turbulent mean flow. An iterative implicit procedure is employed to solve this set of equations. This flow/acoustic coupling approach has many advantages as it provides both freedom and relief for each step. The mean flow is obtained by implicit solver and relieved from the high accuracy requirement of the acoustic part. For the acoustic part, the explicit dispersion-relation-preserving (DRP) scheme is used for spatial discretization in curvilinear coordinates. For the same size of computational stencil, this scheme has higher spectral resolution compared with other classical schemes. Consequently, it is capable of resolving high frequencies using a minimum number of grid points. For the temporal integration, the DRP time integration is used. The multi-block time integration technique is employed on a flow-adapted grid. This methodology achieves the best strategy both for grid demands of the mean flow and for the acoustic computations.

Since noise radiation and scattering mostly involve solutions over finite radiators or scatterers in an infinite domain, boundary element method (BEM) is the almost perfect methodology for solving such problems. This method has emerged as a powerful alternative to the finite element method (FEM), particularly in cases where better accuracy is required on the surface or where the domain extends to infinity. The most important feature of the boundary element method is that it only requires discretization of the surface rather than the volume. Hence, boundary element method mesh generation is greatly simplified compared with finite element method. This advantage is particularly important for designing, as the process usually involves a series of modifications which are more difficult to carry out using finite elements. In the present research, the boundary element method is used to determine the acoustic field around arbitrary-shaped finite structure in an infinite, two-dimensional, acoustic medium. The aim is to find acoustic radiation and scattering patterns for complex structures. This problem is of interest to workers in a number of areas including underwater acoustics, aeronautics, and civil engineers. BEM has two advantages over FDM for such a problem. First, there is no need for grid generation inside the solution domain since only the boundaries are discretized. Second, the wall boundary condition is straightforward and even absorptive walls can be considered without difficulty (compared to the tedious effort required to achieve grid orthogonality at the wall, which is needed for wall boundary condition in the finite difference method). BEM is used to solve the Helmholtz equation for the acoustic field around railway noise barrier. Linear elements are used with at least six elements per wavelength. Frequency-dependent grids are used. The effect of the elevation of the train deck is investigated.

1.4 Outline of the Dissertation

In chapter 2, the current status of the research on computational aeroacoustics is reviewed. This includes both schemes and boundary conditions. Previous experimental and numerical investigations on supersonic jet noise are reviewed. Various numerical approaches are discussed. Finally, experimental, theoretical and numerical studies of noise barriers are reviewed.

The finite difference method is established in chapter 3. The generalized coordinates formulation is adopted. Assuming uniform mean flow, the conservative form of the linearized Euler equations is obtained. The full Euler equations are also considered with isentropic source terms. Nonreflecting and wall boundary conditions equations are presented. The finite difference method is validated through a series of benchmark problems. These include initial value problems and time periodic problems. A Gaussian curve is used to represent the acoustic source amplitude. The efficiency of nonreflecting boundary conditions is tested in the presence of mean flow. Straight and curved walls are introduced to test the wall boundary conditions in Cartesian and generalized coordinates.

The numerical results are studied and compared with the analytical or theoretical solutions.

Chapter 4 is devoted to supersonic jets. The boundary layer approximation of the Reynolds averaged Navier-Stokes equations is introduced. The resulting equations are transformed to the stream function coordinates. An iterative implicit method is proposed to solve the mean flow equations. Jet stability analysis is based on the compressible Rayleigh equation. This equation is solved in an iterative manner using Runge-Kutta method. A flow-adapted grid technique is proposed. A multi-block time integration is also demonstrated. The conservative form of the linearized Euler equations is considered to compute noise propagation. Characteristic boundary conditions are used along the jet inlet. Outflow boundary condition is used at the downstream boundary, radiation boundary condition is used at far field boundary, and symmetry boundary condition is implemented at centerline. Mach 2.1 jet simulation is presented. The calculated mean flow is compared with the experimental/analytical results. Then, Rayleigh equation is solved for the axisymmetric and helical instability waves. These waves are used to excite the jet. The predicted sound field is compared with the experimental results.

The analysis of railway noise barrier is introduced in chapter 5. The boundary element method is formulated based on linear elements. The train noise spectrum is used to estimate the source strength and frequency content. Both zero elevation and elevated structures are considered. Surface discretization is based on the frequency of the source. Elements of varying length are used to avoid a steep change in element lengths at corners. Contours of the sound pressure levels and insertion loss are presented.

Finally, chapter 6 concludes the present study with general remarks and recommendations for future work.

CHAPTER II
LITERATURE SURVEY

2.1 Computational Aeroacoustics

Computational aeroacoustics are concerned with the application of the computational methods to compute sound generation and propagation. Since the early seventies, this field has been constantly growing. The special characteristics of the acoustic waves, being of small amplitude, non-dispersive, and non-disspative, represent a tough challenge for any computational method. A special family of schemes and boundary conditions has been developed to tackle these problems. The resurgence of the noise problem due to the expansion in transportation networks has encouraged different researchers to contribute to this field. In this section a review of the current status of the CAA is introduced. This includes both schemes and boundary conditions.

2.1.1 Schemes

2.1.1.1 Spatial Discretization

It has been recognized that numerical schemes that have minimal dispersion and dissipation errors are desirable, since the acoustic waves are non-dispersive and non-dissipative in their propagation. In this regard, it has appeared that high-order schemes would be more suitable for computational acoustics than lower-order schemes since the former are usually less dispersive and less dissipative. In recent years, a number of high-order schemes have been developed. These include the 2-4 MacCormack scheme by Gottleib and Turkel (1976), high-order essentially non-oscillatory (ENO) schemes by

Atkins (1991), compact finite difference schemes by Lele (1992), and explicit dispersion-relation-preserving (DRP) scheme by Tam and Webb (1993).

The most commonly used approach to construct a highly accurate finite difference scheme is to use Taylor expansion on a large stencil and then increase the order of the truncation errors. However, recent studies expose a conflict between the order of accuracy of a high-order finite difference scheme and its resolution capability. Lele (1992) was one of the first investigators to improve the resolution capability of a high-order compact difference scheme at the cost of its order of accuracy. However, his wave number fit approach is somewhat empirical. Later, Tam and Webb (1993) modified finite difference schemes by an integrated error minimization method. Kim and Lee (1996) further extended this least-square-type technique to compact difference schemes, Li (1997) to upwind-biased difference schemes, Lockard et al. (1995) to ENO schemes, and Hixon (1997) to MacCormack schemes. As a result, these so-called optimized difference schemes have better spectral resolution property than high-order conventional difference schemes with the same stencil size.

The philosophy behind the DRP schemes is that the dispersion relations of the partial differential equations are reproduced in the discretized problem. Tam and Webb (1993) have developed a discretization method based on this idea. They used the Fourier transform to find the dispersion characteristics of the finite difference approximation. Then, the error defined as the difference between the numerical wave number and the exact wave number was minimized over a specified range of wavelengths. They applied this methodology to obtain the fourth-order DRP scheme, which has a 7-point stencil. A sequence of numerical simulations has been carried out to test the effectiveness of this scheme. This includes an initial acoustic pulse, vorticity pulse, or entropy pulse in uniform flow. The computed solutions agree very favorably with the exact solutions.

Baysal et al. (1994) investigated the use of a second-order scheme to solve wave propagation problems. They evaluated various methods to suppress cavity noise. In 1996, Kaushik and Baysal used DRP scheme to solve linearized, two-dimensional, Euler and Navier-Stokes equations for the acoustic wave propagation. They investigated the effects of the choice of the boundary conditions, effects of viscosity and low-storage time integration. Baysal and Kaushik (1996) solved the wave scattering problem using the DRP scheme. They considered the sound field generated by a propeller scattered off by the fuselage of an aircraft. To idealize the problem, the fuselage was assumed to be a circular cylinder and the noise generation by the propeller was represented by a line source. Vanel and Baysal (1997) used the DRP scheme to solve wave propagation problems. They investigated different methods to obtain the spectral characteristics of the time-domain data. They concluded that the spectral method had a significant effect on the frequency spectrum.

Compact finite difference schemes offer a means of obtaining high-order approximations to differential operators using narrow stencils. This is achieved by treating the sought derivatives as unknowns and solving a system of equations for them. Typically, the resulting matrices are tridiagonal or pentadiagonal and can be efficiently solved. A detailed exposition of compact schemes and derivation can be found in Vichenevetsy and Bowles (1982). Lele (1992) developed compact finite difference stencils for the first-, second-, and higher-order derivatives. He successfully applied his schemes to solve the shock wave problem and the compressible mixing layer evolution problem.

The ENO method is able to capture shock waves and remain formally high order in smooth regions of the flow through a stencil-shifting process. Hence, a complete set of stencils, varying from fully-left-shifted to fully-right-shifted, should be available to represent the derivative. The algorithm that chooses the stencil is designed to select a preferred stencil whenever the solution is smooth. Lockard et al. (1995) developed high-bandwidth operators to be used with the ENO method. The spatial operator of a standard sixth-order scheme was replaced by a third-order high-bandwidth operator. They compared numerical and analytical solutions for the model problems of plane-wave propagation and sound generation by an oscillating sphere. They discovered that the high-bandwidth operator performs better than the standard operator with the same stencil size primarily when the propagation distance is long relative to the wave length.

Sankar et al. (1993) evaluated several schemes for use in CAA. The performance of the fourth-order MacCormack scheme was considered satisfactory because of its accuracy, speed, and simplicity. The scheme is an extension by Gottlieb and Turkel (1976) of the classical second-order accurate MacCormack (1969) scheme. It is second-order accurate in time, but fourth-order accurate in space. In this scheme, the operator is split into several one-dimensional operators and applied in a symmetric way to avoid biasing of the solution. Hixon et al. (1995a, 1995b, 1997) and Mankbadi et al. (1995, 1998) have used this scheme to compute jet noise successfully.

2.1.1.2 Temporal Integration

It turns out that the requirement of minimum numerical damping to the physical acoustic wave solution sometimes imposes an even more stringent condition on the size of the time marching step than numerical stability. Since implicit time integration methods are usually used for the benefit of large time steps, these methods are rarely used in computational aeroacoustics. Also, the computational cost per time step for implicit time integration is larger than that for explicit method.

Rather than using the classical explicit schemes, a family of optimized schemes has been developed to reduce the dispersion and dissipation errors of the propagating waves. These include the DRP time integration scheme developed by Tam and Webb (1993), and the low dissipation and dispersion Runge-Kutta (LDDRK) schemes developed by Hu et al. (1994).

Tam and Webb (1993) optimized the Adam-Bashforth type multi-step time integration scheme to develop a third-order time integration scheme. The optimization was carried out to preserve the numerical frequency of the original partial differential equation. The effective frequency of the numerical scheme is obtained by the Laplace transformation of the discretized equation. They conducted a series of numerical simulations of an initial pulse in uniform flow to demonstrate the effectiveness of this scheme.

Hu et al. (1994) have shown that when the classical Runge-Kutta schemes are used in wave propagation problems using high-order spatial finite difference, time steps much smaller than that allowed by the stability limit are necessary in the long time integrations. They chose the coefficients of the Runge-Kutta schemes so as to minimize the dissipation and dispersion errors of the propagating waves. Using this method, larger time steps are attainable without suffering dispersion or dissipation. Optimization of both single-step and two-step alternating schemes were considered. They demonstrated the capability of their scheme through a sequence of benchmark problems. The scheme proved to be effective and accurate.

2.1.2 Boundary Conditions

In a typical CAA problem, one often encounters two types of boundaries. Because a finite computational domain is used, there are external boundaries. On these boundaries, boundary conditions simulating the solution outside the computational domain are to be imposed. These are typically either the nonreflecting or the outflow boundary conditions. Inside the computational domain, there may be internal boundaries. On these boundaries, boundary conditions simulating the presence of an object or surface with specific acoustic characteristics are to be applied. The solid wall boundary condition belongs to this category.

The development of numerical boundary conditions for CAA has continued for many years. A recent review was given by Givoli (1991) for the wave equation, and by Tam (1997) and Lele (1997) for Euler and Navier-Stokes equations.

2.1.2.1 Nonreflecting Inflow and Outflow Boundary Conditions

It is well known that in a uniform mean flow the linearized Euler equations support three types of disturbances. They are the acoustic waves, the vorticity waves and the entropy waves. The acoustic waves propagate at sound speed relative to the mean flow.

The vorticity as well as the entropy waves are convected downstream by the mean flow. At an inflow boundary, the only outgoing disturbances are acoustic waves. At an outflow boundary, in addition to the acoustic waves, both vorticity and entropy waves are convected out by the mean flow. Due to this distinctive difference, the inflow and outflow boundaries have different types of boundary conditions. There have been many proposed nonreflecting boundary conditions based on different ideas. These could be summarized as follows:

1. Characteristic Based Boundary Conditions

Thompson (1987, 1990) and Poinsat and Lele (1992) proposed to treat the problem as one-dimensional near the boundary of the computational domain. The coordinate in the direction normal to the boundary is taken as the spatial coordinate. For Euler equations in one dimension, a full set of characteristics can easily be found. They used these characteristics to form boundary conditions involving only outgoing waves. However, in two- or three-dimensional problems, there are no true characteristics. The characteristics boundary conditions work well for acoustic disturbances incident nearly normal on the boundary. They do not give good results at grazing angle of incidence or when there is a strong mean flow tangential to the boundary.

2. Boundary Conditions Derived from Asymptotic Solutions

Bayliss and Turkel (1982), Hagstrom and Hariharan (1988), and Tam and Webb (1993) derived radiation and outflow boundary conditions by means of the asymptotic solutions of the governing equations. Numerical experiments have shown that these boundary conditions are extremely effective, provided that the sources are sufficiently far from the boundary of the computational domain.

3. Absorbing Boundary Conditions

A different idea to deal with exterior boundary conditions is to use an absorbing layer. An absorbing layer usually consists of 10 to 20 mesh points in which damping terms are introduced to damp out the incident waves. The development of absorbing boundary conditions has been pursued by many investigators including Engquist and Majda (1977), Higdon (1986), and Kosloff and Kosloff (1986). In a more recent work, the idea of absorbing the incident wave was extended and refined by Colonius et al. (1993) into a sponge and exit zone with grid stretching and filtering. A somewhat different approach was suggested by Ta'asan and Nark (1995). They artificially modified the governing equations in a buffer zone so that the mean flow becomes supersonic in the outward direction. This idea was further extended by Hayder and Turkel (1996) to the full Euler equations in conservation form. Most recently Freund (1997) proposed a zonal approach combining the absorbing boundary idea and the technique of Ta'asan and Nark (1995).

4. Perfectly Matched Layer

In an absorbing layer, the addition of artificial damping terms to the governing equations for the purpose of damping out the incidence disturbances also can lead to substantial reflections at the interface. Berenger (1994), in his work on computational electromagnetics, found that it is possible to formulate an absorbing layer without reflection. Such a layer has come to be known as a perfectly matched layer (PML). Hu (1996a) was the first to apply PML to acoustic problems governed by the linearized Euler equations with uniform mean flow. He has since extended his work to nonuniform flow and for the fully nonlinear Euler equations (Hu 1996b). One advantage of the PML method is that if the mean flow is uniform, the boundary can be put very close to the acoustic sources. If the mean flow is nonuniform, the PML equations are unstable and damping terms are added to suppress spurious waves.

2.1.2.2 Wall Boundary Conditions

For high-order finite difference schemes, the order of the finite difference equation is higher than the original partial differential equation. Spurious solutions, which have no relationship to the original partial differential equation, are supported by the difference equation. These spurious solutions are unavoidably excited at the wall. There are two major difficulties in developing wall boundary conditions for high-order finite difference schemes. First, high-order finite difference equations require additional boundary conditions, beyond the physical boundary conditions of the original problem, to define a unique solution. Second, in the discretized system, each flow variable at either an interior or boundary mesh point is governed by an algebraic equation (discretized form of the partial differential equation). The number of unknowns is exactly equal to the number of equations. Thus, there will be too many equations and not enough unknowns if it is insisted that the boundary conditions at the wall mesh points are satisfied also.

Tam and Dong (1994) have suggested a method that uses ghost point to construct a wall boundary condition. They proposed to use backward difference stencils as the wall is approached. This eliminates the need for extra boundary conditions. To provide enough unknowns to enforce the physical wall boundary conditions as well as to allow the discretized governing equations to be satisfied at mesh points on the wall, they suggested including ghost values at ghost points. Ghost points are mesh points immediately outside the computational domain. The number of the ghost values to be included is equal to the number of physical wall boundary conditions. The effectiveness of these numerical boundary conditions, in simulating the presence of a solid wall adjacent to an inviscid or viscous fluid, was tested by comparing the results of numerical simulations with the exact solutions. They considered the reflection of an acoustic source by a solid wall, oscillating viscous boundary layer adjacent to a solid wall and diffraction of acoustic waves around a thin, flat plate. Good agreement was reported for all the test cases.

Chung and Morris (1995) proposed an Impedance Mismatched Method (IMM) to enforce the wall boundary condition. In this method, solid bodies are replaced by a new fluid medium with a large characteristic impedance, ρC. When the characteristic impedance of the new fluid medium is infinite, it can be shown that the incident waves are completely reflected. The advantage of the IMM method is that the entire computational domain including the solid bodies can be regarded as a continuous fluid region making the programming very simple. However, unlike the ghost point method, the IMM can not be used for viscous problems.

2.2 Supersonic Jet Noise

Supersonic jet noise consists of three main components: turbulent mixing noise, screech tones, and broadband shock associated noise, the latter two occurring in imperfectly expanded jets. Figure 2.1 shows the flow field structure for imperfectly expanded supersonic jet. Expansion fans and oblique shocks form the shock cell structure shown in this figure. At high speed, mixing noise is dominated by Mach wave emission which arise when turbulent eddies in the jet travel with a velocity which is supersonic relative to the surrounding medium. Screech is a discrete tone emitted by imperfectly expanded jets. It has a significant upstream propagation component and thus can cause damage to the engine nozzle structure. Screech is thought to be generated and sustained by a resonant feedback loop that comprises the following elements: (a) sound generated by passage of eddies through shock cells; (b) upstream propagation of the sound towards the nozzle; and (c) coupling of the sound with the shear-layer instability.

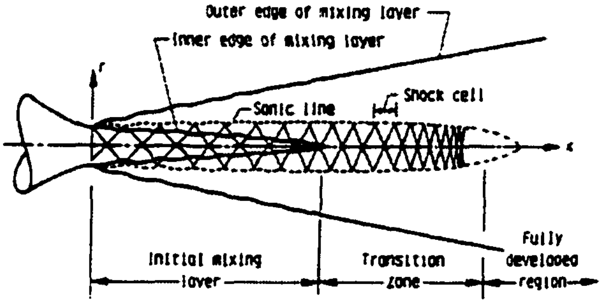
Outer edge of mixing layer
Inner edge of mixing layer
r
Sonic line
Shock cell
x
Initial mixing layer
Transition zone
Fully developed region

Figure 2.1 Imperfectly expanded supersonic jet.

2.2.1 Numerical Studies

The prediction of the sound, which is generated by jet flows, has been extensively researched since Lighthill (1952, 1954) first proposed the acoustic analogy for turbulent jets. In his acoustic analogy, the jet flow is replaced by a distribution of acoustic sources (stationary or convected) in an ambient fluid at rest. Lighthill's equation is 'exact' (it is rearrangement of the Navier-Stokes and continuity equations) but it is a single equation in several dependent variables, and only yields predictions if the source terms are known a priori. Detailed experimental measurements of the source term and its retarded time would be very difficult and have never been performed. Thus, simplifying assumptions about the forms of the source terms have been used to predict scaling lows and the directivity of the acoustic field. The mathematical difficulty stems in part from the inability of the acoustic analogy to extract the sound generation problem from the interaction of acoustic waves with turbulence and the mean flow. It is possible to overcome some of these difficulties by moving certain terms from Lighthill's source term to the left-hand side of the equation, as was done by Lilley (1974). Since the acoustic far field depends on a global solution to the problem, this approach does not lead to a rigorous first-principles method for calculating the sound field as pointed out by Goldstein (1984). In that case, one must again regard the source term as independently known.

Other approaches to the prediction of jet noise have been developed based on utilizing different forms of the governing equations. This includes the instability wave analysis (Liu 1974, Morris and Tam 1979, Tam and Burton 1984a, 1984b, and Crighton and Huerre 1990), the linearized Euler equations (LEE) approach (Hixon et al. 1995a, 1995b, 1996, and Mankbadi et al. 1995a, 1998), non-linear disturbance equation (NLDE) approach (Bangalore et al. 1996, and Morris et al. 1998), full Euler equations approach (Viswanathan and Sankar 1995), large eddy simulation (LES) approach (Mankbadi et al.

1994, 1995, and Shih et al. 1998), and direct numerical simulation (DNS) approach (Lele 1989, Scott 1991, 1992, Mitchell et al. 1996, and Colonius et al. 1997).

Tam and Burton (1984a) used the method of matched asymptotic expansion to solve the linearized stability equations of a supersonic two-dimensional mixing layer. In the second part of their work (Tam and Burton 1984b), they applied this technique to predict the mixing noise of an axisymmetric jet. To test the validity of the theory, numerical results of the solution were compared with the experimental measurements of Trout (1978) and Trout & McLaughlin (1982). Two series of comparisons at Strouhal number 0.2 and 0.4 for a Mach-number 2.1 cold supersonic jet were conducted. Good overall agreements between the calculated results and the experimental measurements were found.

Mankbadi et al. (1995a) used the linearized Euler equations approach to predict supersonic jet noise. The mean flow was obtained by analytical curve fitting of the experimental results of Troutt & McLaughlin (1982). The 2-4 MacCormack scheme is used to solve the linearized Euler equations. At the inlet, the jet was excited by the instability waves which were obtained from the solution of the Orr-Sommerfeld equation. A comparison of the numerical results with the experimental data of Mach-number 2.1 jet at Strouhal number of 0.2 showed good agreement. Parametric studies have been performed to investigate the effects of jet temperature by Hixon et al. (1995b). It was concluded that as the core temperature of the jet is increased, the angle of emission becomes steeper. The effect of random disturbances has been studied by Hixon et al.(1996). It was found that the random input disturbance results were closer to the experimental data than the instability-wave model.

Morris et al. (1997) used the nonlinear disturbance equations in conservative form to predict jet noise. The mean flow was obtained by the solution of the Reynolds averaged Navier-Stokes (RANS) equations. The fourth-order DRP scheme was used for spatial discretization and the fourth-order classical Runge-Kutta scheme for temporal integration. A parallel programming technique was employed. Acoustic results were presented for a perfectly expanded supersonic axisymmetric jet (Troutt & McLaughlin 1982 case) under harmonic and random inlet excitations. Although good agreement between the predictions and experimental data was reported, the effect of the nonlinear terms was not identified. Moreover, they dropped the mean flow source terms in the nonlinear disturbance equations. Morris et al. (1998) applied the same technique to circular and rectangular supersonic jet noise predictions. They conducted simulations of two circular jets at $M_j= 1.66$ and 2.1 and a rectangular jet at $M_j=1.66$ and with an aspect ratio of 2. The predictions were compared with the Kirchhoff method results and with experimental measurements. The simulations overpredicted the sound pressure levels by 4 to 5 dB. The relative changes were well predicted. When the simulations were performed on coarser grids, the predicted noise was consistent with the measured noise. They argued that the specification of the inflow disturbances and their introduction into grids of different refinements could affect the noise field.

Viswanathan and Sankar (1995) used a fluid/acoustic coupling approach to predict noise radiated from axisymmetric supersonic jets. The mean flow was established with the solution of the Reynolds averaged Navier-Stokes equations in the first step. Subsequently, the flow was excited using instability waves and the acoustic field was captured through the solution of full Euler equation. They used an implicit scheme for the mean flow calculations and the 2-4 MacCormack scheme for the noise calculations. A finite volume technique was adopted. They considered a supersonic jet at Mach 2 and different temperatures. The effect of the jet temperature on the peak directivity was correctly demonstrated; i.e. as the jet temperature increases, the peaks are shifted up.

A large eddy simulation (LES) approach was used by Mankbadi et al. (1994) to predict the near field noise source for a supersonic jet. In this approach, the Navier-Stokes equations are filtered into large-scale components, which are calculated directly, and small-scale components, which are modeled. The Smagorinsky's model was used to represent the effect of the subgrid-scale turbulence stresses. The 2-4 MacCormack sheme was used. The time-dependent near field was then used to calculate the far field noise using Lighthill's theory. They considered a supersonic jet at Mach number 1.5 with harmonic or random excitation (*St* from 0 to 1) at the inlet. The difficulties that arise from the nonconvergence of the integrals, in the Lighthill's formula, due to noncompactness of the source were discussed. In a subsequent work, Mankbadi et al. (1995) used LES technique to capture the near and far field noise directly. They considered a supersonic jet at Mach number 2.1 excited at Strouhal number 0.2. The predicted acoustic field was in qualitative agreement with the observation. They pointed out that the small-scale modeling needs crucial attention, not only for adequate spreading of the jet, but also for extension to acoustic predictions. Recently, Shih et al. (1998) replaced the Lighthill's formula by Kirchhoff's method to capture the far field noise from the time-dependent data of the near field. The nonlinear sound source in the near field was identified using the LES approach. A full three-dimensional computation was carried out for Mach 2 heated supersonic jet. Qualitative agreement with the experimental data was reported.

Lele (1989) performed direct numerical simulation of the time-dependent Navier-Stokes equations to compute jet noise. He used the sixth-order accurate compact differencing schemes to investigate certain properties of unsteady shear layers and sound generation. In particular, the behavior of isolated vortex structures and interacting vortices have been examined. Later, Scott (1991, 1992) considered the time-dependent Navier-Stokes equations for jet noise calculations. He used a 2-2 MacCormack scheme. Particular attention has been directed toward specific unsteady flow features that are known to be among major contributors to noise production in supersonic jets. These include production and subsequent interaction of large-scale coherent structures, the presence of shocks and their interaction with the shear layer, and the turbulent behavior of jet flow. Both high subsonic and supersonic jets were considered. Comparison of the computed results with the experimental data have demonstrated that the numerical procedure gives a reasonable representation of the unsteady flow features which have been identified as noise source mechanism.

Colonius et al. (1997) used the direct numerical simulation of the Navier-Stokes equations to compute both the near field region and a portion of the acoustic far field of a plane mixing layer. The acoustic analogy due to Lilley (1974) was solved with acoustic sources determined from the near field data. They considered two streams of Mach numbers 0.5 and 0.25 at low Reynolds number. The predictions from the acoustic analogy were found to be in good agreement with the acoustic field from DNS. It was concluded that the acoustic sources have the form of modulated wave packets that is best represented by a quadrupole terms. They pointed out that the presence of flow-acoustic interactions in the computed source terms causes the acoustic field predicted by the acoustic analogy to be very sensitive to small changes in the description of the source.

Recently, Owis (1999) used a coupled approach to compute the noise from subsonic and supersonic jets. The near field was obtained using the unsteady Navier-Stokes equations. The propagation of the acoustic waves in the far field was captured using the wave equation. The MacCormack scheme was adopted. It was shown that the perfectly matching layer method is the best type of non-reflecting boundary condition. He considered five cases at different Mach numbers and Reynolds numbers. The results were compared with other methods and showed a good agreement.

2.2.2 Experimental Studies

Lau et al. (1979) have conducted a survey of the jet flow field at Mach 0.28, 0.9, and 1.37 under ambient temperature conditions. Radial and centerline distributions of the axial and radial, mean and fluctuating velocities were obtained. The distributions indicated a decrease in the spreading rate of the mixing layer with increasing Mach number and a corresponding lengthening of the potential core. The results further indicated that these two parameters vary with the square of the jet Mach number.

An experimental investigation of the flow and acoustic properties of a moderate Reynolds-number (Re=70000), Mach number 2.1, axisymmetric jet has been performed by Troutt and McLaughlin (1982). The results of the flow-field measurements demonstrated that the jet shear annulus was unstable over a broad frequency range. The initial growth rates and wavelengths of these instabilities, as measured by a hot wire, were found to be in reasonable agreement with linear stability theory predictions. This conclusion was previously established in a series of low-Reynolds-number supersonic jet experiments by McLaughlin et al. (1975, 1977). The potential core of the jet was found to be most responsive to excitation at frequencies near a Strouhal number of 0.3. The acoustic near field was characterized in terms of sound pressure levels and directivity for both natural and excited jets. It was determined that the large-scale flow disturbances radiate noise in a directional pattern centered about 30° from the jet axis. It was also determined that the large-scale components of the near field sound are made up predominately of axisymmetric and helical modes. The dominant noise generation mechanism was described to be a combination of Mach-wave generation and a process associated with the saturation and disintegration of large-scale instability.

Oertel (1979, 1982) carried out a series of experimental studies on the instability waves of high-speed jets. In his experiments, the jets formed by hot or cold gases issued through convergent-divergent nozzles mounted at the end of a shock tube. By using a novel optical technique, he was able to identify three families of waves in his jets. Each family of waves had its distinct characteristics and propagation speed. Associated with the first set of waves was a strong acoustic near field. In the region immediately outside the jet, the waves appeared as nearly parallel lines trailing the flow of the jet. The second family of waves had a near acoustic field in which the wavefronts are almost normal to the jet boundary. The propagation speed of this set of waves was found to be less than that of the first set. The third family of waves, unlike the first two sets of waves, appeared to have no near field. The waves seemed to be confined primarily inside the jet. Within the jet the waves displayed a characteristic cross-hatched pattern.

Panda et al. (1997) investigated the screech characteristics of unheated, supersonic, underexpanded jets issuing from a circular, a 5:1 aspect ratio rectangular, and a 3:1 aspect ratio elliptic nozzle over the nominal range, $1.1 \leq M_j \leq 1.9$. The shock spacing in the jet shear layer was measured using the light scattering properties from a narrow laser beam. The shock spacing was compared with the wavelength of the standing wave system that wraps around the jet. It was found that the two length scales (shock spacing and standing wavelength) are close for all the nozzle geometries and the jet operating conditions. For a given nozzle geometry, the shock spacing and standing wavelength increased when M_j was increased. It was concluded that the difference between the standing wavelength and the shock spacing would be dictating the efficiency of the feedback loop in generating sound.

Recently, Debiasi and Papamoschou (1999) studied the noise characteristics of perfectly and imperfectly expanded, low-density supersonic jets. Application of a subsonic coflow at conditions designed to prevent emission of Mach waves from the jet was also investigated. The fully expanded jet velocity ranged from 400 m/s to 1010 m/s and the fully expanded jet Mach number ranged from 1.25 to 1.75. The coflow was supplied at 200 m/s or 400 m/s, depending on the test case, and was designed for Mach wave elimination condition. Noise spectra were obtained at many radial and polar positions around the jet exit. They concluded that the peak noise emission in the far field is insensitive to nozzle exit pressure and depends solely on the values of the fully expanded velocity and Mach number. In the near field, imperfect expansion created screech and broadband shock noise. Addition of the coflow reduced the near field screech peaks by 5-10 dB. The coflow suppressed Mach wave emission most effectively in jets with fully expanded velocity in the range of 600-700 m/s, providing reductions as much as 18 dB in the mid- and high-frequency spectral components of the far field.

2.3 Noise Barrier

Many investigations have been carried out for the purpose of predicting sound levels behind barriers. The numerous publications on diffraction and noise reduction by barriers can be roughly divided into three categories. The first deals with experiments measuring either scaled models or barriers under normal environmental conditions. The second comprises theoretical studies presenting analytical expressions or asymptotic expansions for the sound pressure. The third gives results of the numerical approximations of the complete initial-boundary value problem.

2.3.1 Experimental Studies

May and Osman (1980) have studied the relative acoustical performances established by scale model testing of barriers in typical highway situations. They considered barriers of different shapes; thin, wide, T-profile, cylindrical top, corrugated, inclined, Y-profile, and arrow-profile. The effect of sound absorptive material was also studied. The highway situations involved a single barrier with a receiver on the opposite side of the highway, and parallel barriers, one on each side of the highway. Higher noise reduction was found for wide-top barrier, especially those of T-profile. Absorptive side treatment was found to have a small effect.

More recently, Duhamel et al. (1998) measured the active noise control efficiency around noise barriers in an outdoor experiment around a real wall. The study was limited to stationary noise, either harmonic or pink noise, created by a loudspeaker and controlled with the help of loudspeakers as secondary sources. The purpose of their experiment was to find the space and frequency domains over which the control is efficient. They compared their results with values calculated by the boundary element method. They concluded that the controlled space domain can extend on distances as large as 40m on the axis perpendicular to the barrier. This domain looked like an angular sector with an opening angle function of the frequency. So the control can be more efficient on very large zones if we go far enough from the barrier.

Certainly, these measurements give the most objective results, but in many cases they are influenced by the environment (temperature, wind speed, and turbulence) at which the experiment is performed. Moreover, it has been discovered that the instrumentation and the measurement technique can also produce errors.

2.3.2 Theoretical Studies

In order to obtain more generality, e.g. different barrier geometries, several theories have been developed differing mainly in the theoretical approach to diffraction and in the model for ground impedance. Among the many existing works in this field are Keller's geometrical theory (Keller 1962), Kirchhoff-Fresnel diffraction theory (Elmore and Heald 1969), Thomasson's theory based on Babinet's principle (Thomasson 1977), the edge-integral diffraction theory based on the Young-Rubinowicz formula (Embleton 1980) and a modification of MacDonald's diffraction theory (Isei 1980). From these theories, relatively simple analytical expressions are derived which approximate the diffracted field in the shadow region behind the barrier.

Isei et al. (1980) have compared the results of these five theories with each other and with the field measurements. They found that these theories agree reasonably well with each other and with point source measurements. In particular, the calculated interference spectra of barrier attenuation exhibit the expected changes in shape and frequency as the obliquity of incidence and acoustical properties of the ground and barrier are changed.

The applicability of the approximating analytical expressions in an actual situation is not very obvious, and, all these analytical expressions lead only to approximate solutions with unknown accuracy. Moreover, since these formulae contain only a small number of parameters, more complicated situations can not be analyzed.

2.3.3 Numerical Studies

It is well known that the propagation of acoustic waves is governed by the scalar wave equation or, if harmonic excitations are considered, by the Helmholtz equation, where reflections, scattering and diffractions are correctly characterized by boundary conditions. Since noise radiation or scattering mostly involves solutions over finite radiators or scatterers in infinite domains of homogeneous media, boundary integral equations are the almost perfect methodology for solving such problems. Several review articles on the application of boundary element method to solve noise problems are available, e.g. Shaw (1988) and Shaw (1991). A more general theory for the integral equations was introduced by Farassat (1996). He used generalized functions to develop aerodynamics and aeroacoustics governing equations. One of the most useful aspects of this theory is that discontinuous functions can be handled as easily as continuous or differentiable functions.

For time harmonic acoustic wave propagation problems, the first paper using numerical solutions based on a boundary integral equation, i.e. the Helmholtz equation, was that of Banaugh and Goldsmith (1963). Among the many existing papers in this field, only a few, concerned with acoustic radiation problems and related to this work, will be mentioned here.

Habault (1985) presented the solution of some diffraction problems, e.g. the diffraction of sound due to cylindrical and spherical sources by an inhomogeneous plane. Amini and Wilton (1986) investigated the efficient determination of acoustic fields around arbitrary-shaped, finite structures in an infinite three-dimensional acoustic medium. They discussed the different ways to overcome the non-existence and non-uniqueness problems associated with classical integral equation formulations of this problem. A class of numerical approximation schemes was developed. They applied their schemes to a number of test problems. The choice of the parameters of the method was critically considered, in particular, the use of higher-order approximations to the unknown boundary function. They concluded that increasing the order of the polynomial approximation is generally the most efficient method of obtaining more accurate results.

Hothersall et al. (1991) used the boundary element approach to obtain the insertion loss for T-, Y- and arrow-profile barriers. The effect of absorptive coating was considered. Results for the mean insertion loss over a range of receiver positions for a broadband source were presented. They concluded that the introduction of absorbing upper surfaces produces a significant increase in insertion loss. Also, the Y- and arrow-profiles perform less efficiently than the T-profile in most conditions.

Antes (1991) investigated several two- and three-dimensional environmental noise problems using time domain and frequency domain boundary element methods. Particularly, he successfully predicted the noise from moving noise sources like that of single cars or flying airplanes. He modeled the noise of the vehicle engine and tires by uniform intensity line source. The numerical modeling used linear approximation functions and elements of equal length, but the discretization, i.e. the number and length of elements was made dependent on the wavelengths of the sound. Six elements per wavelength were used. A 2-D edge and wedge-shaped barriers were considered. It was shown that the insertion loss of the barrier is higher for higher frequencies. When the ground behind the barrier was assumed to be absorbent, the noise intensity near the ground was reduced.

CHAPTER III

BENCHMARK CASES

3.1 Introduction

Benchmark problems are "model problems" where methods can be tested and validated through rigorous comparisons with analytical or theoretical solutions. A number of these problems are considered (refer to figure 3.1). This includes an initial pulse in free space, an initial pulse reflected from a flat or a curved wall, a time-periodic train of waves reflected from a flat wall, and an oscillatory sink flow. In section 3.2, linear and nonlinear Euler equations are considered in generalized curvilinear coordinates. Boundary conditions are discussed in section 3.3. Discretized forms of the governing equations are developed in section 3.4. Sound source modeling is discussed in section 3.5. The results for linear and nonlinear cases are demonstrated in section 3.6 and section 3.7 respectively.

3.2 Governing Equations

The governing equations for the acoustic perturbations can be derived from the unsteady compressible Euler equations. Let ρ^*, (u^*,v^*), and p^* denote the density, velocity components, and pressure respectively. Let ρ_∞, C_∞ denote the free stream density and speed of sound, respectively, and L_{ref} be a reference length dimension in the flow. The various flow variables are nondimensionalized as follows:

$$\rho=\frac{\rho^*}{\rho_\infty},\quad p=\frac{p^*}{\rho C_\infty^2},\quad (u,v)=\frac{(u^*,v^*)}{C_\infty},\quad (x,y)=\frac{(x^*,y^*)}{L_{ref}},\quad t=\frac{t^*}{L_{ref}/C_\infty}$$

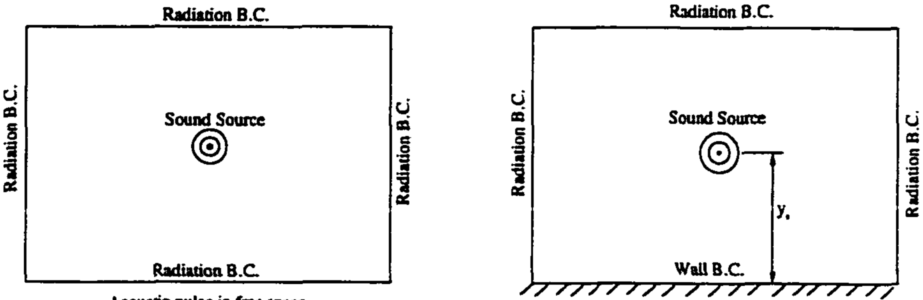
Radiation B.C.
Radiation B.C.
Radiation B.C.
Sound Source
Radiation B.C.
Radiation B.C.
Radiation B.C.
Radiation B.C.
Sound Source
y_s
Wall B.C.

Acoustic pulse in free space

Reflection of an acoustic pulse (or incident wave train) from flat wall

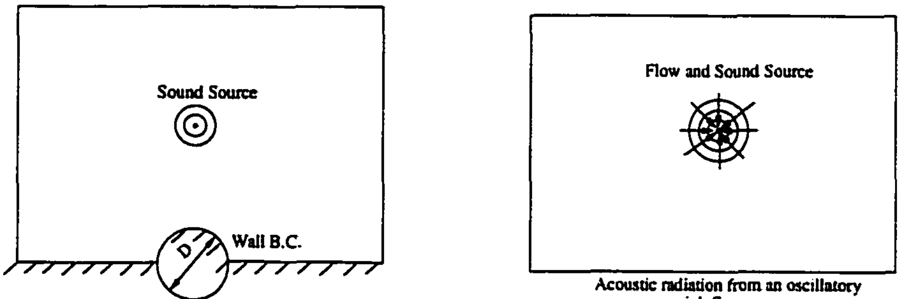
Sound Source
D
Wall B.C.
Flow and Sound Source

Reflection of an acoustic pulse (or incident wave train) from flat wall with bump

Acoustic radiation from an oscillatory sink flow

Figure 3.1 Benchmark cases

The two-dimensional unsteady Euler equations can be written in generalized curvilinear coordinates (ξ, η) as follows:

$$\frac{\partial \mathbf{q}}{\partial t}+\mathbf{A}\frac{\partial \mathbf{q}}{\partial \xi}+\mathbf{B}\frac{\partial \mathbf{q}}{\partial \eta}=\mathbf{S} \tag{3.1}$$

where

$$\mathbf{q}=\begin{Bmatrix}\rho\\u\\v\\p\end{Bmatrix},\quad \mathbf{A}=\begin{pmatrix}\hat{u} & \rho\xi_x & \rho\xi_y & 0\\ 0 & \hat{u} & 0 & \frac{\xi_x}{\rho}\\ 0 & 0 & \hat{u} & \frac{\xi_y}{\rho}\\ 0 & \gamma p\xi_x & \gamma p\xi_y & \hat{u}\end{pmatrix},\quad \mathbf{B}=\begin{pmatrix}\hat{v} & \rho\eta_x & \rho\eta_y & 0\\ 0 & \hat{v} & 0 & \frac{\eta_x}{\rho}\\ 0 & 0 & \hat{v} & \frac{\eta_y}{\rho}\\ 0 & \gamma p\eta_x & \gamma p\eta_y & \hat{v}\end{pmatrix},\quad \mathbf{S}=\begin{Bmatrix}s_1\\s_2\\s_3\\s_4\end{Bmatrix} \tag{3.2}$$

and the contravariant velocities $(\hat{u},\hat{v})$ are defined as:

$$\hat{u}=\xi_x u+\xi_y v,\quad \hat{v}=\eta_x u+\eta_y v \tag{3.3}$$

The complete Euler equations can be perturbed about a steady mean flow, first by substituting

$$\begin{Bmatrix}\rho\\u\\v\\p\end{Bmatrix}=\begin{Bmatrix}\rho_m\\U\\V\\P\end{Bmatrix}+\begin{Bmatrix}\rho'\\u'\\v'\\p'\end{Bmatrix} \tag{3.4}$$

and then by subtracting the steady equations governing the mean flow. Here the prime denotes the acoustic perturbation quantities. Further, if the nonlinear terms are neglected and a uniform mean flow is assumed, the linearized, two-dimensional, conservative Euler equations in generalized coordinates are obtained as (where primes are dropped):

$$\frac{\partial\hat{\mathbf{q}}}{\partial t}+\frac{\partial\hat{\mathbf{F}}}{\partial\xi}+\frac{\partial\hat{\mathbf{G}}}{\partial\eta}=\hat{\mathbf{S}} \tag{3.5}$$

where

$$\hat{\mathbf{q}}=\frac{1}{J}\begin{Bmatrix}\rho\\u\\v\\p\end{Bmatrix},\quad \hat{\mathbf{F}}=\frac{1}{J}\begin{Bmatrix}\hat{u}+\hat{U}\rho\\ \hat{U}u+\xi_x p\\ \hat{U}v+\xi_y p\\ \hat{u}+\hat{U}p\end{Bmatrix},\quad \hat{\mathbf{G}}=\frac{1}{J}\begin{Bmatrix}\hat{v}+\hat{V}\rho\\ \hat{V}u+\eta_x p\\ \hat{V}v+\eta_y p\\ \hat{v}+\hat{V}p\end{Bmatrix},\quad \hat{\mathbf{S}}=\frac{1}{J}\begin{Bmatrix}s_1\\s_2\\s_3\\s_4\end{Bmatrix} \tag{3.6}$$

$$\hat{u}=\xi_x u+\xi_y v,\quad \hat{v}=\eta_x u+\eta_y v,\quad \hat{U}=\xi_x U+\xi_y V,\quad \hat{V}=\eta_x U+\eta_y V \tag{3.7}$$

3.3 Boundary Conditions

3.3.1 Radiation Boundary Condition

At boundaries where there are only outgoing acoustic waves, a set of radiation boundary conditions can be derived based on the asymptotic solution of the linearized Euler equations. In the present work, the radiation boundary condition due to Tam and Webb (1993) is used in generalized curvilinear coordinates as,

$$\frac{\partial \mathbf{q}}{\partial t}+\frac{V_g}{R}\left[\left(x\xi_x + y\xi_y\right)\frac{\partial \mathbf{q}}{\partial \xi}+\left(x\eta_x + y\eta_y\right)\frac{\partial \mathbf{q}}{\partial \eta}+\frac{\mathbf{q}}{2}\right]=0 \qquad (3.8)$$

V_g is the group velocity of wave propagation, which is defined by,

$$V_g = \frac{x}{R}U+\frac{y}{R}V+\sqrt{C^2-\left(\frac{x}{R}V+\frac{y}{R}U\right)^2} \qquad (3.9)$$

where

$$R=\sqrt{x^2+y^2}$$

3.3.2 Outflow Boundary Condition

At the outflow region the outgoing disturbances, in general, consist of a combination of acoustic, entropy, and vorticity waves. The pressure disturbance is an acoustic fluctuation alone, while the density and velocity disturbances are due to the combined effect of the three types of waves at the boundary. For these last two variables, Euler equations are used. This yields the following set of boundary conditions (Tam and Webb 1993):

$$\frac{\partial \rho}{\partial t}+\hat{U}\frac{\partial \rho}{\partial \xi}+\hat{V}\frac{\partial \rho}{\partial \eta}=\frac{1}{C^2}\left(\frac{\partial p}{\partial t}+\hat{U}\frac{\partial p}{\partial \xi}+\hat{V}\frac{\partial p}{\partial \eta}\right) \qquad (3.10)$$

$$\frac{\partial u}{\partial t}+\hat{U}\frac{\partial u}{\partial \xi}+\hat{V}\frac{\partial u}{\partial \eta}=-\frac{1}{\rho_m}(\xi_x\frac{\partial p}{\partial \xi}+\eta_x\frac{\partial p}{\partial \eta}) \tag{3.11}$$

$$\frac{\partial v}{\partial t}+\hat{U}\frac{\partial v}{\partial \xi}+\hat{V}\frac{\partial v}{\partial \eta}=-\frac{1}{\rho_m}(\xi_y\frac{\partial p}{\partial \xi}+\eta_y\frac{\partial p}{\partial \eta}) \tag{3.12}$$

$$\frac{\partial p}{\partial t}+\frac{V_g}{R}\left[(x\xi_x+y\xi_y)\frac{\partial p}{\partial \xi}+(x\eta_x+y\eta_y)\frac{\partial p}{\partial \eta}+\frac{p}{2}\right]=0 \tag{3.13}$$

3.3.3 Characteristic Boundary Condition

As an alternative to the asymptotic radiation boundary condition and/or the outflow boundary condition, the characteristic boundary conditions could be used. Assuming locally one-dimensional flow, the Euler equations are written in the characteristic form,

$$\frac{\partial p}{\partial t}\mp\rho C\frac{\partial \hat{u}^i}{\partial t}+\Gamma^i_{1,3}=0, \quad \text{and} \quad \frac{\partial p}{\partial t}-C^2\frac{\partial \rho}{\partial t}+\Gamma^i_2=0 \tag{3.14}$$

where the characteristic waves $\Gamma^i_{1,3}$ and Γ^i_2 are defined by,

$$\Gamma^i_{1,3}=(\hat{u}^i\mp C)(\frac{\partial p}{\partial \xi^i}\mp\rho C\frac{\partial \hat{u}^i}{\partial \xi^i}), \quad \text{and} \quad \Gamma^i_2=\hat{u}^i(\frac{\partial p}{\partial \xi^i}-C^2\frac{\partial \rho}{\partial \xi^i}) \tag{3.15}$$

For boundary in ξ-direction (i.e. the normal to the boundary is in ξ-direction), $\xi^i=\xi$ and $\hat{u}^i=\hat{u}$. For boundary in η-direction (i.e. the normal to the boundary is in η-direction), $\xi^i=\eta$ and $\hat{u}^i=\hat{v}$. The incoming characteristic waves (to computational domain) are set to zero, while outgoing characteristic waves are computed by a one-sided scheme that only includes points inside the computational domain. Then, the time derivatives of the flow variables can be obtained.

3.3.4 Wall Boundary Condition

For inviscid flows, the boundary condition at a solid wall is that the velocity component normal to the wall is zero. For a high-order finite difference scheme, the order of the difference equations is higher than that of the Euler equations. Thus, the zero normal velocity boundary condition is insufficient to define a unique solution. Extra conditions must be imposed. These conditions can be satisfied if ghost values are introduced as extra unknowns. The number of ghost values is arbitrary but the minimum number must be equal to the number of boundary conditions. For an inviscid flow, the condition of no flux through the wall requires a minimum of one ghost value per boundary point on the wall. Physically, the wall exerts a pressure on the fluid to make the normal velocity vanish. This suggests that one may use a ghost value of 'p' (pressure) at the ghost point immediately below the wall to simulate the pressure of the wall.

For orthogonal generalized curvilinear coordinates, assuming that the wall lies across η=constant curve, the no-flux condition is $\hat{V}=0$. To impose this condition, the two momentum equations are combined to obtain the following equation for the normal pressure gradient:

$$\frac{\partial p}{\partial \eta}=-\frac{1}{\eta_x^2+\eta_y^2}[\rho_m \hat{U}(\eta_x \frac{\partial u}{\partial \xi}+\eta_y \frac{\partial v}{\partial \xi})+\frac{\partial p}{\partial \xi}(\eta_x \xi_x+\eta_y \xi_y)] \tag{3.16}$$

At the wall, using one-point-backward discretization for the η-derivative of the pressure, the ghost pressure is obtained as,

$$p_{gh}=\frac{-\Delta\eta}{a_{-1}(\eta_x^2+\eta_y^2)}[\rho_m \hat{U}(\eta_x \frac{\partial u}{\partial \xi}+\eta_y \frac{\partial v}{\partial \xi})+\frac{\partial p}{\partial \xi}(\eta_x \xi_x+\eta_y \xi_y)]-\frac{1}{a_{-1}}\sum_{\ell=0}^{5} a_\ell p_\ell \tag{3.17}$$

Inside the boundary region, the quantities $\frac{\partial \rho}{\partial \eta}$, $\frac{\partial \tilde{u}}{\partial \eta}$, and $\frac{\partial \tilde{v}}{\partial \eta}$ are all calculated using values of the variables lying inside the physical domain. For $\frac{\partial p}{\partial \eta}$, the stencils extend to the ghost point below the wall.

3.4 Discretized Equations

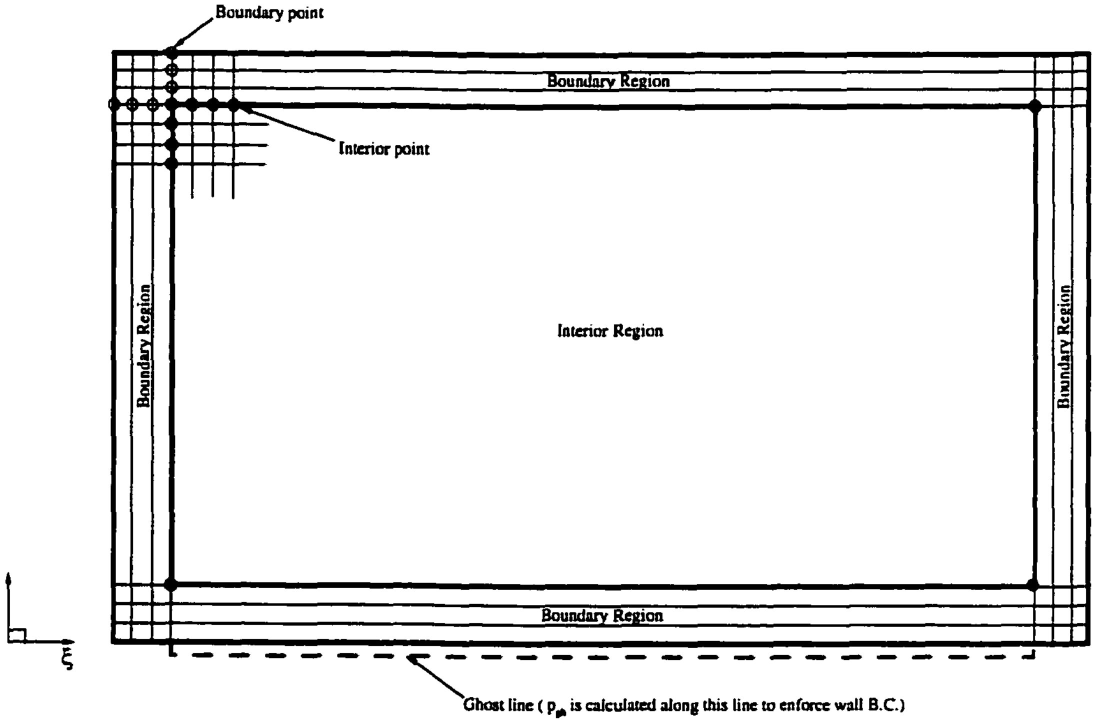
Boundary point
Boundary Region
Interior point
Boundary Region
Interior Region
Boundary Region
Boundary Region
η
ξ
Ghost line (p_w is calculated along this line to enforce wall B.C.)

Figure 3.2 Computational Domain.

The 7-point stencil, dispersion-relation-preserving (DRP) scheme of Tam and Webb (1993) is used for the spatial derivatives. The time integration is performed by optimized Runge-Kutta algorithm developed by Hu et al. (1996) or the DRP time integration of

Tam and Webb (1993). The computational domain is shown in figure 3.2. Since 7-point stencil is used, the computational boundary layer extends over three mesh points.

In some cases, it is necessary to remove spurious numerical oscillations due to nonlinearities or mismatches with the boundary conditions or the initial conditions. These short waves can be filtered by an artificial selective damping proposed by Tam and Shen (1993). The damping terms are added to the right side of the equations in the form:

$$\hat{\mathbf{D}} = -\frac{1}{J}\mu_a(\Delta\xi\frac{\partial\mathbf{q}}{\partial\xi} + \Delta\eta\frac{\partial\mathbf{q}}{\partial\eta}) \tag{3.18}$$

where the derivatives are discretized using selective damping coefficients d_k to obtain,

$$(\mathbf{D})^n_{\ell,m} = -\mu_a\sum_{k=-3}^{3} d_k(\mathbf{q}^n_{\ell+k,m} + \mathbf{q}^n_{\ell,m+k}) \tag{3.19}$$

where ℓ, m are the indices of the mesh points and the superscript n is the time level.

3.4.1 Linearized Euler Equations

$$\left(\frac{\partial\hat{\mathbf{q}}}{\partial t}\right)^n_{\ell,m} = -\left(\frac{\partial\hat{\mathbf{F}}}{\partial\xi}\right)^n_{\ell,m} - \left(\frac{\partial\hat{\mathbf{G}}}{\partial\eta}\right)^n_{\ell,m} + \left(\hat{\mathbf{S}}\right)^n_{\ell,m} + \left(\hat{\mathbf{D}}\right)^n_{\ell,m} \tag{3.20}$$

where

$$\left(\frac{\partial\hat{\mathbf{F}}}{\partial\xi}\right)^n_{\ell,m} = \frac{1}{\Delta\xi}\sum_{k=-3}^{3} a_k\hat{\mathbf{F}}^n_{\ell+k,m} \quad , \quad \left(\frac{\partial\hat{\mathbf{F}}}{\partial\eta}\right)^n_{\ell,m} = \frac{1}{\Delta\eta}\sum_{k=-3}^{3} a_k\hat{\mathbf{G}}^n_{\ell,m+k} \tag{3.21}$$

$$\left(\hat{\mathbf{D}}\right)^n_{\ell,m} = -\frac{1}{J}\mu_a\sum_{k=-3}^{3} d_k(\mathbf{q}^n_{\ell+k,m} + \mathbf{q}^n_{\ell,m+k}) \tag{3.22}$$

$$\left(\hat{\mathbf{D}}\right)^n_{\ell,m} = -\frac{1}{J}\mu_a\sum_{k=-3}^{3} d_k(\mathbf{q}^n_{\ell+k,m} + \mathbf{q}^n_{\ell,m+k})$$

3.4.2 Nonlinear Euler

$$\left(\frac{\partial \mathbf{q}}{\partial t}\right)_{\ell,m}^{n} = -\mathbf{A}_{\ell,m}^{n}\left(\frac{\partial \mathbf{q}}{\partial \xi}\right)_{\ell,m}^{n} - \mathbf{B}_{\ell,m}^{n}\left(\frac{\partial \mathbf{q}}{\partial \eta}\right)_{\ell,m}^{n} + (\mathbf{S})_{\ell,m}^{n} + (\mathbf{D})_{\ell,m}^{n} \tag{3.23}$$

where

$$\left(\frac{\partial \mathbf{q}}{\partial \xi}\right)_{\ell,m}^{n} = \frac{1}{\Delta\xi}\sum_{k=-3}^{3} a_k \mathbf{q}_{\ell+k,m}^{n} \quad , \quad \left(\frac{\partial \mathbf{q}}{\partial \eta}\right)_{\ell,m}^{n} = \frac{1}{\Delta\eta}\sum_{k=-3}^{3} a_k \mathbf{q}_{\ell,m+k}^{n} \tag{3.24}$$

$$(\mathbf{D})_{\ell,m}^{n} = -\mu_a \sum_{k=-3}^{3} d_k (\mathbf{q}_{\ell+k,m}^{n} + \mathbf{q}_{\ell,m+k}^{n}) \tag{3.25}$$

3.4.3 Fully Discretized Equations

For DRP time integration:

$$\mathbf{q}_{\ell,m}^{n+1} = \mathbf{q}_{\ell,m}^{n} + \Delta t \sum_{k=0}^{3} b_k \left(\frac{\partial \mathbf{q}}{\partial t}\right)_{\ell,m}^{n-k} \tag{3.26}$$

For LDDRK time integration:

$$\begin{aligned} \overline{\mathbf{q}}_{\ell,m}^{k} &= \mathbf{q}_{\ell,m}^{n} + b_k \Delta t \frac{\partial \mathbf{q}}{\partial t}^{k-1} \quad ; \quad k = 0,1,2,3,4 \\ \mathbf{q}_{\ell,m}^{n+1} &= \overline{\mathbf{q}}_{\ell,m}^{4} \end{aligned} \tag{3.27}$$

Numerical values of the coefficients b_k and d_k are given in Appendix A. The boundary conditions equations are discretized using the same method. But in this case, unsymmetric stencils that include only points inside the physical domain are used. These are also listed in Appendix A.

3.5 Sound Source

The acoustic perturbations are introduced by an initial Gaussian pulse or time-periodic source term. This is explained as follows:

(1) Acoustic Pulse:

For initial value problems, the source vector **S** is nullified. An acoustic pulse is generated by an initial Gaussian pressure and density distributions,

$$p = \rho = \varepsilon e^{-\alpha((x-x_s)^2+(y-y_s)^2)} \tag{3.28}$$

where ε is the pulse amplitude , $\alpha = \frac{\ln 2}{b^2}$, b is the half-width of the pulse, and (x_s, y_s) is source location.

(2) Periodic source:

The periodic source is introduced in the energy equation and the source vector has the following form:

$$\mathbf{S}(x, y, t) = \varepsilon \sin(\omega t) e^{-\alpha((x-x_s)^2+(y-y_s)^2)} \begin{bmatrix} 0 & 0 & 0 & 1 \end{bmatrix}^T \tag{3.29}$$

where ω is the angular frequency of the source.

(3) Oscillatory sink flow:

To test the effectiveness of the computational method for non-uniform mean flow, consider Euler's equations with source terms added in a way that the isentropic condition $(p / p_\infty) = (\rho / \rho_\infty)^\gamma$ is satisfied. The source vector is:

$$\mathbf{S} = \begin{bmatrix} s & -\frac{u}{\rho} s & -\frac{v}{\rho} s & \frac{\gamma p}{\rho} s \end{bmatrix}^T \tag{3.30}$$

where

$s = \bar{s} + s'$,

$\bar{s} = -\bar{\varepsilon} e^{-\bar{\alpha}((x-x_s)^2+(y-y_s)^2)}$, $s' = \varepsilon\, e^{-\alpha((x-x_s)^2+(y-y_s)^2)} \cos(\omega t)$, $\bar{\alpha} = \frac{\ln 2}{\bar{b}^2}$, and $\alpha = \frac{\ln 2}{b^2}$.

Table 3.1 summarizes the test cases. In what follows, benchmark cases are categorized according to the governing equations used to solve the problem.

3.6 Linear Cases

3.6.1 Pulse in Free Space

An acoustic pulse is generated by an initial pressure disturbance with a Gaussian spatial distribution centered at (0,0). The uniform H-grid with 141×71 points is shown in figure 3.3. Distances are normalized by the spatial step Δx. The pulse amplitude is 0.01 and the Gaussian curve half-width is 6. Using LDDRK time integration scheme, the time step is 0.37. The computed pressure waveform along the x-axis at different times is plotted in figure 3.4. The exact solution is represented by solid circles. The exact and computed solutions are clearly almost identical. An important computational issue to be considered in initial value problems is the use of adequate grid points to represent the initial pulse. In this example, six grid points are used inside the half-width area of the Gaussian pulse, which is adequate number of grid points for the DRP scheme to capture the initial wave. Since the initial pulse is symmetric, using uniform mesh spacing at the source is important to ensure isotropy of the source. A distorted wave front is noticed when there is a large difference between grid spacing in x- and y-directions near the source. The time step can be increased as long as the numerical stability bounds are not reached; i.e, it does not affect the accuracy of the solution.

Equations	Case	Time Integration	$\bar{\varepsilon}, \varepsilon$	$\bar{b}, b$	x_s, y_s	Grid Type	$\Delta\bar{t}, \Delta t$	μa
Linearized Euler Equations	Pulse in free space	LDDRK	0, 0.01	0, 6	0,0	H 141×71	0, 0.37	-
	Pulse reflected from flat wall	LDDRK	0, 0.01	0, 6	0, 20	H 141×71	0, 0.37	-
	Periodic source reflected from flat wall	DRP	0, 0.01	0, 6	0, 20	H 141×71	0, 0.08	-
Nonlinear Euler Equations	Pulse in free space	LDDRK	0, 1	0, 6	0,0	H 141×71	0, 0.37	10 U_{sten}.
	Pulse reflected from bump on flat wall	LDDRK	0, 1	0, 0.6	0, 2	O 65×65	0, 0.008	0.001
	Oscillatory sink flow	LDDRK	10.0, 0.001	6, 3	0, 0	H 101×101	0.2, 0.08	0.1

Table 3.1 Benchmark cases.

3.6.2 Pulse Reflected by a Flat Wall

Consider the reflection of a two-dimensional acoustic pulse by a plane wall located at y=0. The pulse is generated by a Gaussian curve centered at (0, 20) and of half-width equals 6. The pulse amplitude is 0.01. Figure 3.5 shows the calculated pressure contours associated with the acoustic pulse at 0, 60, 120, and 180 time steps. The corresponding contours of the exact solution, from Appendix B, are also plotted in this figure. To the accuracy given by the thickness of the contour lines, the two sets of contours are almost indistinguishable. At 60 time steps, the front part of the pulse reaches the wall. It is immediately reflected back. At 120 time steps, the entire pulse has effectively been reflected off the wall creating a double pulse pattern; one from the original source and the other from the image source below the wall. When characteristic boundary conditions are used, the solution exhibits minimum reflections up to 180 time steps (refer to figure 3.6). After this instant the failure of these boundary conditions begins to appear gradually. This failure is due to the inability of the characteristic boundary condition to pass the waves, which have inclined incidence to the boundary, without reflection. This is clear in figure 3.6, where the waves are reflected from the corners. This supports the idea reported by many researchers of the failure of the characteristic boundary conditions if long time integration is pursued.

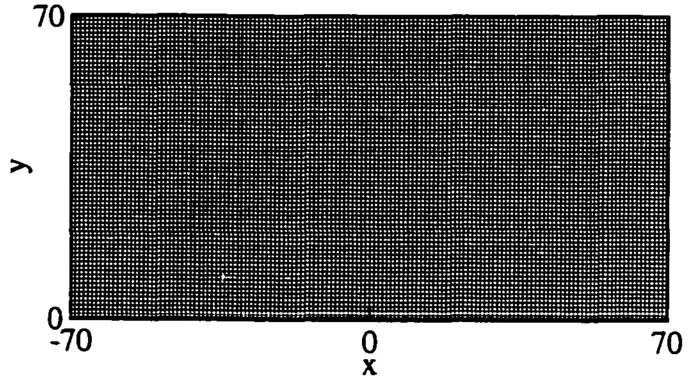

Figure 3.3 H-grid (141×71 points) for initial value problems.

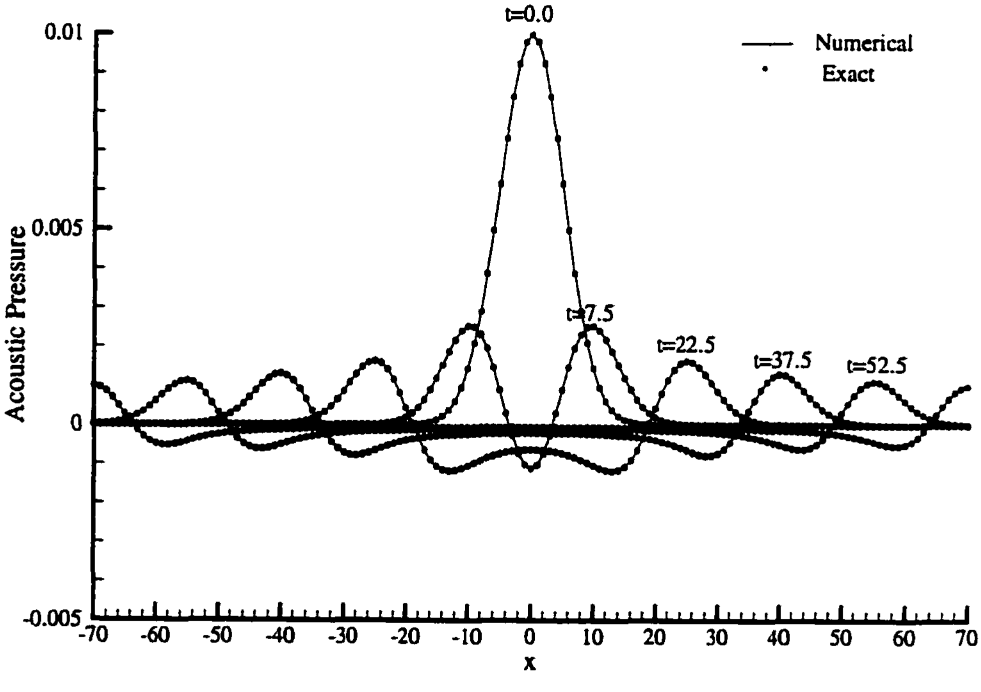

Figure 3.4 Pressure waveforms of an acoustic pulse in free space along the line y=0; numerical solution of LEE compared with the exact solution. (ε=0.01, b=6, H-grid 141x71, Δt=0.37,μ_a=0)

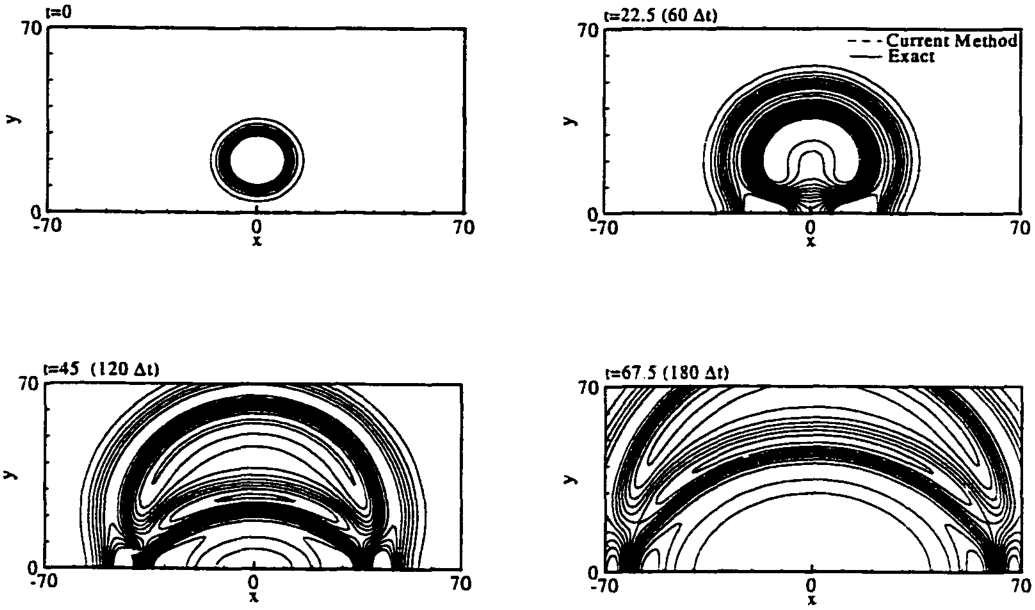

Figure 3.5 Pressure contours of an acoustic pulse reflected by a flat wall at y=0. (ε=0.01, b=6, H-grid 141x71, Δt=0.37,μ_a=0)

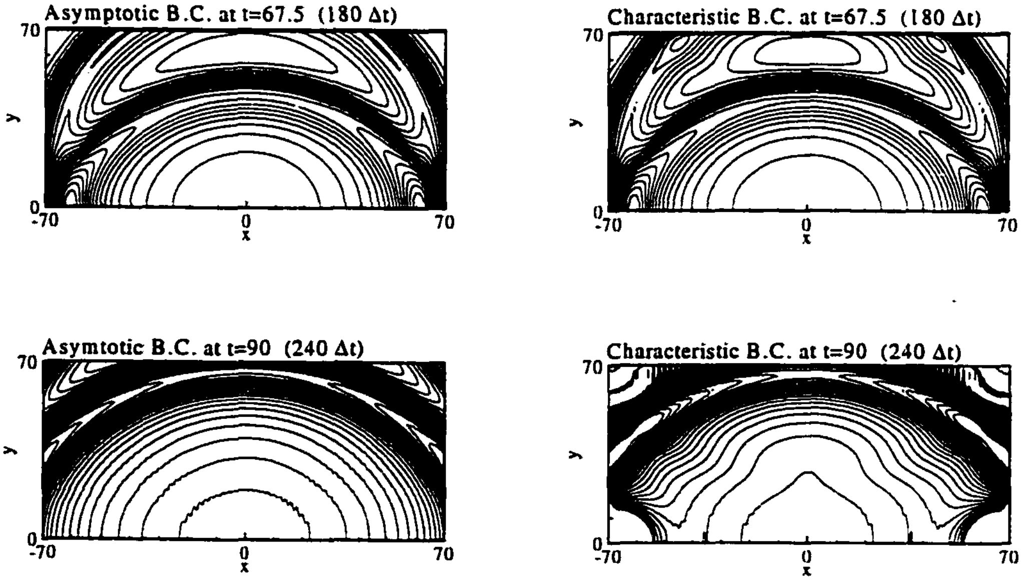

Figure 3.6 Comparison of pressure contours computed using asymptotic boundary condition and characteristic boundary condition.

(Acoustic pulse reflected by a flat plate; ε=0.01, b=6, H-grid 141x71, Δt=0.37,μ_a=0)

3.6.3 Time Periodic Acoustic Wave Train Reflected by a Solid Wall

The acoustic wave train is assumed to be generated by a time periodic source in the energy equation. Physically, the source represents a heat source or sink. A uniform H-grid with 141×71 points is used. The center of the source is located at (0,20) and the angular frequency, ω, is 0.2 π. The time step is 0.08 using DRP time integration scheme. After the transient solution has propagated out of the computational domain, the pressure fluctuation is time periodic with angular frequency ω. The spatial pressure distribution has the form of an interference pattern created by the reflected wave train and the wave train generated directly by the source. Figure 3.7 shows the computed pressure contour patterns compared with the exact solution from Appendix B. Perfect matching is shown in the figure. For time periodic problems, three computational issues are to be considered. The first is the adequate representation of the amplitude of the source. For this example, six grid points are used inside the half-width region of the Gaussian amplitude. This number is enough to represent the Gaussian curve correctly. The second is the number of grid points per wavelength (PPW), since at least five points are needed for the DRP scheme to capture the wave correctly. For the current example, the period of the oscillation ($2\pi/\omega$) is equal to 10. The corresponding acoustic wavelength is equal to 10 mesh spacings. This exceeds the minimum required number of grid points. The third is the use of an adequate number of time steps per period of oscillation. This requirement is sometimes more stringent than the stability of the numerical scheme. For this example, 125 time steps are used per period of oscillation. From numerical stability point of view, 60 time steps per period of oscillation are enough. Usually, more than one hundred time steps per period of oscillation are needed.

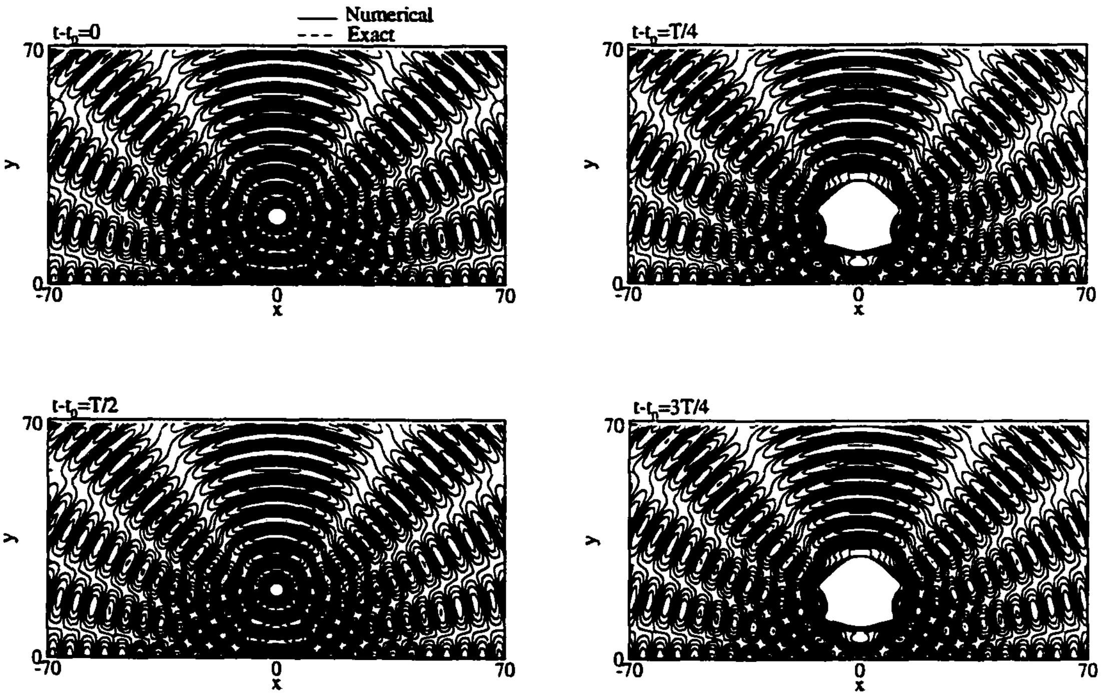

Figure 3.7 Pressure contour patterns adjacent to a solid wall generated by a time periodic acoustic source. (ε=0.01, b=6, ω=0.2 π, H-grid 141x71, Δt=0.08,μ_a=0)

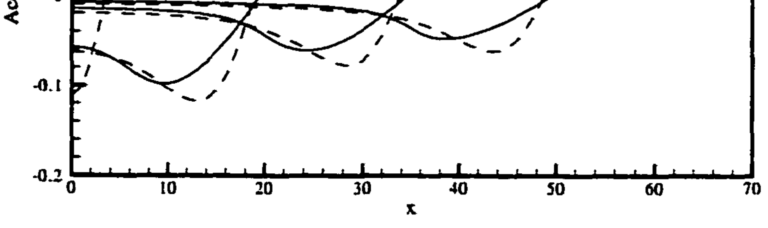

Figure 3.8 Pressure waveforms of an acoustic pulse in free space along the line y=0; linear and nonlinear solutions.

3.7 Nonlinear Cases

3.7.1 Pulse in Free Space

For the purpose of comparing the linear solution with the nonlinear solution, a Gaussian pulse with unit amplitude and half-width of 6 is generated at the center of the domain (0,0). Both LEE and NLEE are solved to determine the wave propagation in free space. Figure 3.8 shows the waveform at different time instants. The waveform is highly distorted by the nonlinear steepening effect. Near the wave front, the nonlinear solution suffers from spurious oscillations. To alleviate this problem, the damping term is modified to (Tam and Shen, 1993) as follows:

$$\left(\hat{\mathbf{D}}\right)^n_{\ell,m} = -\frac{1}{J}\frac{u_{stencil}}{R_{stencil}}\sum_{k=-3}^{3} d_k\left(\mathbf{q}^n_{\ell+k,m} + \mathbf{q}^n_{\ell,m+k}\right) \qquad (3.31)$$

where

$u_{stencil} = \left|u_{\max} - u_{\min}\right|$; the difference between the maximum and minimum velocities in the stencil.

$R_{stencil}$ is the stencil Reynolds number, which is taken to be 0.1.

3.7.2 Pulse Reflected by a Flat Wall with Bump

A unit pulse is generated by a Gaussian curve centered at (0,2) and of half-width equals 0.6. The bump is located at (0,0). Bump diameter is used to normalize length scales. The 65 by 65 O-grid is shown in figure 3.9. The grid is uniform in r-θ plane, but it is non-uniform in curvilinear coordinates ξ-η plane. Along ξ-direction, which is the clockwise peripheral direction, the spacing ($r\Delta\theta$) is increasing as r increases. Along η-direction, which is the positive r-direction, the spacing is constant and equals to Δr. The source isotropy is ensured by imposing uniform spacing at the source location. The grid resolution is determined by the conditions $imax=1+\pi r_s/\Delta\xi_s$ and $jmax=1+(rmax-0.5)/\Delta\eta_s$, where $\Delta\xi_s=\Delta\eta_s=b/PPS$; *PPS* is the number of grid points per half-width of the source (taken to be 6 herein). The Jacobian of the transformation is evaluated analytically as

$$J=\frac{\partial(\xi,\eta)}{\partial(x,y)}=\begin{pmatrix} \frac{y}{r^2} & -\frac{x}{r^2} \\ \frac{x}{r} & \frac{y}{r} \end{pmatrix}$$

Figure 3.10 shows the calculated pressure contours at 0, 100, 200, 300, 400, 500, 600, and 700 time steps. The success of the curvilinear coordinates formulation is demonstrated by this example. A clean solution is obtained near the wall and at the outer boundaries.

3.7.3 Oscillatory Sink Flow

To assess the accuracy of the method for non-uniform mean flow cases, the simulation of oscillatory sink flow in two dimensions is performed for both the mean flow and acoustics. The sink flow is produced by a Gaussian curve of amplitude 10 and half-width 6. The acoustic source is generated by Gaussian distribution of amplitude 0.001 and half-width 3. The angular frequency of the acoustic source is 0.2 π. A uniform H-grid with 101×101 points is used. The spatial step is used to normalize length scales. The LDDRK scheme is used for the time integration. The ratio between the acoustic perturbation and the mean flow amplitudes is 1:10000. This represents a tough challenge for any numerical method to compute both of them at the same time. Therefore, the simulations are carried out in two steps: the mean flow computation and the acoustic field computation.

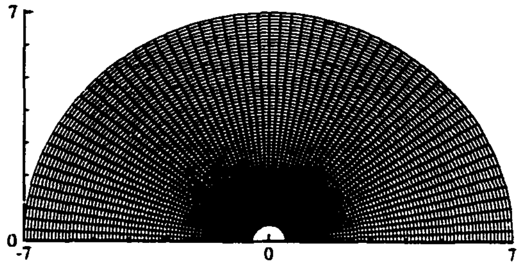

Figure 3.9 O-grid for flat wall with bump problem.

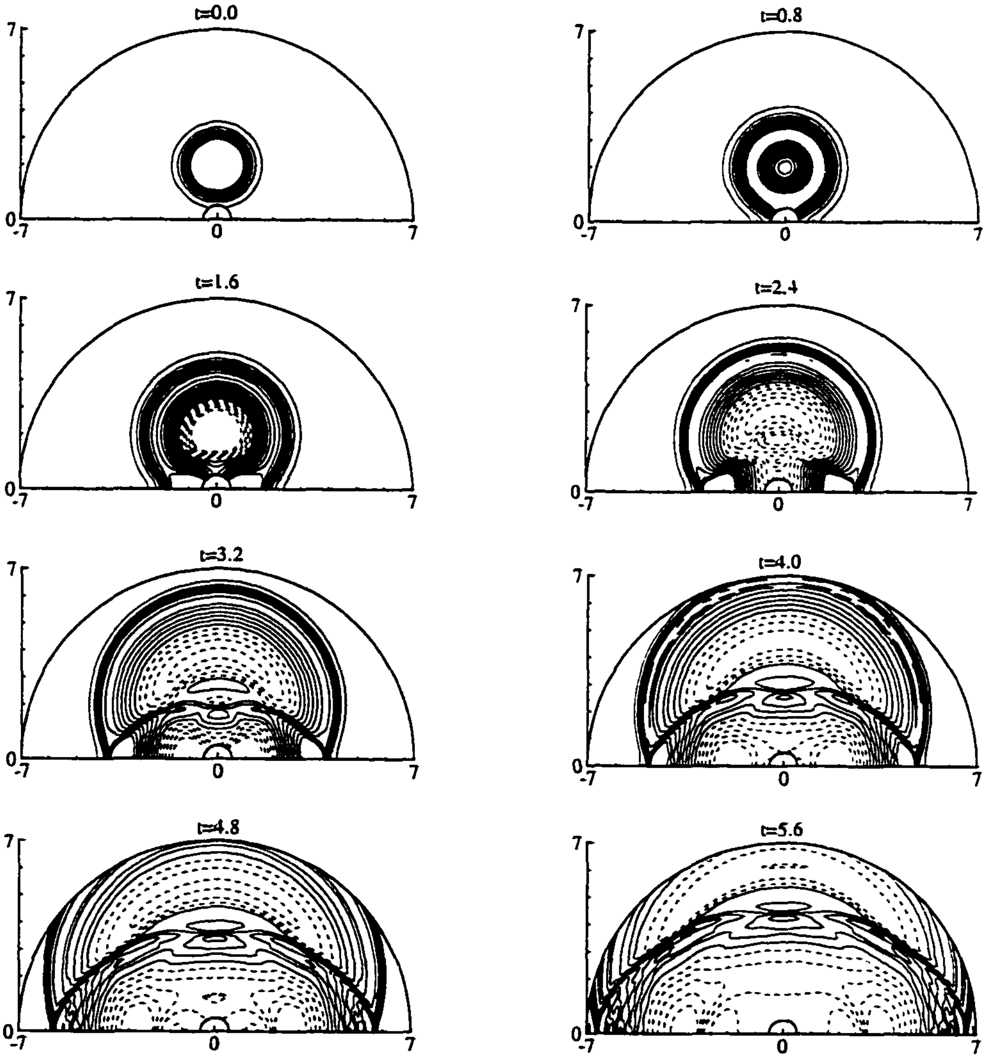

Figure 3.10 Pressure contours of an acoustic pulse reflected by a flat wall with bump.

(ε=1, b=0.6, Δt=0.008)

3.7.3.1 Mean Flow Computation

For the first step, the acoustic source is turned off (ε=0). The canceling-the-residual technique is used to accelerate the steady state convergence for the mean flow computation. Since the order of accuracy for the mean flow solution is different from that of the acoustic solution, further time marching calculation is a waste of effort once the residual reaches a level of the order 10^{-5}. It is possible to add a term, which is equal in magnitude but opposite in sign to the residual, to the right side of each of the governing equations. These are terms of order 10^{-5} or less and would not affect the accuracy of the numerical solution. The consequence of adding these source terms is to cancel the residuals instantaneously to zero. For finite difference marching scheme, the residuals are greatly reduced in this way but they would not exactly equal zero. The procedure is repeated until machine accuracy is achieved.

Figure 3.11 shows the maximum residual $\underset{x,y}{Max}(d\mathbf{q}/dt)$. The arrows in this figure indicate when the canceling-the-residual technique is applied. It is clear that there is a dramatic decrease (of 4 or 5 orders of magnitude) in the residual immediately after each application of the method. The computed mean density and velocity are plotted along x-axis in figure 3.12 together with the exact results which are obtained by half-analytical and half-numerical method (refer to Appendix B). The numerical solution matches the exact solution almost perfectly.

3.7.3.2 Acoustic Field Computation

The time-dependent acoustic source is turned on after the steady state solution is computed. The time step is calculated to ensure accuracy of the time integration. The period of oscillation has 125 time steps. After a short transient, a periodic state is obtained. The spatial distributions of instantaneous density and velocity along x-axis are plotted in figure 3.13. Again, a perfect match with the exact solution is obtained.

One computational issue should be noted here. Although, LDDRK scheme allows larger time-steps to be used, the time accuracy consideration inhibits the use of such large time steps. In fact, for such problems the DRP time integration is more appropriate since it needs much less effort per time step (for DRP time integration d**q**/dt is calculated only once for each time step, while, n-stage LDDRK scheme needs (n-1)-times calculation of d**q**/dt for each time step). Unless a large period of oscillation is considered, which allows the use of the large time steps offered by the LDDRK scheme, the DRP time integration is recommended. In terms of storage, four levels of storage are required to store d**q**/dt and one level to store **q** for the DRP time integration, while one level of storage is required to store d**q**/dt and two levels to store **q** for the 5-stage LDDRK scheme.

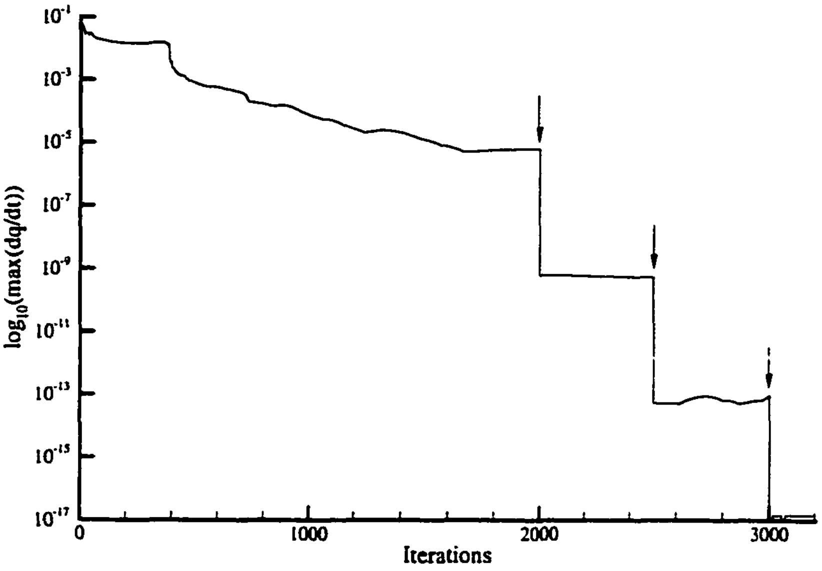

Figure 3.11 Time history of the maximum residual. Arrows indicate the application of the canceling-the-residual technique for accelerated convergence.

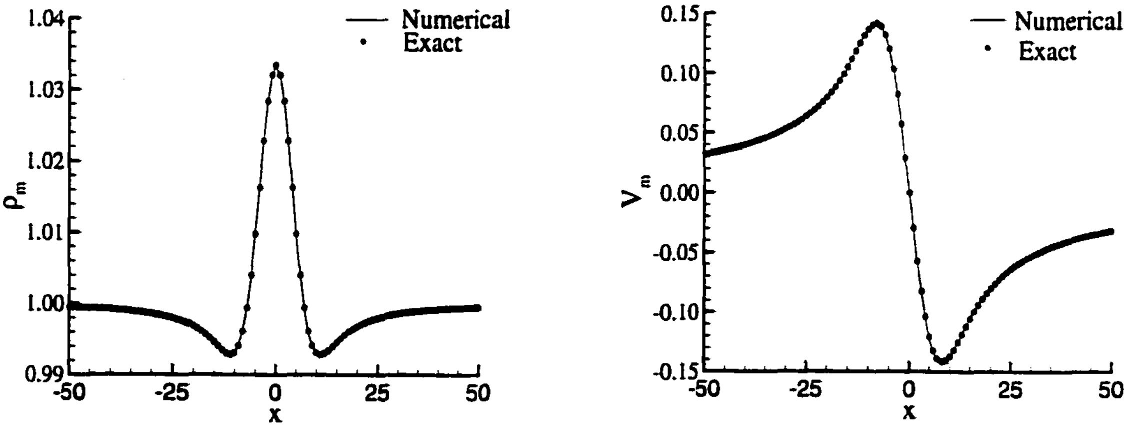

Figure 3.12 Mean flow solution of sink. (a) Density along x-axis. (b) Velocity along x-axis.

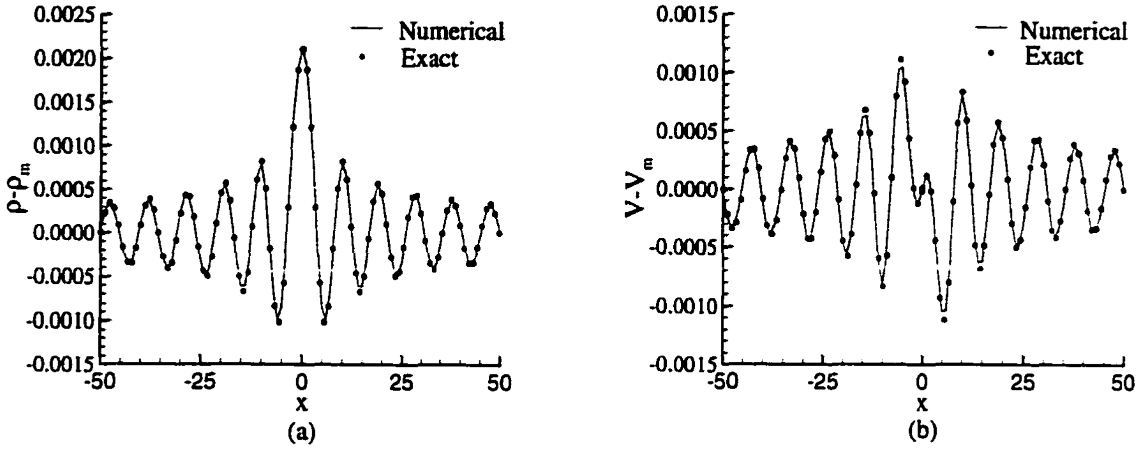

Figure 3.13 Acoustic wave propagation along x-axis. (a) Acoustic density. (b) Acoustic velocity.

CHAPTER IV
SUPERSONIC JET

4.1 Introduction

The analysis of supersonic jet is introduced in this chapter. Perfectly expanded supersonic jet is considered. Figure 4.1 is a schematic drawing of a perfectly expanded jet. Three streamwise regimes are identified. Those are the potential core, transitional, and fully developed regimes. The flow is uniform in the conical region near the centerline of the jet. The shear layer, or mixing layer, extends from the edges of the uniform core to the free stream region. In the developed region, the shear layer extends from the centerline to the free stream region. The sound waves are generated as a result of turbulent fluctuations of the mean flow.

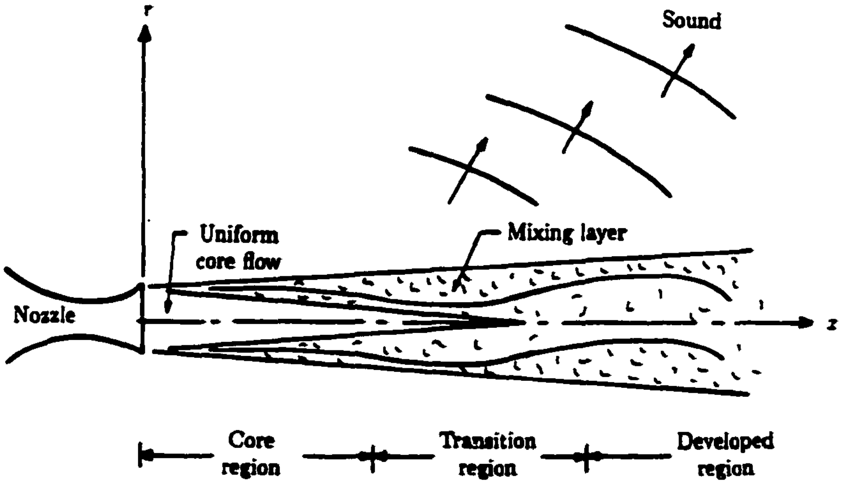
r
Sound
Uniform core flow
Mixing layer
Nozzle
z
Core region
Transition region
Developed region

Figure 4.1 Schematic drawing of perfectly expanded jet flow.

In section 4.2, the parabolic Reynolds averaged Navier-stokes equations are solved for the mean flow. They are written in stream function coordinates. An iterative marching procedure is used to solve the system of equations obtained. The stability analysis is presented in section 4.3. Compressible Rayleigh equation is solved using Runge-Kutta scheme. For a given Strouhal number, St, the wave number, α, is obtained through an iterative procedure. Supersonic jet noise analysis is described in section 4.4. At jet inlet, the instability waves are used to perturb the mean flow. The linearized Euler equations are considered. Azimuthal mode decomposition is employed to treat the θ-derivatives. The resulting complex equations are solved. Flow-adapted grid and DRP time integration on multi-blocks are used. The computational method is used to simulate the noise generated by a Mach 2.1 supersonic cold jet (Troutt & Mclaughlin 1982). First, in section 4.5, the mean flow solution is obtained. The results of laminar and turbulent calculations are presented and compared with the analytical solution. Second, the Rayleigh equation is solved for the eigen functions at the jet inlet for St=0.2. The results of these calculations are presented in section 4.6. Third, the linearized Euler equations are solved for the acoustic field. The results for the axisymmetric and helical modes are compared with the experimental data in section 4.7.

4.2 Mean Flow Analysis

4.2.1 Governing Equations

The compressible flow of a free jet is governed by the continuity, momentum, energy and state equations. The mean flow development of an axisymmetric free jet is governed by the Reynolds averaged boundary layer equations for compressible flow. The flow variables are decomposed into a time averaged or mean value part and a fluctuating or turbulent part as follows:

$$\rho = \rho_m + \rho', \quad u = U + u', \quad v = V + v', \quad p = P + p', \text{ and } T = T_m + T'$$

With the jet static pressure matched to the ambient pressure and the density–velocity and density-enthalpy correlations neglected, the equations in axisymmetric coordinates reduce to the following:

Continuity:
$$\frac{\partial(r\rho_m U)}{\partial x} + \frac{\partial(r\rho_m \tilde{V})}{\partial r} = 0 \tag{4.1}$$

Momentum:
$$\rho_m U\frac{\partial U}{\partial x} + \rho_m \tilde{V}\frac{\partial U}{\partial r} = \frac{1}{r}\frac{\partial}{\partial r}[r(\mu\frac{\partial U}{\partial r} - \rho_m \overline{u'v'})] \tag{4.2}$$

Energy:

$$\rho_m U\frac{\partial H}{\partial x} + \rho_m \tilde{V}\frac{\partial H}{\partial r} = \frac{1}{r}\frac{\partial}{\partial r}\{r[\frac{\mu}{\Pr}\frac{\partial H}{\partial r} - \rho_m\, Cp\, \overline{v'T'} + U\ ((1 - \frac{1}{\Pr})\mu\frac{\partial U}{\partial r} - \rho_m \overline{u'v'})]\} \tag{4.3}$$

State:
$$P = \rho_m\, R_g T_m \tag{4.4}$$

where

$\tilde{V}$ is a mass averaged quantity, defined as,

$$\tilde{V} = \frac{1}{\rho_m}(\rho_m V + \overline{\rho' v'}) \tag{4.5}$$

H is the total specific enthalpy defined as $H = C_p T_m + \frac{1}{2}U^2$,

$-\rho_m\ \overline{u'v'}$ is the Reynolds stress,

$-\rho_m\ \overline{v'T'}$ is the Reynolds heat flux

The laminar viscosity is computed from Sutherland's law,

$$\mu = \mu_0 (\frac{T}{T_0})^{3/2} \frac{T_0 + S_0}{T + S_0} \tag{4.6}$$

where S_0=110.3 , and μ_0 is the viscosity at T_0=273° K ($\mu_0 = 17.1 \times 10^{-6}$ Pa/s for air).

4.2.2 Turbulence Model

The mixing length model is used to model the Reynolds stress term $-\rho_m \overline{u'v'}$ and Reynolds heat flux term $-\rho_m \overline{v'T'}$ as follows:

$$-\rho_m \overline{u'v'} = \mu_T \frac{\partial u}{\partial r} \tag{4.7}$$

$$-\rho_m C_p \overline{v'T'} = \frac{C_p}{\mathrm{Pr}_T} \mu_T \frac{\partial T_m}{\partial r} \tag{4.8}$$

where Pr_T is the turbulent Prandtl Number which is equal to *0.5* for free jets.

The turbulent viscosity is calculated as:

$$\mu_T = \rho_m (C_1 C_2 \ell)^2 \left| \frac{\partial U}{\partial r} \right| \tag{4.9}$$

where C_1 is the incompressible mixing length constant, C_2 is the compressible mixing length constant, and ℓ is the mixing length defined by,

$$\ell = \frac{\Delta U}{\left| \frac{\partial U}{\partial r} \right|_{\max}} \tag{4.10}$$

where ΔU is the velocity difference across the shear layer.

Using 4.7 and 4.8, the governing equations reduce to,

$$\frac{\partial (r \rho_m U)}{\partial x} + \frac{\partial (r \rho_m \tilde{V})}{\partial r} = 0 \tag{4.11}$$

$$\rho_m U\frac{\partial U}{\partial x}+\rho_m \tilde{V}\frac{\partial U}{\partial r}=\frac{1}{r}\frac{\partial}{\partial r}[r\mu_{eff}\frac{\partial U}{\partial r}] \tag{4.12}$$

$$\rho_m U\frac{\partial H}{\partial x}+\rho_m \tilde{V}\frac{\partial H}{\partial r}=\frac{1}{r}\frac{\partial}{\partial r}\{ r\ [\frac{\mu_{eff}}{\mathrm{Pr}_{eff}}\frac{\partial H}{\partial r}+U\ (\mu_{eff}-\frac{\mu_{eff}}{\mathrm{Pr}_{eff}})\frac{\partial U}{\partial r}]\} \tag{4.13}$$

$$\rho_m=\frac{1}{(\gamma-1)M_j^2 h} \tag{4.14}$$

where

$$\mu_{eff}=\mu+\mu_T,\qquad \mathrm{Pr}_{eff}=\frac{\mu_{eff}}{\frac{\mu}{\mathrm{Pr}}+\frac{\mu_T}{\mathrm{Pr}_T}} \tag{4.15}$$

$$\mu=\mu_0(\frac{h}{h_0})^{3/2}\frac{1+\frac{S_0}{T_0}}{\frac{h}{h_0}+\frac{S_0}{T_0}} \tag{4.16}$$

$$h=\frac{C_p T_m}{U_j^2}=H-\frac{1}{2}U^2 \tag{4.17}$$

These equations are non-dimensionalized by the following reference values: spatial coordinates by R_j, velocity by U_j^2, density by ρ_j, pressure by $\rho_j U_j^2$, enthalpy by U_j^2, and viscosity by $\rho_j U_j R_j$. The subscript 'j' is used to indicate jet exit conditions.

4.2.3 Equations in Stream Function Coordinates

The equations of motion are transformed to stream function coordinates using,

$$\frac{\partial\psi}{\partial r}=r\rho_m U,\quad \frac{\partial\psi}{\partial x}=-r\rho_m\tilde{V} \tag{4.18}$$

These equations ensure that the continuity equation is satisfied. The derivatives of a general function '*f*' in cylindrical coordinates (*x, r*) is transformed to stream function coordinates (*x, Ψ*) using,

$$\frac{\partial f}{\partial x}=\frac{\partial f}{\partial x}+\frac{\partial \psi}{\partial x}\frac{\partial f}{\partial \psi} \quad \& \quad \frac{\partial f}{\partial r}=\frac{\partial \psi}{\partial r}\frac{\partial f}{\partial \psi} \tag{4.19}$$

Using 4.18 and 4.19, the governing equations become,

$$\frac{\partial}{\partial \psi}[A\frac{\partial U}{\partial \psi}]=\frac{\partial U}{\partial x} \tag{4.20}$$

$$\frac{\partial}{\partial \psi}[B\frac{\partial H}{\partial \psi}+C\frac{\partial U}{\partial \psi}]=\frac{\partial H}{\partial x} \tag{4.21}$$

where

$$A=r^2\mu_{eff}\rho_m U, \quad B=r^2\frac{\mu_{eff}}{\mathrm{Pr}_{eff}}\rho_m U, \; and \quad C=r^2\rho_m U^2(\mu_{eff}-\frac{\mu_{eff}}{\mathrm{Pr}_{eff}})$$

4.2.4 Boundary Conditions

The boundary conditions at r=0 are derived based on the removal of the singularity from the governing equations 4.11-4.13 at the centerline. The continuity equation leads to the condition $\tilde{V}=0$. The momentum equation has the singular term, $\frac{1}{r}(\mu_{eff}\partial U/\partial r)$, which implies that $\partial U/\partial r$ must vanish at the centerline. Similarly, from the energy equation, $\partial H/\partial r$ must vanish at the centerline. Since x is independent of ψ along the centerline, i.e. $\partial x/\partial \psi=0$, the ψ-derivatives of U and H must vanish at the centerline,

$$\left(\frac{\partial U}{\partial \psi}\right)_{r=0}=0 \quad \& \quad \left(\frac{\partial H}{\partial \psi}\right)_{r=0}=0 \tag{4.22}$$

The outer boundary condition is simply that the U and H values equal the free stream values; that is,

$$(U)_{r=r\max} = U_\infty \quad \& \quad (H)_{r=r\max} = H_\infty \tag{4.23}$$

where ∞ indicates free stream conditions.

4.2.5 Computational Method

Assuming uniform grid in x and r directions, the Ψ grid will not be uniform and $\Delta\Psi$ can be calculated as follows (see figure 4.2):

$$\begin{aligned}\Delta\psi_j = \psi_j - \psi_{j-1} &= \int_{r_{j-1}}^{r_j} \frac{\partial\psi}{\partial r} dr = \frac{1}{2}[(\frac{\partial\psi}{\partial r})_j + (\frac{\partial\psi}{\partial r})_{j-1}]\Delta r \\ &= \frac{1}{2}[(r\rho_m U)_j + (r\rho_m U)_{j-1}]\Delta r\end{aligned} \tag{4.24}$$

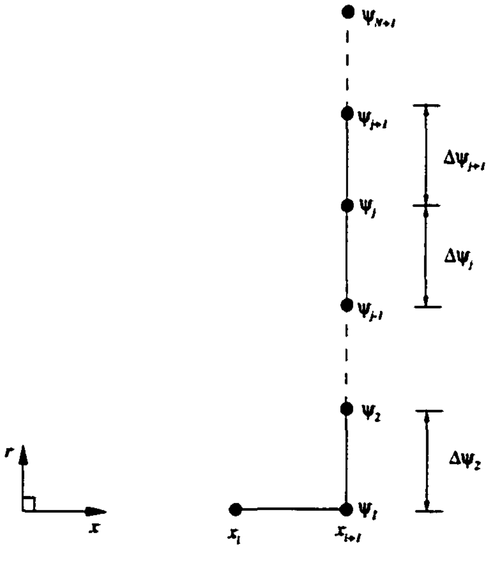
ψ_{N+1}
ψ_{j+1}
$\Delta\psi_{j+1}$
ψ_j
$\Delta\psi_j$
ψ_{j-1}
ψ_2
$\Delta\psi_2$
ψ_1
r
x
x_i
x_{i+1}

Figure 4.2 The stream function grid for mean flow calculations.

Using second order central discretization in Ψ-direction and first order backward in x-direction, equations 4.20 and 4.21 become

$$\left\{\frac{2}{\Delta\psi_j+\Delta\psi_{j+1}}[A_{j+\frac{1}{2}}\frac{U_{j+1}-U_j}{\Delta\psi_{j+1}}-A_{j-\frac{1}{2}}\frac{U_j-U_{j-1}}{\Delta\psi_j}]\right\}_i=\frac{U_{i,j}-U_{i-1,j}}{\Delta x} \qquad (4.25)$$

$$\left\{\frac{2}{\Delta\psi_j+\Delta\psi_{j+1}}[B_{j+\frac{1}{2}}\frac{H_{j+1}-H_j}{\Delta\psi_{j+1}}-B_{j-\frac{1}{2}}\frac{H_j-H_{j-1}}{\Delta\psi_j}+C_{j+\frac{1}{2}}\frac{U_{j+1}-U_j}{\Delta\psi_{j+1}}-C_{j-\frac{1}{2}}\frac{U_j-U_{j-1}}{\Delta\psi_j}]\right\}_i$$
$$=\frac{H_{i,j}-H_{i-1,j}}{\Delta x}$$
$$(4.26)$$

where $A_{i,j\pm\frac{1}{2}}=\frac{1}{2}(A_{i,j}+A_{i,j\pm\frac{1}{2}})$ and similar forms for $B_{i,j\pm\frac{1}{2}}$ and $C_{i,j\pm\frac{1}{2}}$.

At r=0, the momentum equation is,

$$\left\{\frac{\partial}{\partial\psi}[A\frac{\partial U}{\partial\psi}]\right\}_{i,1}=\left(\frac{\partial U}{\partial x}\right)_{i,1}$$

The left side of this equation is differenced using half the grid spacing at the centerline (see figure 4.2):

$$\left\{\frac{1}{\frac{\Delta\psi_2}{2}}[(A\frac{\partial U}{\partial\psi})_{1+\frac{1}{2}}-\underbrace{(A\frac{\partial U}{\partial\psi})_1}_{=0}]\right\}_i=\frac{U_{i,1}-U_{i-1,1}}{\Delta x}$$

From centerline boundary condition (equation 4.22), the second term in the left side is zero, thus

$$\left\{\frac{1}{\frac{\Delta\psi_2}{2}}[A_{1+\frac{1}{2}}\frac{U_2-U_1}{\Delta\psi_2}]\right\}_i=\frac{U_{i,1}-U_{i-1,1}}{\Delta x} \qquad (4.27)$$

Similarly for the energy equation,

$$\left\{\frac{1}{\frac{\Delta\psi_2}{2}}[B_{1+\frac{1}{2}}\frac{H_2-H_1}{\Delta\psi_2}+C_{1+\frac{1}{2}}\frac{U_2-U_1}{\Delta\psi_2}]\right\}_i=\frac{H_{i,1}-H_{i-1,1}}{\Delta x} \tag{4.28}$$

The outer boundary condition is represented by,

$$U_{i,N+1}=U_{i,N} \quad \text{and} \quad H_{i,N+1}=H_{i,N} \tag{4.29}$$

Equations 4.25-4.29 can be written in matrix form (for $N+1$ points in r-direction) as,

$$\{\mathbf{D}_j\,\mathbf{q}_{j-1}+\mathbf{E}_j\,\mathbf{q}_j+\mathbf{F}_j\,\mathbf{q}_{j+1}\}_i=\mathbf{q}_{i-1,j} \qquad j=1,2,3,\ldots,N \tag{4.30}$$

where

$$\mathbf{q}_{i,j}=\begin{Bmatrix}U_{i,j}\\ H_{i,j}\end{Bmatrix} \tag{4.31}$$

$$\begin{aligned}\mathbf{D}_{i,j}&=\mathbf{0} && j=1\\ &=\begin{pmatrix}-\Delta_j^- A_{j-\frac{1}{2}} & 0\\ -\Delta_j^- B_{j-\frac{1}{2}} & -\Delta_j^- B_{j-\frac{1}{2}}\end{pmatrix}_i && j>1\end{aligned} \tag{4.32}$$

$$\begin{aligned}\mathbf{E}_{i,j}&=\begin{pmatrix}1+\frac{2\Delta x}{\Delta\psi_2^2}A_{1+\frac{1}{2}} & 0\\ \frac{2\Delta x}{\Delta\psi_2^2}C_{1+\frac{1}{2}} & 1+\frac{2\Delta x}{\Delta\psi_2^2}B_{1+\frac{1}{2}}\end{pmatrix}_i && j=1\\ &=\begin{pmatrix}1+\Delta_j^- A_{j-\frac{1}{2}}+\Delta_j^+ A_{j+\frac{1}{2}} & 0\\ \Delta_j^- C_{j-\frac{1}{2}}+\Delta_j^+ C_{j+\frac{1}{2}} & 1+\Delta_j^- B_{j-\frac{1}{2}}+\Delta_j^+ B_{j+\frac{1}{2}}\end{pmatrix}_i && j>1\end{aligned} \tag{4.33}$$

$$\mathbf{F}_{i,j}=\begin{pmatrix}-\dfrac{2\Delta x}{\Delta\psi_2^2}A_{1+\frac{1}{2}} & 0\\ -\dfrac{2\Delta x}{\Delta\psi_2^2}C_{1+\frac{1}{2}} & -\dfrac{2\Delta x}{\Delta\psi_2^2}B_{1+\frac{1}{2}}\end{pmatrix}_i \qquad j=1$$

$$=\begin{pmatrix}-\Delta_j^+A_{j+\frac{1}{2}} & 0\\ -\Delta_j^+C_{j+\frac{1}{2}} & -\Delta_j^+B_{j+\frac{1}{2}}\end{pmatrix}_i \qquad j>1 \tag{4.34}$$

$$\Delta_j^-=\frac{2\Delta x}{\Delta\psi_j(\Delta\psi_j+\Delta\psi_{j+1})},\qquad \Delta_j^+=\frac{2\Delta x}{\Delta\psi_{j+1}(\Delta\psi_j+\Delta\psi_{j+1})} \tag{4.35}$$

A block tridiagonal system is formed as,

$$\begin{pmatrix}E_1 & F_1 & 0 & \cdots & 0\\ D_2 & E_2 & F_2 & 0 & \vdots\\ 0 & \ddots & \ddots & \ddots & 0\\ \vdots & \ddots & D_{N-1} & E_{N-1} & F_{N-1}\\ 0 & \cdots & 0 & D_N & E_N\end{pmatrix}\begin{Bmatrix}\mathbf{q}_1\\ \mathbf{q}_2\\ \vdots\\ \mathbf{q}_{N-1}\\ \mathbf{q}_N\end{Bmatrix}_i=\begin{Bmatrix}\mathbf{q}_1\\ \mathbf{q}_2\\ \vdots\\ \mathbf{q}_{N-1}\\ \mathbf{q}_N-\mathbf{F}_N\mathbf{q}_\infty\end{Bmatrix}_{i-1} \tag{4.36}$$

This is a 2x2 block tridiagonal system for $j=1$ to N. It can be solved by any standard block tridiagonal routine (e.g. Thomas Algorithm). The marching technique is used to solve the governing parabolic equations. The solution procedure for each station 'i' is as follows

1. Use $U_{i-1,j}$ and $H_{i-1,j}$ as an initial guess for $U_{i,j}$ and $H_{i,j}$, respectively.
2. Solve for ρ_m, μ_{eff}, and Pr_{eff} profiles.
3. Calculate $\Delta\psi_{i,j}$ using equation 4.24.
4. Solve the block tridiagonal system for new values of U and H. Also, new values of ρ_m, μ_{eff}, and Pr_{eff} are calculated.
5. If the difference between the new solution and the previous solution is smaller than some convergence criterion, then the axial step is completed. Otherwise, the iteration process continues at step 3.

4.2.6 Initial Profile

The jet exit velocity and enthalpy profiles are represented by

$$U = [\frac{1+U_\infty}{2} - \frac{1-U_\infty}{2} \tanh(\beta(r - r_{0.5}))] \tag{4.37}$$

$$H = [\frac{H_j + H_\infty}{2} - \frac{H_j - H_\infty}{2} \tanh(\beta^*(r - r_{0.5}^*))] \tag{4.38}$$

where

H_j is the jet exit enthalpy at the centerline,

U_∞, H_∞ are free stream values,

β, β^* are parameters that determine the shape of the velocity and enthalpy profiles,

$r_{0.5}, r_{0.5}^*$ are the radial locations where $U=(1+U_\infty)/2$ and $H=(H_j+H_\infty)/2$, respectively.

4.3 Stability Analysis

4.3.1 Governing Equations

Using parallel flow assumption $\vec{V} = (U(r),0,0)$ and constant mean pressure, the linearized Euler equations in cylindrical coordinates are:

$$\frac{\partial \rho}{\partial t} + U\frac{\partial \rho}{\partial x} + \rho_m \frac{\partial u}{\partial x} + \frac{1}{r}\frac{\partial (r\rho_m v)}{\partial r} + \frac{\rho_m}{r}\frac{\partial w}{\partial \theta} = 0 \tag{4.39}$$

$$\frac{\partial u}{\partial t} + U\frac{\partial u}{\partial x} + v\frac{\partial U}{\partial r} = -\frac{1}{\rho_m}\frac{\partial p}{\partial x} \tag{4.40}$$

$$\frac{\partial v}{\partial t} + U\frac{\partial v}{\partial x} = -\frac{1}{\rho_m}\frac{\partial p}{\partial r} \tag{4.41}$$

$$\frac{\partial w}{\partial t} + U\frac{\partial w}{\partial x} = -\frac{1}{r\rho_m}\frac{\partial p}{\partial \theta} \tag{4.42}$$

$$\frac{\partial p}{\partial t}+U\frac{\partial p}{\partial x}+\gamma P\left(\frac{\partial u}{\partial x}+\frac{1}{r}\frac{\partial (rv)}{\partial r}+\frac{1}{r}\frac{\partial w}{\partial \theta}\right) =0 \qquad (4.43)$$

Substitute $\lfloor \rho \quad u \quad v \quad w \quad p \rfloor = \lfloor \tilde{\rho} \quad \tilde{u} \quad \tilde{v} \quad \tilde{w} \quad \tilde{p} \rfloor e^{i(\alpha x+n\theta-\omega t)}$ and rearrange to obtain all variables as function of p,

$$\rho=\frac{\rho_m}{M_j^2}p-\frac{\dfrac{d\rho_m}{dr}}{i\,(\omega-\alpha\, U)}v \qquad (4.44)$$

$$u=\frac{\dfrac{dU}{dr}v+\dfrac{i\,\alpha}{\rho_m}p}{i\,(\omega-\alpha U\,)} \qquad (4.45)$$

$$v=\frac{\dfrac{dp}{dr}}{i\,\rho_m\,(\,\omega-\alpha U)} \qquad (4.46)$$

$$w=\frac{n\,p}{r\,\rho_m\,(\,\omega-\alpha U\ \,)} \qquad (4.47)$$

Using these relations in the energy equation, the compressible Rayleigh equation is obtained as,

$$\frac{d^2p}{dr^2}+\left\{\frac{1}{r}-\frac{1}{\rho_m}\frac{d\rho_m}{dr}+\frac{2\alpha}{\omega-\alpha U}\frac{dU}{dr}\right\}\frac{dp}{dr}+\left\{\rho_m M_j^2(\omega-\alpha U)^2-\frac{n^2}{r^2}-\alpha^2\right\}p=0 \qquad (4.48)$$

4.3.2 Boundary Conditions

Since the Rayleigh equation is singular at r=0, a new form is obtained at the centerline using Taylor series expansion for p and dp/dr to remove the singularity as follows:

$$p = p_0 + r\left(\frac{dp}{dr}\right)_0 + \frac{r^2}{2}\left(\frac{d^2p}{dr^2}\right)_0 + \cdots \tag{4.49}$$

$$\frac{dp}{dr} = \left(\frac{dp}{dr}\right)_0 + r\left(\frac{d^2p}{dr^2}\right)_0 + \cdots \tag{4.50}$$

The Rayleigh equation at *r=0* reduces to

$$\begin{gathered}(2-\frac{n^2}{2})\left(\frac{d^2p}{dr^2}\right)_0 + \left\{\frac{(1-n^2)}{r} - \frac{1}{\rho_m}\frac{d\rho_m}{dr} + \frac{2\alpha}{\omega-\alpha U}\frac{dU}{dr}\right\}\left(\frac{dp}{dr}\right)_0 \\ + \left\{\rho_m M_j^2(\omega-\alpha U)^2 - \frac{n^2}{r^2} - \alpha^2\right\}p_0 = 0\end{gathered} \tag{4.51}$$

The conditions to remove the singularity at *r=0* are:

(1) for $n=0$:

The first derivative must vanish; that is, $(dp/dr)_0 = 0$, and the equation reduces to,

$$2\left(\frac{d^2p}{dr^2}\right)_0 + \{\rho_m M_j^2(\omega-\alpha U)^2 - \alpha^2\}p_0 = 0 \tag{4.52}$$

(2) for $|n|=1$:

The centerline pressure must vanish; that is, $p_0 = 0$, and the equation reduces to,

$$\frac{3}{2}\left(\frac{d^2p}{dr^2}\right)_0 + \left\{-\frac{1}{\rho_m}\frac{d\rho_m}{dr} + \frac{2\alpha}{\omega-\alpha U}\frac{dU}{dr}\right\}\left(\frac{dp}{dr}\right)_0 = 0 \tag{4.53}$$

(3) for $|n|=2$:

The second-order derivative disappears from the equation ($(d^2p/dr^2)_0 \neq 0$) and both the centerline pressure and the first derivative must vanish; that is, $p_0 = 0$ and $(dp/dr)_0 = 0$.

(4) for $|n|>2$:

Both the centerline pressure and the first derivative must vanish; that is, $p_0 = 0$ and $(dp/dr)_0 = 0$, and the equation reduces to,

$$\left(\frac{d^2 p}{dr^2}\right)_0 = 0 \tag{4.54}$$

Thus, the boundary conditions are

For $n=0$: $$\left(\frac{dp}{dr}\right)_{r=0} = 0 \quad \& \quad (p)_{r\to\infty} = 0 \tag{4.55-a}$$

For $|n|=1$: $$(p)_{r=0} = 0 \quad \& \quad (p)_{r\to\infty} = 0 \tag{4.55-b}$$

For $|n|\geq 2$: $$(p)_{r=0} = 0, \quad \left(\frac{dp}{dr}\right)_{r=0} = 0 \quad \& \quad (p)_{r\to\infty} = 0 \tag{4.55-c}$$

It is noted here that the second boundary condition at *r=0* for $|n|\geq 2$ will replace the governing equation at the centerline, i.e. this equation is no longer needed at *r=0*.

4.3.3 Computational Method

Rayleigh equation is solved using fourth-order Runge-Kutta scheme as follows:

Defining $\mathbf{F} = \lfloor p \quad dp/dr \rfloor$, the Rayleigh equation can be written as

$$\frac{d\mathbf{F}}{dr} = \begin{pmatrix} 0 & 1 \\ a_1 & a_2 \end{pmatrix}\mathbf{F} \tag{4.56}$$

where

$$a_1 = \begin{cases} -[\rho_m M_j^2 (\omega - \alpha U)^2 - \alpha^2]/(2 - \frac{n^2}{2}) & r = 0 \;\&\; n \neq 2 \\ -[\rho_m M_j^2 (\omega - \alpha U)^2 - \frac{n^2}{r^2} - \alpha^2] & r \neq 0 \end{cases} \tag{4.57}$$

$$a_2 = \begin{cases} -[-\dfrac{1}{\rho_m}\dfrac{d\rho_m}{dr} + \dfrac{2\alpha}{\omega-\alpha U}\dfrac{dU}{dr}]/(2-\dfrac{n^2}{2}) & r=0\ \&\ n \neq 2 \\ -[\dfrac{1}{r} - \dfrac{1}{\rho_m}\dfrac{d\rho_m}{dr} + \dfrac{2\alpha}{\omega-\alpha U}\dfrac{dU}{dr}] & r \neq 0 \end{cases} \tag{4.58}$$

For $n=0$ or $|n|=1$, starting at $r=0$, either dp/dr or p is known (refer to equation 4.55). The unknown variable at the centerline, i.e. p for $n=0$ and dp/dr for $|n|=1$, is used as normalization constant. For $|n| \geq 2$, starting at $r=rmax$, p is known (refer to equation 4.55). The unknown variable at $r=rmax$, i.e. dp/dr, is used as normalization constant. Thus, the solution vector, **F**, is initialized as follows:

At $r=0$: $$\mathbf{F} = \begin{Bmatrix} 1 \\ 0 \end{Bmatrix} \text{ for } n=0 \quad \text{Or} \quad \mathbf{F} = \begin{Bmatrix} 0 \\ 1 \end{Bmatrix} \text{ for } |n|=1 \tag{4.59}$$

At $r=rmax$: $$\mathbf{F} = \begin{Bmatrix} 0.00001 \\ 1 \end{Bmatrix} \text{ for } |n| \geq 2 \tag{4.60}$$

Assuming both ω and α are known, the solution proceeds along r-direction using Runge-Kutta integration formula:

$$\mathbf{F} = \mathbf{F}_0 + \frac{1}{6}(\mathbf{k}_1 + 2\mathbf{k}_2 + 2\mathbf{k}_3 + \mathbf{k}_4)\Delta r \tag{4.61}$$

where

$\mathbf{F}_0$ is the value at r,

$\mathbf{F}$ is the value at $r+\Delta r$,

$$\mathbf{k}_1 = \left(\frac{d\mathbf{F}}{dr}\right)_{r,\mathbf{F}_0}$$

$$\mathbf{k}_2 = \left(\frac{d\mathbf{F}}{dr}\right)_{r+\frac{1}{2}\Delta r,\mathbf{F}_0+\frac{1}{2}\Delta r\mathbf{k}_1}$$

$$\mathbf{k}_3 = \left(\frac{d\mathbf{F}}{dr}\right)_{r+\frac{1}{2}\Delta r,\mathbf{F}_0+\frac{1}{2}\Delta r\mathbf{k}_2}$$

$$\mathbf{k}_4 = \left(\frac{d\mathbf{F}}{dr}\right)_{r+\Delta r,\mathbf{F}_0+\Delta r\mathbf{k}_3}$$

Since only ω is given, the solution has an iterative nature where α is guessed and refined aiming at the satisfaction of the other boundary conditions.

4.4 Acoustic Field Analysis

4.4.1 Governing Equations

For the acoustic field, the linearized Euler equations are considered in conservation form and in the cylindrical coordinates:

$$\frac{\partial\tilde{\mathbf{Q}}}{\partial t}+\frac{\partial\tilde{\mathbf{F}}}{\partial x}+\frac{1}{r}\frac{\partial\left(r\tilde{\mathbf{G}}\right)}{\partial r}+\frac{1}{r}\frac{\partial\tilde{\mathbf{H}}}{\partial\theta}=\frac{\tilde{\mathbf{S}}}{r} \tag{4.62}$$

where

$$\tilde{\mathbf{Q}}=\begin{Bmatrix}\tilde{\rho}\\ \tilde{u}\\ \tilde{v}\\ \tilde{w}\\ \tilde{e}\end{Bmatrix}=\begin{Bmatrix}\rho'\\ (\rho u)'\\ (\rho v)'\\ (\rho w)'\\ (\rho e)'\end{Bmatrix} \tag{4.63}$$

$$\tilde{\mathbf{F}}=\begin{Bmatrix}\tilde{u}\\ (\tilde{u}-\tilde{\rho}U)U+U\tilde{u}+p'\\ (\tilde{v}-\tilde{\rho}V)U+V\tilde{u}\\ (\tilde{w}-\tilde{\rho}W)U+W\tilde{u}\\ U(p'+\tilde{e})+(\tilde{u}-\tilde{\rho}U)(E+P/\rho_m)\end{Bmatrix} \tag{4.64}$$

$$\tilde{\mathbf{G}}=\left\{\begin{matrix} \tilde{v} \\ (\tilde{u}-\tilde{\rho}U)\,V+U\,\tilde{v} \\ (\tilde{v}-\tilde{\rho}V)V+V\,\tilde{v}+p' \\ (\tilde{w}-\tilde{\rho}W)V+W\,\tilde{v} \\ V(p'+\tilde{e})+(\tilde{v}-\tilde{\rho}V)(E+P/\rho_m) \end{matrix}\right\} \tag{4.65}$$

$$\tilde{\mathbf{H}}=\left\{\begin{matrix} \tilde{w} \\ (\tilde{u}-\tilde{\rho}U)W+U\,\tilde{w} \\ (\tilde{v}-\tilde{\rho}V)W+V\,\tilde{w} \\ (\tilde{w}-\tilde{\rho}W)W+W\,\tilde{w}+p' \\ W(p'+\tilde{e})+(\tilde{w}-\tilde{\rho}W)(E+P/\rho_m) \end{matrix}\right\} \tag{4.66}$$

and

$$\tilde{\mathbf{S}}=\left\{\begin{matrix} 0 \\ 0 \\ (\tilde{w}-\tilde{\rho}W)W+W\,\tilde{w}+p' \\ (\tilde{w}-\tilde{\rho}W)\,V+W\,\tilde{v} \\ 0 \end{matrix}\right\} \tag{4.67}$$

All the velocities are normalized by the centerline velocity at the jet exit plane U_j, time by R_j/U_j, density by the jet centerline value ρ_j, and pressure by $\rho_j\, U_j^2$. For the sake of computational efficiency, the flow variables are decomposed in the azimuthal direction as,

$$\left\{\begin{matrix} \rho' \\ u' \\ v' \\ w' \\ p' \end{matrix}\right\}=\mathrm{Re}\left(\left\{\begin{matrix} \rho(x,r,t) \\ u(x,r,t) \\ v(x,r,t) \\ w(x,r,t) \\ p(x,r,t) \end{matrix}\right\} e^{in\theta}\right), \tag{4.68}$$

where ρ,u,v,w and p are complex variables. This yields a set of equations that includes all three components of the acoustic velocity field, but the partial derivatives are only in the axial and the radial directions:

$$\frac{\partial \breve{\mathbf{Q}}}{\partial t}+\frac{\partial \breve{\mathbf{F}}}{\partial x}+\frac{1}{r}\frac{\partial\left(r\breve{\mathbf{G}}\right)}{\partial r}+\frac{in}{r}\breve{\mathbf{H}}=\frac{\breve{\mathbf{S}}}{r} \tag{4.69}$$

where $\breve{\mathbf{Q}}$, $\breve{\mathbf{F}}$, $\breve{\mathbf{G}}$, and $\breve{\mathbf{S}}$ are similar to those in equation 4.62 except that all primes are now removed, i.e., the variables are complex. These equations are then transformed into the generalized curvilinear coordinates,

$$\frac{\partial \hat{\mathbf{Q}}}{\partial t}+\frac{\partial \hat{\mathbf{F}}}{\partial \xi}+\frac{\partial \hat{\mathbf{G}}}{\partial \eta}=\frac{\hat{\mathbf{S}}}{r} \tag{4.70}$$

where $\hat{\mathbf{Q}}$ is the vector of conserved complex variables, $\hat{\mathbf{F}}$ and $\hat{\mathbf{G}}$ are the contravariant fluxes, and $\hat{\mathbf{S}}$ contains the azimuthal flux and the source terms:

$$\hat{\mathbf{Q}}=\frac{\breve{\mathbf{Q}}}{J}=\frac{1}{J}\begin{Bmatrix}\breve{\rho}\\ \breve{u}\\ \breve{v}\\ \breve{w}\\ \breve{e}\end{Bmatrix}=\frac{1}{J}\begin{Bmatrix}\rho\\ \rho_m u+\rho U\\ \rho_m v+\rho V\\ \rho_m w+\rho W\\ \rho_m e+\rho E\end{Bmatrix} \tag{4.71}$$

$$\hat{\mathbf{F}}=\frac{1}{J}(\xi_x\breve{\mathbf{F}}+\xi_r\breve{\mathbf{G}})=\frac{1}{J}\begin{Bmatrix}\hat{u}\\ (\breve{u}-\breve{\rho}U)\hat{U}+U\hat{u}+\xi_x p\\ (\breve{v}-\breve{\rho}V)\hat{U}+V\hat{u}+\xi_r p\\ \breve{w}\hat{U}\\ (p+\breve{e})\hat{U}+(\hat{u}-\breve{\rho}U)(E+P/\rho_m)\end{Bmatrix} \tag{4.72}$$

$$\hat{\mathbf{G}}=\frac{1}{J}(\eta_x\breve{\mathbf{F}}+\eta_r\breve{\mathbf{G}})=\frac{1}{J}\begin{Bmatrix}\hat{v}\\ (\breve{u}-\rho U)\hat{V}+U\hat{v}+\eta_x p\\ (\breve{v}-\rho V)\hat{V}+V\hat{v}+\eta_r p\\ \breve{w}\hat{V}\\ (p+\breve{e})\hat{V}+(\hat{v}-\breve{\rho}\hat{V})(E+P/\rho_m)\end{Bmatrix} \tag{4.73}$$

$$\hat{\mathbf{S}} = \frac{1}{J}(\breve{\mathbf{S}} - \breve{\mathbf{G}} - in\breve{\mathbf{H}}) = -\frac{1}{J}\left\{\begin{matrix} \hat{v} + in\breve{w} \\ (\breve{u} - \breve{\rho}U)V + U(\hat{v} + in\breve{w}) \\ (2\breve{v} - \breve{\rho}V)V + inV\breve{w} \\ inp \\ (p + \breve{e})V + (\hat{v} - \breve{\rho}V + in\breve{w})(E + P/\rho_m) \end{matrix}\right\} \tag{4.74}$$

$$p = (\gamma - 1)\left[\breve{e} - (\breve{u}U + \breve{v}V) + \frac{1}{2}\breve{\rho}(U^2 + V^2)\right] \tag{4.75}$$

$$P = (\gamma - 1)\rho\left[E - \frac{1}{2}(U^2 + V^2)\right] \tag{4.76}$$

$$\left.\begin{aligned} \hat{U} &= \xi_x U + \xi_r V, \\ \hat{V} &= \eta_x U + \eta_r V, \\ \hat{u} &= \xi_x \breve{u} + \xi_r \breve{v}, \\ \hat{v} &= \eta_x \breve{u} + \eta_r \breve{v} \end{aligned}\right\} \tag{4.77}$$

4.4.2 Computational Method

By virtue of the transformation 4.68, equation 4.70 could be solved in the x-r plane only. Note that the mean flow considered herein is axisymmetric. The linearized Euler equations are solved using the fourth-order DRP scheme. The present central-difference scheme includes artificial dissipation to overcome the expected spurious oscillations. The discretized form of equation 4.70 is

$$\left(\frac{\partial \hat{\mathbf{Q}}}{\partial t}\right)^n_{\ell,m} = -\frac{1}{\Delta\xi}\sum_{k=-3}^{3} a_k \hat{\mathbf{F}}^n_{\ell+k,m} - \frac{1}{\Delta\eta}\sum_{k=-3}^{3} a_k \hat{\mathbf{G}}^n_{\ell,m+k} + \frac{\hat{\mathbf{S}}^n_{\ell,m}}{r} + \hat{\mathbf{D}}^n_{\ell,m} \tag{4.78}$$

where

$$\hat{\mathbf{D}}^n_{\ell,m} = -\frac{\mu_a}{J}\sum_{k=-3}^{3} d_k (\mathbf{Q}^n_{\ell+k,m} + \mathbf{Q}^n_{\ell,m+k}) \tag{4.79}$$

ℓ and m are the spatial indices and n indicates the time level. The coefficients a_k and d_k are given in Appendix A.

4.4.3 Flow Adapted Grid

A Flow adapted grid is generated using the transformations:

$$\xi = x \quad and \quad \eta = r + N\,\Delta\eta\,(1-\bar{U}) \tag{4.80}$$

where N is the number of grid points inside the mixing layer and $\bar{U}$ is the analytical functions obtained by curve fitting of the mean flow axial velocity. The '*tanh*' function is used for curve fitting in the form,

$$\bar{U} = a_1 - a_2 \tanh(a_3(r - a_4)) \tag{4.81}$$

where the coefficients a_i are obtained using least-squares fitting technique after applying Gauss-Newton method to linearize the *tanh* equation. The resulting system of equations is,

$$[\mathbf{Z}]^T[\mathbf{Z}]\{\Delta\mathbf{A}\} = [\mathbf{Z}]^T\{\mathbf{U}-\bar{\mathbf{U}}) \tag{4.82}$$

where

$$[\mathbf{Z}]_{j\,\max\times 4} = \begin{pmatrix} \left(\frac{\partial\bar{U}}{\partial a_1}\right)_1 & \left(\frac{\partial\bar{U}}{\partial a_2}\right)_1 & \left(\frac{\partial\bar{U}}{\partial a_3}\right)_1 & \left(\frac{\partial\bar{U}}{\partial a_4}\right)_1 \\ \left(\frac{\partial\bar{U}}{\partial a_1}\right)_2 & \left(\frac{\partial\bar{U}}{\partial a_2}\right)_2 & \left(\frac{\partial\bar{U}}{\partial a_3}\right)_2 & \left(\frac{\partial\bar{U}}{\partial a_4}\right)_2 \\ \vdots & \vdots & \vdots & \vdots \\ \left(\frac{\partial\bar{U}}{\partial a_1}\right)_{j\max} & \left(\frac{\partial\bar{U}}{\partial a_2}\right)_{j\max} & \left(\frac{\partial\bar{U}}{\partial a_3}\right)_{j\max} & \left(\frac{\partial\bar{U}}{\partial a_4}\right)_{j\max} \end{pmatrix},$$

$\{\Delta\mathbf{A}\} = \lfloor \Delta a_1 \quad \Delta a_2 \quad \Delta a_3 \quad \Delta a_4 \rfloor^T$,

$\mathbf{U} = \lfloor U_1 \quad U_2 \quad \cdots \quad U_{j\max} \rfloor^T$ is the actual velocity profile vector,

$\bar{\mathbf{U}} = \lfloor \bar{U}_1 \quad \bar{U}_2 \quad \cdots \quad \bar{U}_{j\max} \rfloor^T$ is the fitted velocity profile vector,

$$\frac{\partial \overline{U}}{\partial a_1}=1,\quad \frac{\partial \overline{U}}{\partial a_2}=-\tanh(a_3(r-a_4)),$$
$$\frac{\partial \overline{U}}{\partial a_3}=\frac{-a_2(r-a_4)}{\cosh^2(a_3(r-a_4))},\quad \frac{\partial \overline{U}}{\partial a_4}=\frac{a_2a_3}{\cosh^2(a_3(r-a_4))}$$

and *jmax* is the number of points in the velocity profile (number of grid points in r-direction).

Starting with an initial guess of the coefficients a_i, equation 4.82 is solved for the incremental change of these coefficients and the new values are obtained. The process is repeated until convergence. The procedure starts at the jet inlet, where the velocity profile is imposed as *tanh* function. Moving downstream, the initial guess of the *tanh* function coefficients is taken from the previous station. The procedure is fast and takes only minutes to generate the complete set of *tanh* functions that represent the axial mean flow velocity. The coefficients, a_i, are then smoothed in x-direction and used to obtain the Jacobian of the transformation:

$$J=\frac{\partial(\xi,\eta)}{\partial(x,r)}=\begin{pmatrix} 1 & 0 \\ -N\Delta\eta\dfrac{\partial \overline{U}}{\partial x} & 1-N\Delta\eta\dfrac{\partial \overline{U}}{\partial r}\end{pmatrix} \tag{4.83}$$

where

$$\frac{\partial \overline{U}}{\partial x}=\frac{\partial a_1}{\partial x}-\frac{\partial a_2}{\partial x}\tanh(a_3(r-a_4))-a_2\left(\frac{\partial a_3}{\partial x}(r-a_4)-a_3\frac{\partial a_4}{\partial x}\right)/\cosh^2(a_3(r-a_4)),$$

$$\frac{\partial \overline{U}}{\partial r}=-a_2a_3/\cosh^2(a_3(r-a_4)),$$

$\frac{\partial a_i}{\partial x}$ are obtained using the fourth-order DRP scheme.

4.4.4 Multiple Time Scales

For the present computations, which require rather long time integration, computational time savings are accomplished by extending the methodology for multiblock grids with multiple time scales. Shown in figure 4.3 is a representative multiblock grid, where four levels of time steps are used. A buffer zone is defined as the transition region between any two time-step blocks. As such, a modified DRP scheme (Webb, 1993) is implemented to update the buffer zones as follows:

$$f(t+\delta\Delta t) = f(t) + \Delta t \sum_{k=0}^{3} b_\ell^{(\delta)} \frac{\partial f}{\partial t}^{n-k} \qquad (4.84)$$

where $b_\ell^{(\delta)}$ are given in appendix A, $\delta = m/M$; m is the fractional time step index ($m=1,2,\ldots,M$), and M is the ratio of the time steps across the buffer.

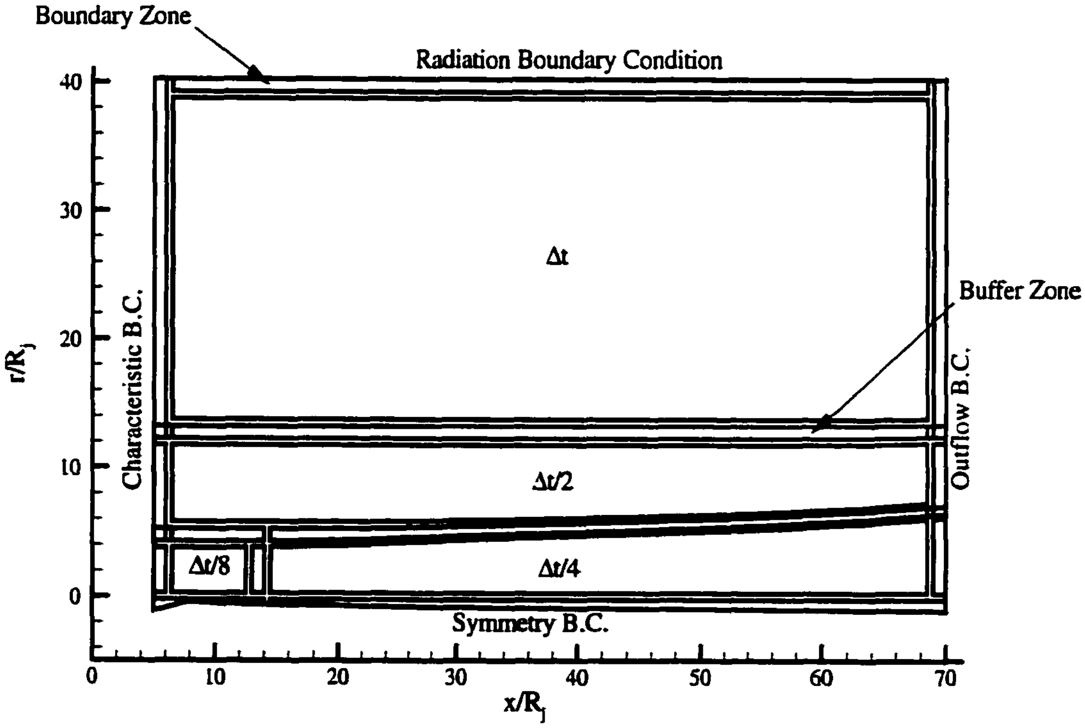
Boundary Zone
Radiation Boundary Condition
Δt
Buffer Zone
Δt/2
Δt/8
Δt/4
Symmetry B.C.
Characteristic B.C.
Outflow B.C.
r/R_j
x/R_j
0
10
20
30
40
50
60
70
0
10
20
30
40

Figure 4.3 Multi-block time integration zones.

The calculation cycle is determined by maximum time step, Δt. During each cycle, a block with a time step equalling $\Delta t/n$ is updated n-times, so that, at the end of the cycle all blocks are at the same time level. The buffer zone is updated with the minimum of the time steps for the block sharing that zone.

4.4.5 Boundary Conditions

Four types of boundary conditions are used for the boundaries shown in figure 4.3: characteristic inflow, radiation, centerline, and outflow. All the boundary conditions are written in terms of the primitive perturbation variables, ρ, u, v, w, and p. Once the time derivatives of these variables are determined, the transformation equations (derived later) are used to obtain the conservative variables at the boundaries.

4.4.5.1 Characteristic Inflow Boundary Condition

In the fluid disturbance region of the upstream boundary, the input disturbance, $\hat{\mathbf{Q}}_{disturbance}$ is introduced into the acoustic field using the following equation

$$\hat{\mathbf{Q}}_{boundary} = \hat{\mathbf{Q}}_{computed} + \hat{\mathbf{Q}}_{disturbance} \tag{4.85}$$

where $\hat{\mathbf{Q}}_{computed}$ is obtained using the one-dimensional characteristic inflow boundary condition in the curvilinear coordinates. The time derivative of $\hat{\mathbf{Q}}$ at the inflow boundary is decomposed into its components:

$$\hat{\mathbf{Q}}_t = -\hat{\mathbf{F}}_\xi - \hat{\mathbf{G}}_\eta + \frac{\hat{\mathbf{S}}}{r} = (\hat{\mathbf{Q}}_t)|_\xi + (\hat{\mathbf{Q}}_t)|_\eta + (\hat{\mathbf{Q}}_t)|_s \tag{4.86}$$

The ξ-operator is decomposed into five locally one-dimensional characteristics. The eigenvalues which determine the wave propagation direction are given by,

$$\boldsymbol{\lambda} = \begin{Bmatrix} U-C \\ U \\ U \\ U \\ U+C \end{Bmatrix} \tag{4.87}$$

and the eigenvectors which represent the characteristic relations are,

$$\mathbf{L} = \begin{Bmatrix} L_1 \\ L_2 \\ L_3 \\ L_4 \\ L_5 \end{Bmatrix} = \begin{Bmatrix} (p_t)|_\xi - \rho_m C\,(u_t)|_\xi \\ C^2\,(\rho_t)|_\xi - (p_t)|_\xi \\ (v_t)|_\xi \\ (w_t)|_\xi \\ (p_t)|_\xi + \rho_m C\,(u_t)|_\xi \end{Bmatrix} \tag{4.88}$$

The five characteristic relations are solved together to obtain the time derivatives of the variables at the inflow boundary,

$$(\mathbf{q}_t)|_\xi = \begin{Bmatrix} (\rho_t)|_\xi \\ (u_t)|_\xi \\ (v_t)|_\xi \\ (w_t)|_\xi \\ (p_t)|_\xi \end{Bmatrix} = \begin{Bmatrix} \dfrac{1}{C^2}(L_2 + \tfrac{1}{2}(L_5 + L_1)) \\ \dfrac{1}{2\rho_m C}(L_5 - L_1) \\ L_3 \\ L_4 \\ \tfrac{1}{2}(L_5 + L_1) \end{Bmatrix} \tag{4.89}$$

Then, the conserved variables $(\mathbf{Q}_t)|_\xi$ are assembled as follows:

$$(\mathbf{Q}_t)|_\xi = \begin{Bmatrix} \rho_t \\ \rho_m u_t + \rho_t U \\ \rho_m v_t + \rho_t V \\ \rho_m w_t \\ \dfrac{p_t}{\gamma-1} + (U\,\breve{u}_t + V\,\breve{v}_t) - \tfrac{1}{2}(U^2 + V^2)\,\rho_t \end{Bmatrix} \tag{4.90}$$

For a nonreflecting boundary condition, all the incoming waves are set to zero. For supersonic inflow ($U>C$), all characteristics are incoming and thus all L_i are set to zero. For subsonic flow ($U<C$), the first wave is outgoing, thus, L_1 is computed using the internal scheme, where the time derivatives of the conservative variables are calculated first. Then, the time derivative of the primitive variables are obtained by,

$$\begin{Bmatrix} \rho_t \\ u_t \\ v_t \\ w_t \\ p_t \end{Bmatrix} = \begin{Bmatrix} \breve{\rho} \\ (\breve{u} - U\rho_t)/\rho_m \\ (\breve{v} - V\rho_t)/\rho_m \\ \breve{w}/\rho_m \\ (\gamma-1)\left[\breve{e} - (U\breve{u}_t + V\breve{v}_t) + \frac{1}{2}(U^2+V^2)\rho_t\right] \end{Bmatrix} \tag{4.91}$$

The other four waves are incoming, so, $L_2=L_3=L_4=L_5=0$.

4.4.5.2 Radiation Boundary Condition

For the remainder of the upstream boundary and the far field boundary, the radiation boundary condition is used in the following form:

$$\frac{\partial \mathbf{q}}{\partial t} + \frac{V_g}{R}\left[(x\xi_x + r\xi_r)\frac{\partial \mathbf{q}}{\partial \xi} + (x\eta_x + r\eta_r)\frac{\partial \mathbf{q}}{\partial \eta} + \mathbf{q}\right] = 0 \tag{4.92}$$

where

$$V_g = \frac{x}{R}U + \frac{r}{R}V + \sqrt{C^2 - (\frac{x}{R}V + \frac{r}{R}U)^2} \tag{4.93}$$

and $\mathbf{q} = [\rho \quad u \quad v \quad w \quad p]^T$, $R = \sqrt{x^2 + r^2}$ and C is the mean flow speed of sound.

4.4.5.3 Outflow Boundary Condition

The outflow boundary treatment, used for the downstream boundary, is based on the asymptotic analysis of the linearized equations. They are obtained in cylindrical coordinates (x,r,θ), by first substituting the mean flow velocity vector for the axisymmetric jet $\vec{V}=(U,V,0)$ and the perturbation velocity vector $\vec{v}'=(u',v',w')$ into the governing equations. Then, using the mode decomposition, the following equations are obtained:

$$\frac{\partial \rho}{\partial t}+\hat{U}\frac{\partial \rho}{\partial \xi}+\hat{V}\frac{\partial \rho}{\partial \eta}=\frac{1}{C^2}(\frac{\partial p}{\partial t}+\hat{U}\frac{\partial p}{\partial \xi}+\hat{V}\frac{\partial p}{\partial \eta}) \tag{4.94}$$

$$\frac{\partial u}{\partial t}+\hat{U}\frac{\partial u}{\partial \xi}+\hat{V}\frac{\partial u}{\partial \eta}=\frac{1}{\rho_m}(\xi_x\frac{\partial p}{\partial \xi}+\eta_x\frac{\partial p}{\partial \eta}) \tag{4.95}$$

$$\frac{\partial v}{\partial t}+\hat{U}\frac{\partial v}{\partial \xi}+\hat{V}\frac{\partial v}{\partial \eta}=\frac{1}{\rho_m}(\xi_r\frac{\partial p}{\partial \xi}+\eta_r\frac{\partial p}{\partial \eta}) \tag{4.96}$$

$$\frac{\partial w}{\partial t}+\hat{U}\frac{\partial w}{\partial \xi}+\hat{V}\frac{\partial w}{\partial \eta}+\frac{V\,w}{r}=-\frac{i\,n\,p}{r\rho_m} \tag{4.97}$$

$$\frac{\partial p}{\partial t}+\frac{V_g}{R}\left[(x\xi_x+r\xi_r)\frac{\partial p}{\partial \xi}+(x\eta_x+r\eta_r)\frac{\partial p}{\partial \eta}+p\right]=0 \tag{4.98}$$

4.4.5.4 Centerline Boundary Condition

Due to the helical pattern of the disturbances, only half of the domain needs to be considered. Then, a centerline treatment should be invoked. As the central spatial derivative stencil uses three points on each side, computing η-derivatives along the centerline requires data values at three points below the centerline. For the axisymmetric mode calculations, the centerline boundary condition for $j=1,2,3$ is,

$$\left.\begin{array}{ll} \rho(i,-j)=\rho(i,-j) & p(i,-j)=p(i,j) \\ u(i,-j)=u(i,j) & v(i,-j)=-v(i,j) \end{array}\right\} \tag{4.99}$$

For the helical mode calculations, the centerline boundary condition for $j=1,2,3$ is,

$$\left.\begin{array}{ll} \rho(i,-j)=-\rho(i,-j) & p(i,-j)=-p(i,j) \\ u(i,-j)=-u(i,j) & v(i,-j)=v(i,j) \\ w(i,-j)=w(i,j) & \end{array}\right\} \qquad (4.100)$$

4.5 Mean Flow Results

Troutt and Mclaughlin (T&M) used a jet of 0.01 m diameter. Jet exit conditions were Mach number, M_j =2.1, Reynolds number, Re_j=70000, and stagnation temperature, T_0=294° k. In Appendix C, Gaussian curves are used to fit the axial velocity profiles. Measured data and conservation of axial momentum are used to calculate the Gaussian curve parameters. These empirical results will be compared with the present computations.

The marching procedure described in section 4.2.5 is used to obtain the mean flow field. The initial velocity profile is a *tanh* curve with β=10 and $r_{0.5}$=0.95. The inlet enthalpy is uniform and equals the product $C_p\ T_0$. The computational domain extends axially to 70 radii and radially to 40 radii. A uniform grid of 3500×2000 points is used. This gives a mesh size of 0.02 R_j in both directions.

Figure 4.4 shows the empirical and computed Mach numbers at different axial locations (x/R_j=0, 10, 20, 30, 40, 60). The empirical solution is described in Appendix C. Also shown in this figure are the centerline velocity variations with the axial distance. The radial velocity at the same axial locations is plotted in figure 4.5. Both laminar and turbulent calculations are conducted. The turbulence model parameters are due to Dahl and Morris (1997).

For the current example, the turbulent viscosity has much stronger effect than the laminar viscosity. The laminar centerline velocity is approximately constant and can not represent the actual variation of the centerline velocity. Also, a slow spreading rate is observed for the laminar solution. The turbulent solution is in good agreement with the experimental results.

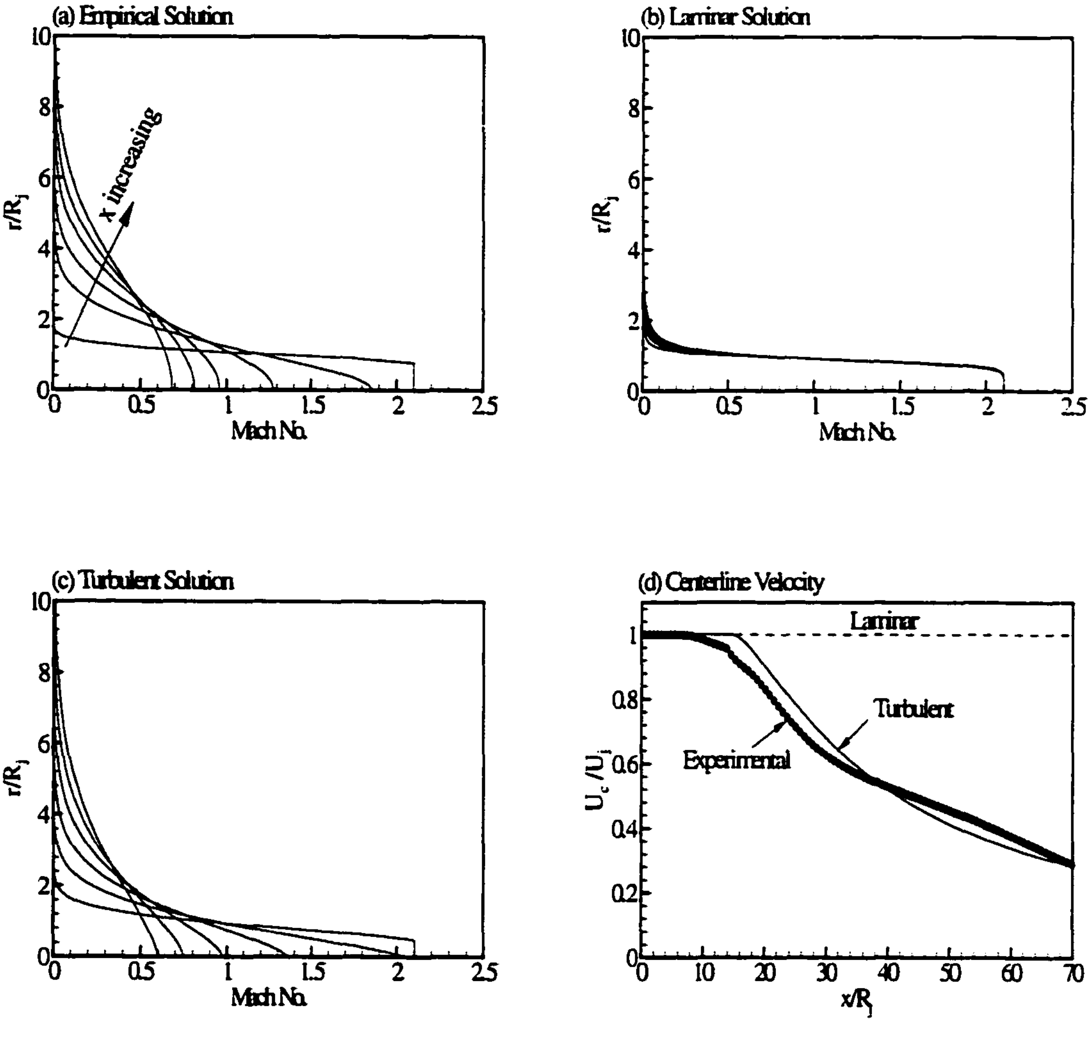

Figure 4.4 Mach number and centerline velocity of T&M Mach 2.1 jet.

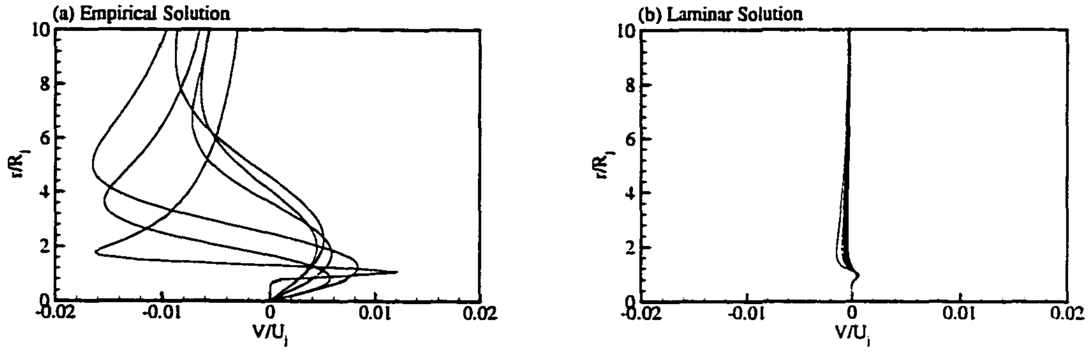

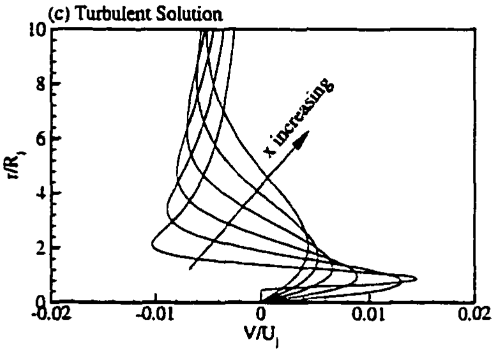

Figure 4.5 Radial velocity of T&M Mach 2.1 jet.

4.6 Stability Results

The purpose of the stability analysis is to obtain the eigenfunctions for a given Strouhal number. Since these functions are only needed at jet inlet, the inlet *tanh* profile is only considered. The grid extends to 20 radii with 300 points. It is clustered near the critical layer, $r=1$. Figure 4.6 shows the variation of growth rate and phase speed with Strouhal number. The amplitude of the eigen functions for $St=0.2$ are also shown in this figure. The computations are performed for two azimuthal wave numbers, $n=0$ and $n=1$. The growth rate of the helical mode is larger than that of the axisymmetric mode. For a given initial disturbance, the helical instability waves will have larger amplitude at the same axial location.

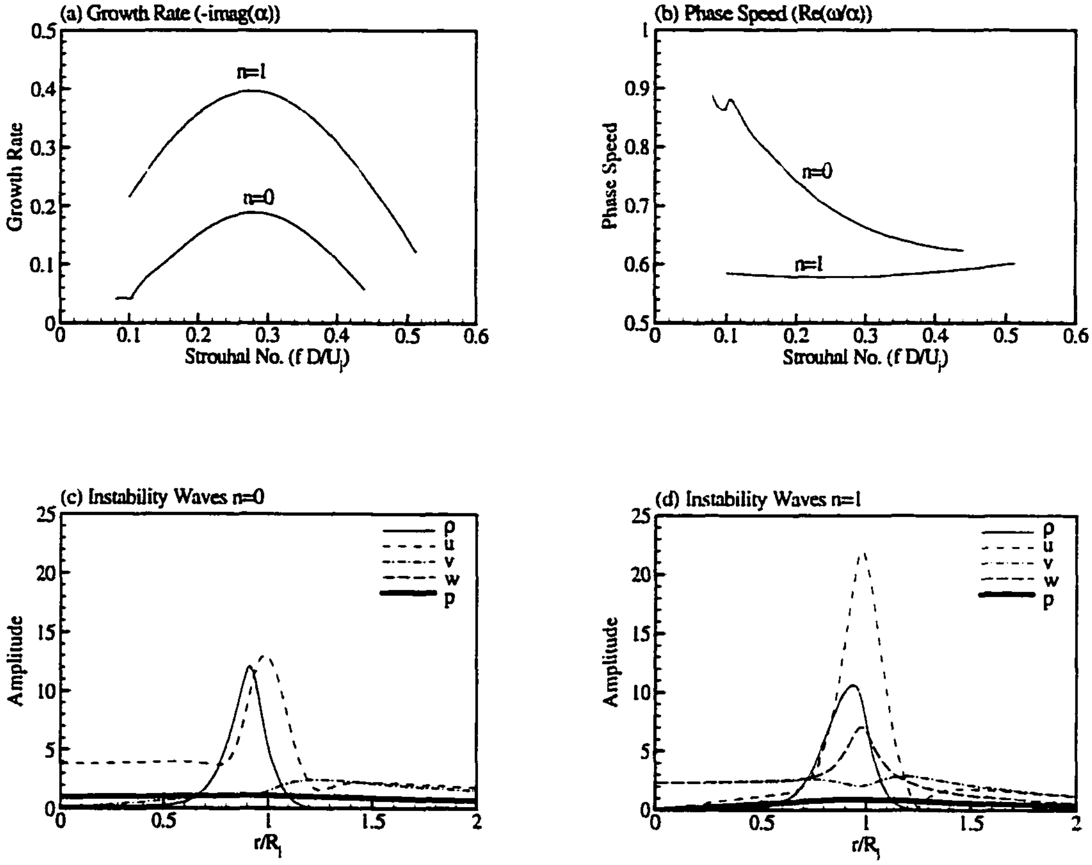

Figure 4.6 Instability wave solution. (a) Growth rate (-im(α)). (b) Phase speed Re(ω/α). (c) Radial distribution of waves amplitude for axisymmetric mode. (d) Radial distribution of waves amplitude for helical mode.

The phase speed determines the velocity at which the instability waves are moving. A dominant portion of supersonic jet noise is thought to be caused by the propagation of turbulent eddies with a convective velocity, which is supersonic with respect to the surrounding air stream. It has been discovered that there is a remarkable similarity between the behavior of these eddies and the instability waves. Consequently, supersonic phase speed relative to free stream indicates a strong emission of noise. The normalized free stream speed of sound is $\sqrt{\gamma RT_\infty}/U_j = 0.65$. The phase speed of the axisymmetric mode is above this value for most of the Strouhal number range. For the helical mode, the phase speed is highly subsonic (about 0.6). This suggests that the axisymmetric mode is more effective in noise generation. Large variations of the amplitude of the eigen functions are shown near the nozzle lip, r=1. The amplitude reduces gradually with the radial distance.

4.7 Acoustic Field Results

For the acoustic solution, the computational domain is 65×40 jet radii starting from x=5 axial location. The grid has 131×89 points. It has uniform distribution in x-direction with $\Delta x=0.5$. In r-direction, the grid is clustered inside the shear layer and is stretched away from it, until it becomes uniform with $\Delta r=\Delta x$. For $St=0.2$ (based on jet diameter), the nondimensional wavelength (λ) =10. Thus, the number of points per wavelength (PPW) in far field is 20 points, which is more than adequate for the DRP scheme. Also, the mean flow nature has to be considered to determine the mesh resolution. A fine mesh is required in high gradient regions to capture the mean flow variations correctly. Usually, this constraint is more restrictive than wave resolution requirement for jet noise computations in near field region. Figure 4.7 demonstrates the multi-block grid used for multiple scale time integration scheme. Approximately half of the domain is covered with uniform grid with the largest time integration step, Δt=0.047. With four levels of time steps, the computational time is dramatically reduced. The reduction is estimated to be as much as three-fourth of the original required time for single block grid.

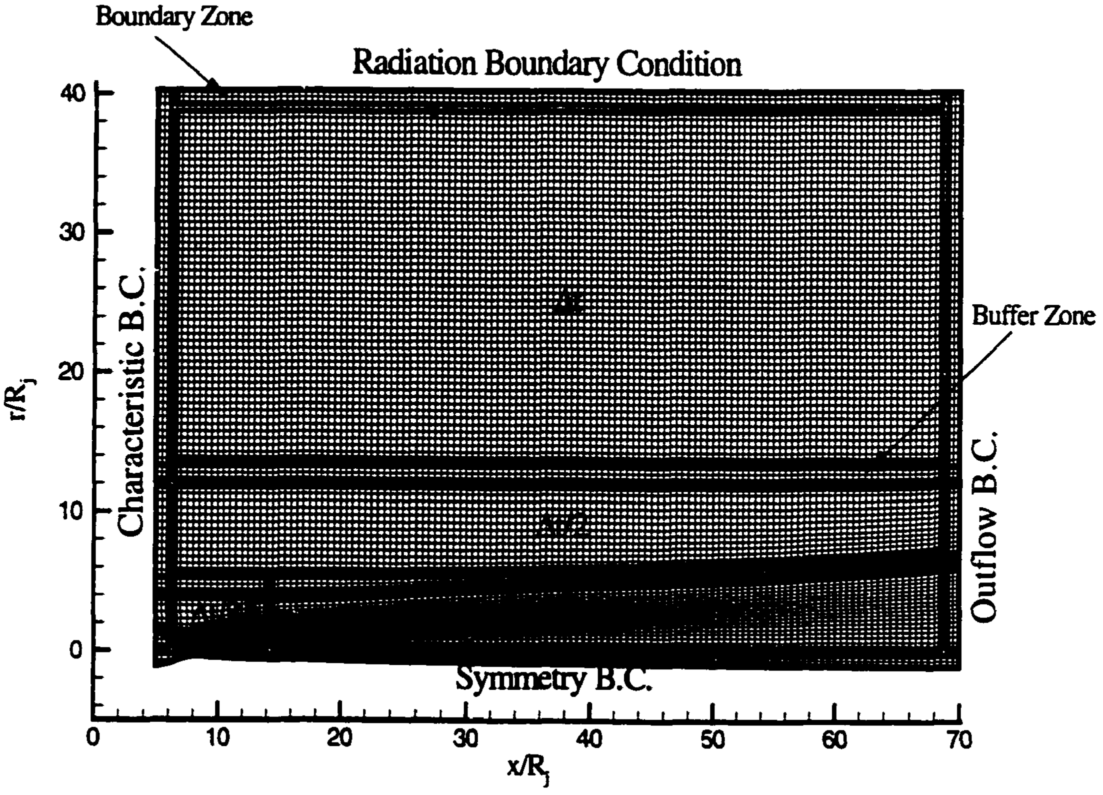
Boundary Zone
Radiation Boundary Condition
Buffer Zone
Characteristic B.C.
Outflow B.C.
Symmetry B.C.
Δt
Δt/2
r/R_j
40
30
20
10
0
x/R_j
0
10
20
30
40
50
60
70

Figure 4.7 Flow adapted multi-block grid for multiple time scales.

This grid is used for both axisymmetric (n=0) and helical mode (n=1) calculations. The eigen functions used to excite the jet are extracted from figure 4.6. The complex form of linearized Euler equation (equation 4.70) is solved with the appropriate mode number.

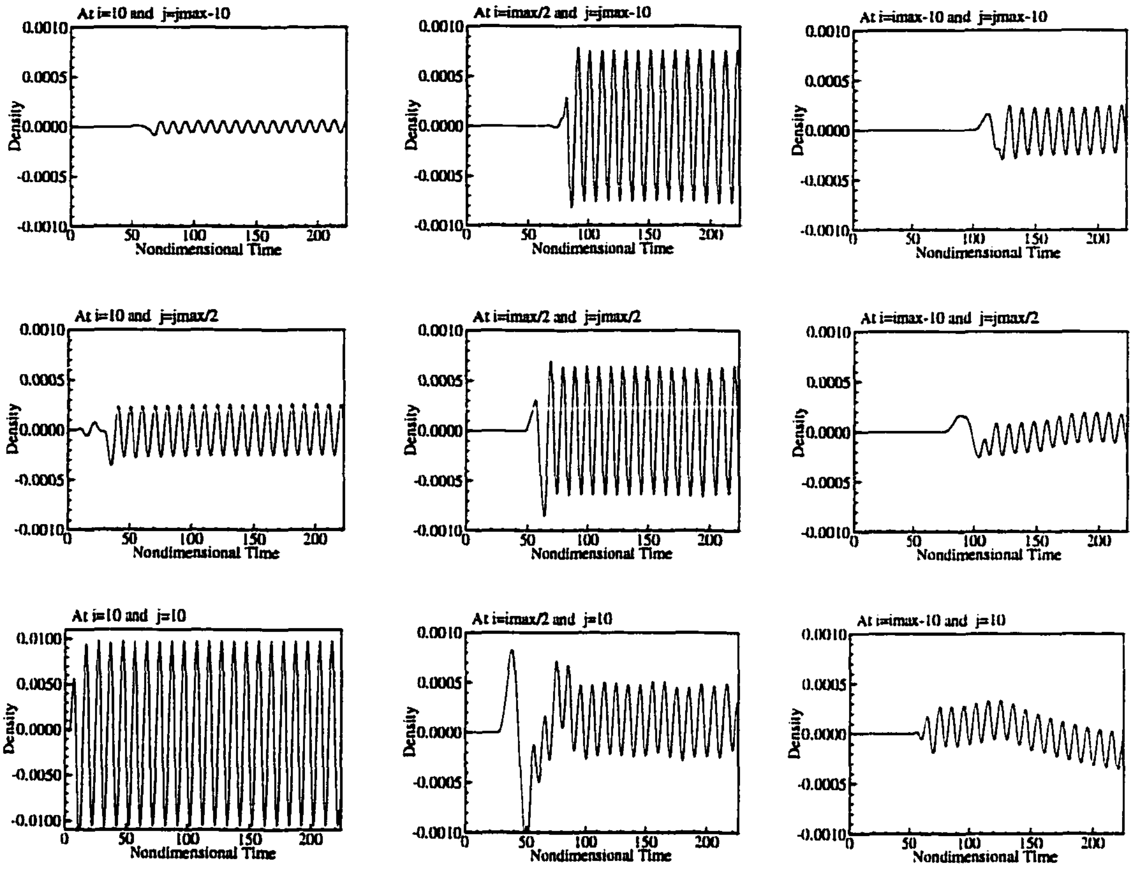

Figure 4.8 Time history of the density signal at nine monitoring points for the axisymmetric case.

To check the convergence of the solution, the time history of the density signal is tracked through nine monitoring points with (i, j) combinations: (10,10), (imax/2,10), (imax-10, 10), (10, jmax/2), (imax/2, jmax/2), (imax-10, jmax/2), (10, jmax-10), (imax/2, jmax-10), and (imax-10, jmax-10). These points represent a three-by-three test matrix to check the periodicity of the signal. For the axisymmetric case, the time history of these signals is shown in figure 4.8. At near field, the solution becomes periodic faster than at far field. This is true since the solution procedure is time-marching where the instability waves are introduced at the jet exit. The influence of these waves is felt earlier at near field point (10,10), (imax/2, 10), and (10, jmax/2). The figure shows the relative amplitude of the signal. The amplitude is small at the left and right portions of the domain. This suggests a directive character of the solution as will be discussed later.

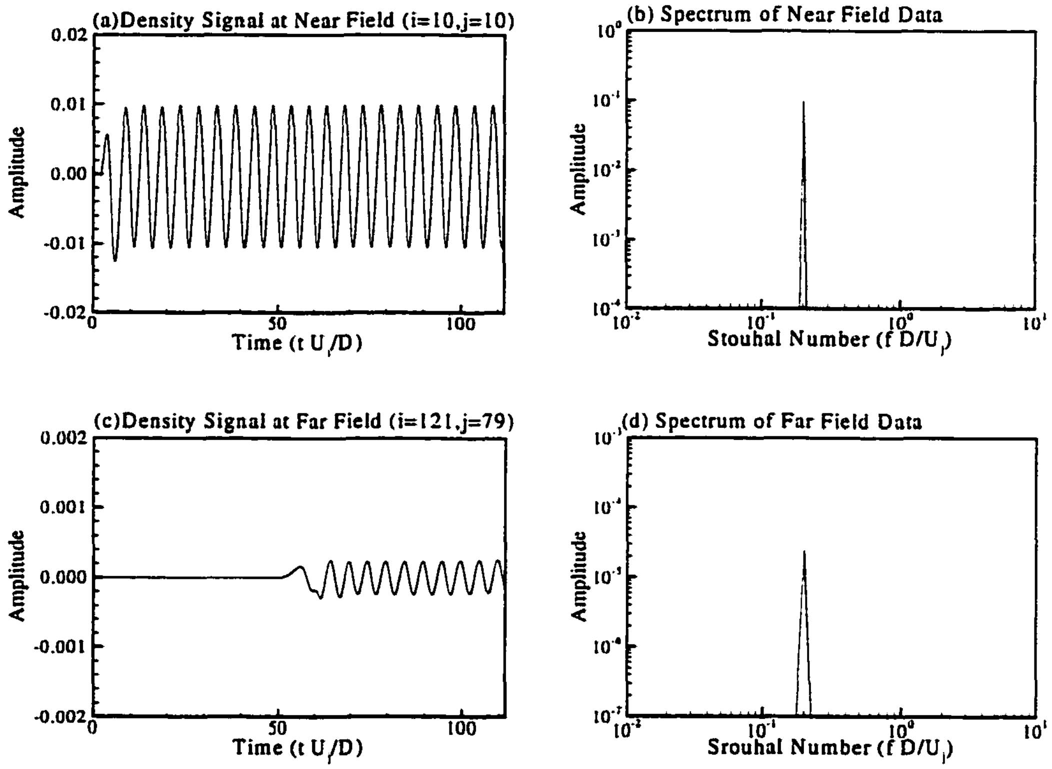

Figure 4.9 Density history and its spectra at two fixed field points for the axisymmetric case. (a)-(b) Near field. (c)-(d) Far field.

Figure 4.9 shows the time history of the density signal and the power spectral densities (PSD) at two points. The spectra are calculated by applying fast Fourier transforms to the time history data. Since the governing equations are linear and the excitation disturbance has single frequency, it is expected that only this frequency mode will appear in the spectra. If any other modes existed, they would have to be nonphysical and a result of numerical errors. Each PSD has a peak at the imposed frequency (the fundamental mode), followed by a sharp drop. All nonfundamental modes are at least two orders of magnitude lower than the imposed one. This indicated that the solution is practically free from spurious modes.

The acoustic solutions for the two mode calculations are presented in figures 4.10 and 4.11. The solution exhibits the wavy nature of the acoustic fields with little or no dispersion. There are hardly any reflections from the boundaries. No boundary buffers or sponge layers are required for the current boundary treatment, which meant no wasted computational domain. Note the oscillatory nature of the sound source in the near field region. The radiated sound peaks at an angle 43.65 degrees. The SPL contours resemble that of a quadrupole with preferred forward emission.

Presented in figure 4.12 are the comparisons of the computed sound-pressure-levels (SPL) with the experimental data of Trout and Mclaughlin (1982) and the asymptotic expansion results of Tam and Burton (1984b). Trout and Mclaughlin attempted to excite a 2.1 Mach jet with a single axisymmetric disturbance at $St=0.2$. However, other axisymmetric and three-dimensional modes were present, and the initial excitation level was not well defined. Because the governing equations are linear, the calculated results have an unknown multiplicative constant and the absolute pressure level can not be predicted. To compare with experimental results, the magnitude of this constant is tuned so that the calculated pressure level at a chosen field point, say at (34,20), matches the corresponding experimental value. Once this constant is determined, it is used to scale all the calculated data. The entire calculated data are moved about four jet diameters downstream as suggested by Tam and Burton (1984b). The results are in good qualitative agreement with the experiment. The lobed nature of the contours, the direction of the lobe and the spacing of the contours are correctly predicted. The direction of the peak sound radiation as defined by the lobe of the calculated contours and that of the measurements is practically the same. The percentage error in SPL peak location is presented in table 4.1. The helical mode agrees favorably with the experimental data, while the axisymmetric mode has larger errors.

Mode Type	SPL=150	SPL=148	SPL=146	SPL=144
Axisymmetric mode (n=0)	8%	6.4%	11%	16%
Helical mode (n=1)	2%	4.6%	1%	3.7%

Table 4.1 Percentage error in SPL peak location.

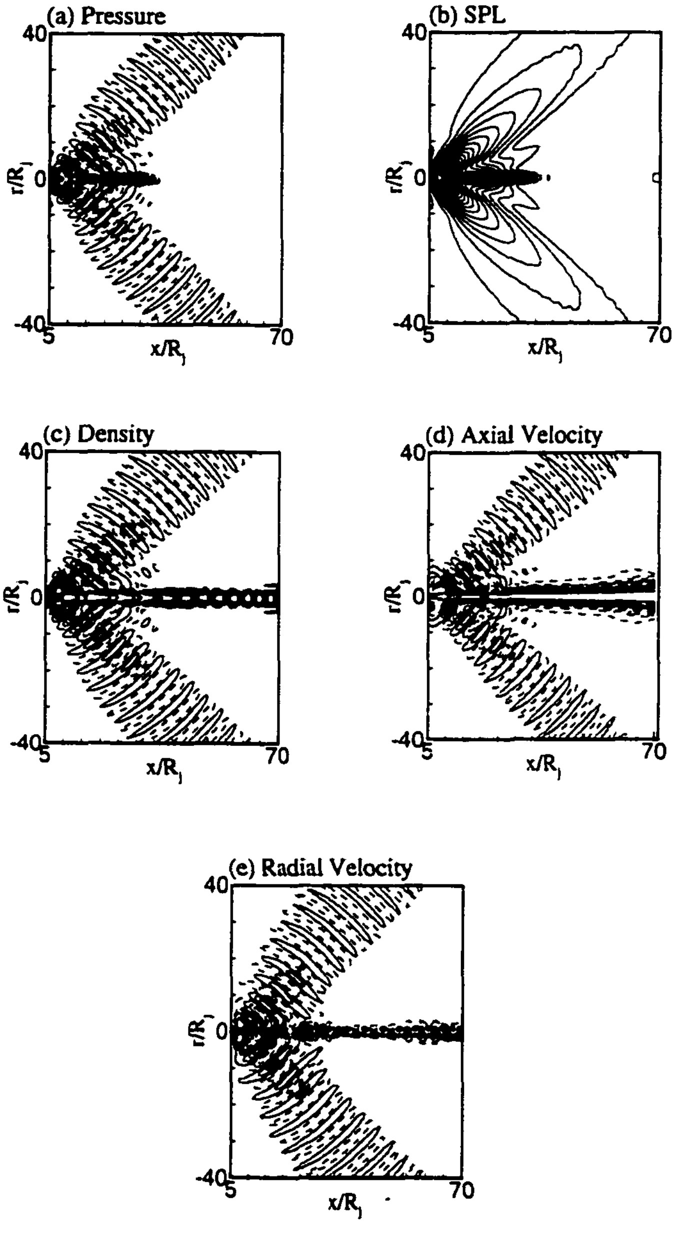

Figure 4.10 Simulation of axisymmetric instability generated jet noise. (a) Instantaneous pressure. (b) SPL. (c) Instantaneous density. (d) Instantaneous axial velocity. (e) Instantaneous radial velocity. (Dashed lines indicate negative values.)

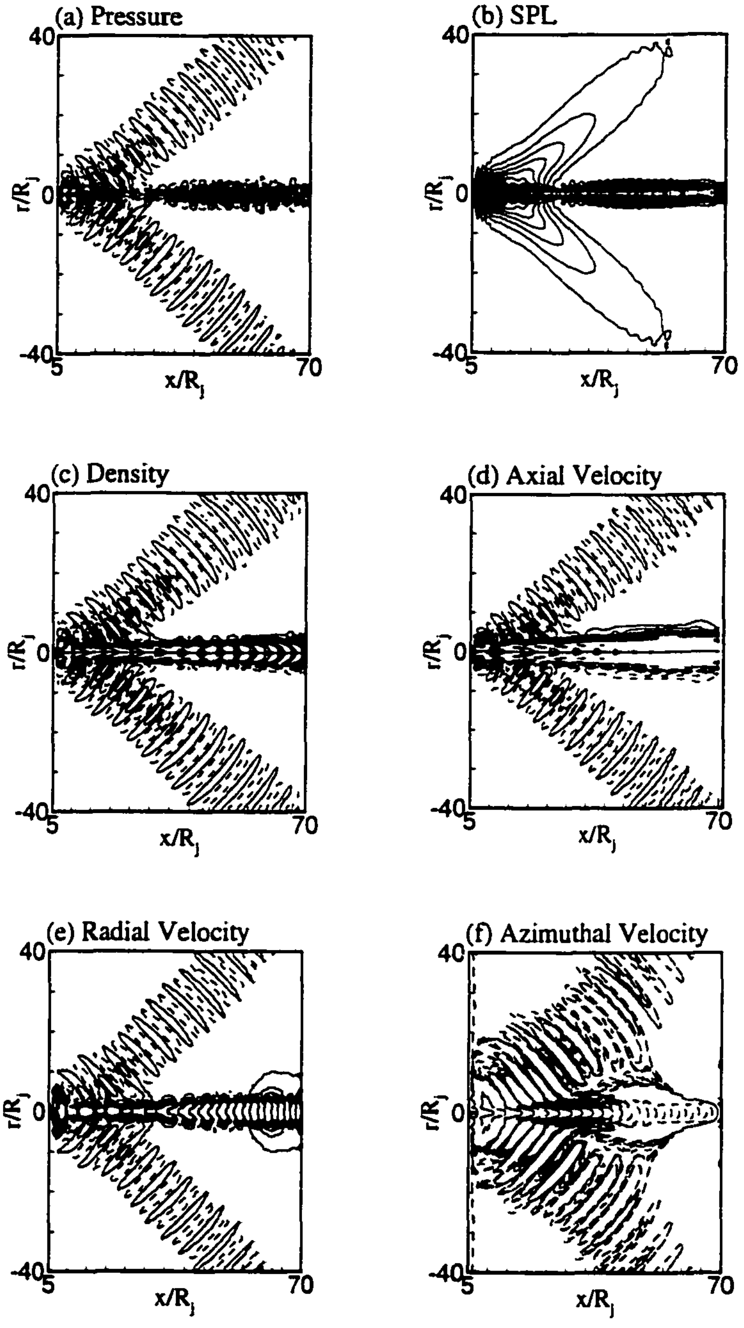

Figure 4.11 Simulation of helical instability generated jet noise. (a) Instantaneous pressure. (b) SPL. (c) Instantaneous density. (d) Instantaneous axial velocity. (e) Instantaneous radial velocity. (f) Instantaneous azimuthal velocity.

(Dashed lines indicate negative values.)

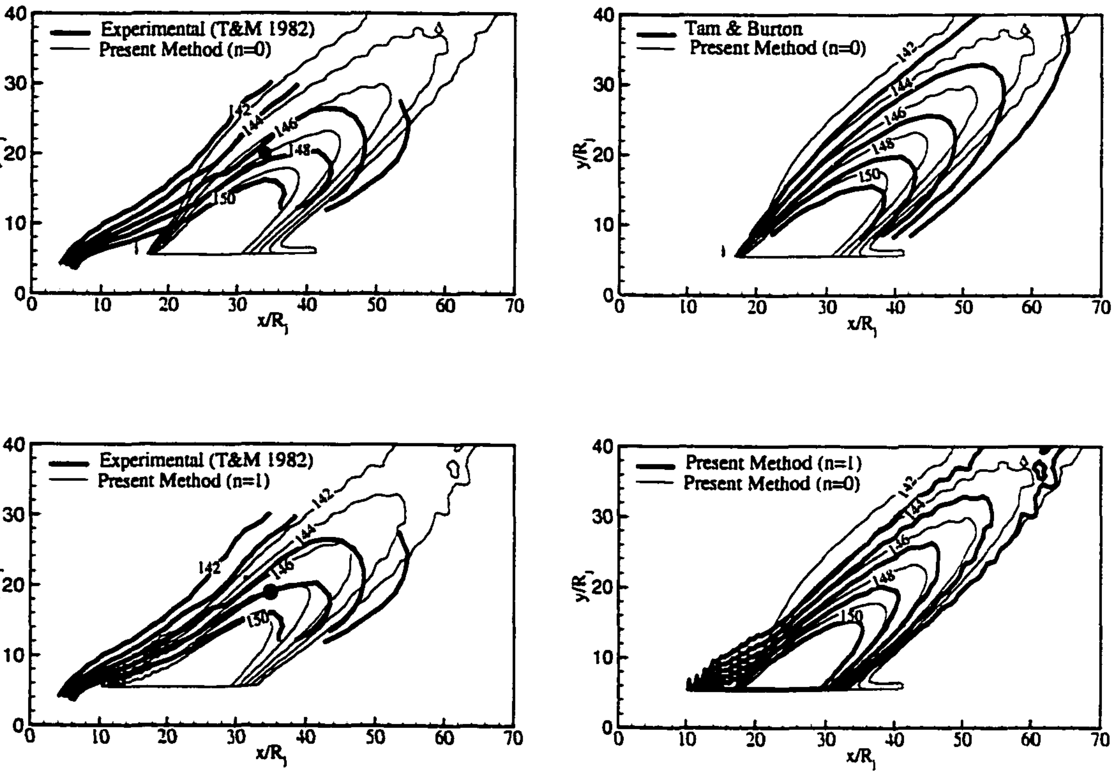

Figure 4.12 Comparison of sound-pressure-level contours. (a) Axisymmetric mode Vs. experimental data. (b) Axisymmetric mode Vs. Tam & Burton (1984b) results. (c) Helical mode Vs. experimental data. (d) Helical mode Vs. axisymmetric mode.

CHAPTER V

RAILWAY NOISE BARRIER

5.1 Introduction

The most commonly used passive mechanism for noise reduction in the neighborhood of highways, railways, airports, etc. is to build a wall or a barrier along the highway or around parts of the airport or the industrial building, respectively, in order to intercept the line-of-sight from the noise source to a receiver. Such barriers reduce the noise that is transmitted. However, some of the acoustic energy is diffracted over the barrier top and around its ends or scattered by other objects so that part of the noise is deflected to inhabited areas behind the barrier (refer to figure 5.1). The shadow zone is defined as the region where only diffracted sound exists. In the interference zone, incident waves are combined with the diffracted and/or reflected waves. Barriers can be constructed from natural materials, such as earth and wood, or from man-made materials, such as concrete, aluminum and fiber glass, and must shield against the predominant portion of the sound energy radiated from the source and directed toward the reception point. The effectiveness of such a barrier depends on its height, its shape, and whether it has sound absorbing coverage. Moreover, it is dependent on the type of the noise, i.e. its frequency content.

The finite difference method has several drawbacks for such problems. The grid generation procedure would have to cope with the complicated geometry of the barrier with steep corners, which is an extremely difficult task for structured grid codes. The grid orthogonality condition at the wall would be a difficult issue. Without this orthogonality condition, the wall boundary condition cannot be imposed. If frequency domain calculations are pursued, the grid size would have to be fine enough to capture the wave. Consequently, the computational time will increase significantly as the source frequency increases. Boundary element method eliminates those problems by simply requiring only surface discretization, i.e., no grid generation is required in the domain.

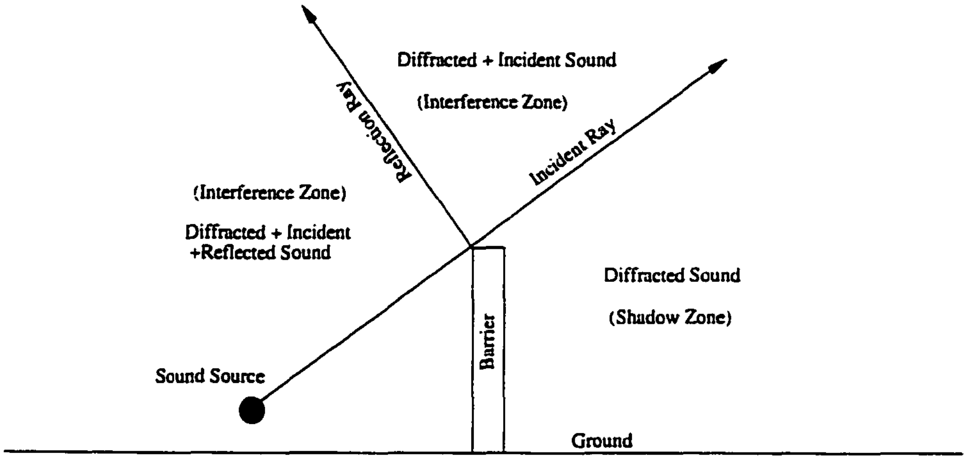
Diffracted + Incident Sound
(Interference Zone)
Reflection Ray
Incident Ray
(Interference Zone)
Diffracted + Incident +Reflected Sound
Diffracted Sound
(Shadow Zone)
Barrier
Sound Source
Ground

Figure 5.1 Acoustic zones around a barrier.

The noise sources of a railway system are discussed in section 5.2. The governing equation in frequency domain is introduced in section 5.3. Section 5.4 is devoted to the Boundary element method formulation. The sound source calculated from a typical noise spectrum of a train is presented in section 5.5. Barrier geometry and surface grids are demonstrated in section 5.6. The results of the zero-elevation case are introduced in section 5.7. Elevated deck simulations are presented in section 5.8. The results are compared with the experiment in section 5.9.

5.2 Railway Noise

For a rail system, the principal sources of noise are: (1) the interaction between wheels and rails, (2) the propulsion system of the railcars and locomotives, (3) auxiliary equipment, and (4) in the case of high-speed trains, aerodynamic noise. The noise sources are usually described in terms of A-weighted sound pressure levels (SPL_A) at a standard distance from the track and a standard height above the ground.

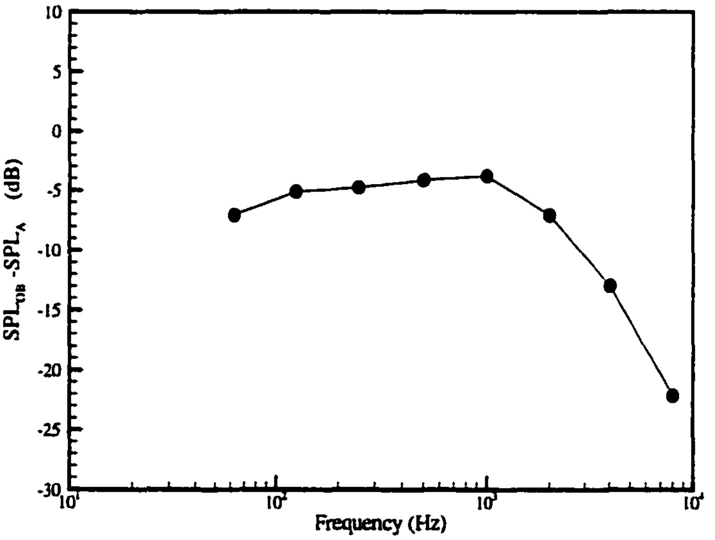

Figure 5.2 Average relative octave-band spectra for railcars and rubber-tired transit cars in the open electrically powered passenger railcars.

The dominant source of noise for railcars over most of their speed range is the interaction between the wheels and rails. For railcars traveling on a tangent straight track, the A-weighted sound level (at 100 ft from the track centerline and 5 ft above the ground) due to wheel/rail interaction can be obtained from the following formula (Hanson et al. 1994):

$$SPL_A = 75 + 30\log(V/V_0) \qquad dBA \tag{5.1}$$

where V is the railcar speed in mph and V_0 is a reference speed of 37 mph. A typical frequency spectrum of the sound source is shown in figure 5.2. This figure demonstrates the wide frequency range included in the noise source (62.5 Hz to 8000 Hz), which complicate the task of any computational method.

5.3 Governing Equation

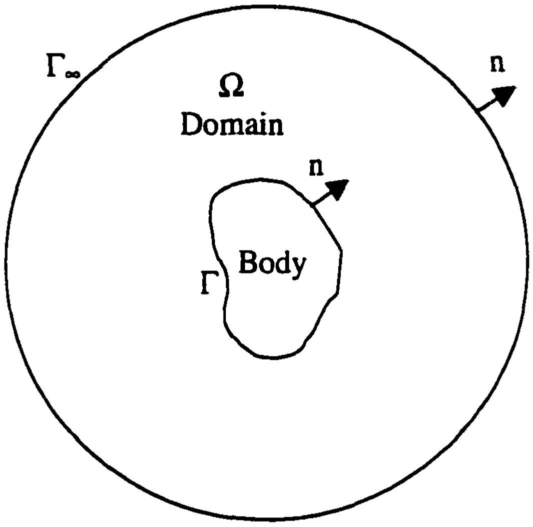

Figure 5.3 Acoustic domain.

A mathematical model for the propagation of small-amplitude acoustic waves through a homogeneous acoustic medium at rest is the linear wave equation,

$$\nabla^2 p(\mathbf{x},t) - \frac{1}{C^2}\frac{\partial^2 p(\mathbf{x},t)}{\partial t^2} = s(\mathbf{x},t) \qquad \text{for } \mathbf{x} \in \Omega, \quad t \geq 0 \tag{5.2}$$

The scalar function $p(\mathbf{x},t)$ is the excess acoustic pressure at a point $\mathbf{x}\equiv(x,y)$ at time t, C is the speed of sound and s is the sound source. Assuming homogeneous initial conditions, i.e., a quiescent past for the acoustic domain, the determination of the sound distribution in the region Ω (refer to figure 5.3), interior or exterior to the boundary surface Γ, means finding the unique solution of equation 5.1 which satisfy the boundary conditions,

(A) Surface B.C.:
$$\frac{\partial p(\mathbf{x},t)}{\partial n}=\bar{q}(\mathbf{x},t) \qquad \text{for} \quad \mathbf{x}\in\Gamma, \quad t\geq 0 \tag{5.3}$$

where n is the outward normal to the boundary, $\bar{q}=0$ for perfectly hard surface, and $\bar{q}\neq 0$ for radiation by the surface.

(B) Far field Sommerfeld Radiation B.C.:
$$\lim_{r\to\infty}[r\,(\frac{\partial p}{\partial r}+\frac{1}{C}\frac{\partial p}{\partial t})]=0 \qquad \text{for} \quad \mathbf{x}\in\Gamma_\infty \tag{5.4}$$

Assuming time dependence with the angular frequency ω,

$$p(x,y,t)=\mathrm{Re}(\hat{p}(x,y)e^{-i\omega t}), \quad s(x,y,t)=\mathrm{Re}(\hat{s}(x,y)e^{-i\omega t}) \tag{5.5}$$

Equation 5.2 becomes the Helmholtz equation,

$$\nabla^2\hat{p}+k^2\hat{p}=\hat{s} \tag{5.6}$$

where $k=\omega/C$ is the acoustic wave number. The boundary conditions are

Surface B.C.:
$$\frac{\partial\hat{p}(\mathbf{x})}{\partial n}=\bar{q}(\mathbf{x}) \qquad \text{for} \quad \mathbf{x}\in\Gamma, \quad t\geq 0 \tag{5.7}$$

Far field Sommerfeld Radiation B.C.:
$$\lim_{r\to\infty}[r\,(\frac{\partial\hat{p}}{\partial r}-ik\hat{p}(\mathbf{x})]=0 \qquad \text{for} \quad \mathbf{x}\in\Gamma_\infty \tag{5.8}$$

5.4 Boundary Element Method

5.4.1 Formulation

The boundary integral equation required by the method can be deduced in a simple way based on the weighted residual method. An approximate solution $\hat{p}$ is assumed and, hence, the governing equation and the boundary conditions are not satisfied exactly, i.e.,

$$\text{Residual}: \quad R = \nabla^2 \hat{p}(\mathbf{x}) + k^2 \hat{p}(\mathbf{x}) - \hat{s}(\mathbf{x}) \neq 0 \qquad \text{for} \quad \mathbf{x} \in \Omega$$

$$R_1 = \frac{\partial \hat{p}(\mathbf{x})}{\partial n} - \bar{q}(\mathbf{x}) \neq 0 \qquad \text{for} \quad \mathbf{x} \in \Gamma$$

$$R_2 = \frac{\partial \hat{p}(\mathbf{x})}{\partial n} - ik\hat{p} \neq 0 \qquad \text{for} \quad \mathbf{x} \in \Gamma_\infty$$

The above residuals are forced to be zero in an average sense by the weighted residual formula,

$$\int_\Omega \underbrace{(\nabla^2 \hat{p} + k^2 \hat{p} - \hat{s})}_{P.D.E.\ \text{Residual}} \hat{p}^* d\Omega = \int_{\Gamma_\infty} \underbrace{(\frac{\partial \hat{p}}{\partial n} - ik\hat{p})}_{Sommerfield\ R.B.C.\ \text{Residual}} \hat{p}^* d\Gamma - \int_\Gamma \underbrace{(\frac{\partial \hat{p}}{\partial n} - \bar{q})}_{Surface\ B.C.\ \text{Residual}} \hat{p}^* d\Gamma \qquad (5.9)$$

where $\hat{p}^*$ is a fundamental solution of the original P.D.E., i.e,

$$\nabla^2 \hat{p}^* + k^2 \hat{p}^* = -\Delta_i \qquad (5.10)$$

where Δ_i is the Dirac delta function. The fundamental solution used here is,

$$\hat{p}^* = \frac{i}{4} H_0^1(kr) = \frac{i}{4}(J_0(kr) + iY_0(kr)) \qquad (5.11)$$

$$\frac{\partial \hat{p}^*}{\partial n} = -\frac{ik}{4} H_1^1 \frac{\partial r}{\partial n} = -\frac{ik}{4}(J_1(kr) + iY_1(kr)) \left(\frac{\partial r}{\partial x} n_x + \frac{\partial r}{\partial y} n_y\right) \qquad (5.12)$$

where

$r = |\mathbf{x} - \mathbf{x}_i|$ **x** is a field point and $\mathbf{x}_i$ is the source point,

H_n^1 is the n-order Hankel function of the first kind,

J_n and Y_n are the n-order Bessel functions of the first and second kind, respectively.

This solution represents the field generated by a concentrated unit source acting at point "i".

Integrating the Laplacian term twice yields,

$$\begin{aligned}
\int_\Omega (\nabla^2 \hat{p})\hat{p}^* d\Omega &= \int_\Omega \nabla\cdot(\nabla\hat{p}\ \hat{p}^*)d\Omega - \int_\Omega \nabla\hat{p}\cdot\nabla\hat{p}^* d\Omega \\
&= \int_{\Gamma_\infty} \hat{p}^*\ \nabla\hat{p}\cdot d\bar{\Gamma}_\infty - \int_\Gamma \hat{p}^*\ \nabla\hat{p}\cdot d\bar{\Gamma} - \int_\Omega \nabla\hat{p}\cdot\nabla\hat{p}^* d\Omega \\
&= \int_{\Gamma_\infty} \hat{p}^*\ \nabla\hat{p}\cdot d\bar{\Gamma}_\infty - \int_\Gamma \hat{p}^*\ \nabla\hat{p}\cdot d\bar{\Gamma} - \int_{\Gamma_\infty} \hat{p}\,\nabla\hat{p}^*\cdot d\bar{\Gamma}_\infty \\
&\qquad + \int_\Gamma \hat{p}\,\nabla\hat{p}^*\cdot d\bar{\Gamma} + \int_\Omega \hat{p}\,(\nabla^2\hat{p}^*)d\Omega \\
&= \int_{\Gamma_\infty} (\nabla\hat{p}\ \hat{p}^* - \hat{p}\,\nabla\hat{p}^*)\cdot d\bar{\Gamma}_\infty - \int_\Gamma (\nabla\hat{p}\ \hat{p}^* - \hat{p}\,\nabla\hat{p}^*)\cdot d\bar{\Gamma} + \int_\Omega \hat{p}\,(\nabla^2\hat{p}^*)d\Omega
\end{aligned}$$

where

$$d\bar{\Gamma}_\infty = \vec{n}\,d\Gamma_\infty \quad \text{and} \quad d\bar{\Gamma} = -\vec{n}\,d\Gamma \qquad \text{(refer to figure 5.1)}$$

Hence,

$$\int_\Omega (\nabla^2\hat{p})\hat{p}^* d\Omega = \int_{\Gamma_\infty} \left(\frac{\partial\hat{p}}{\partial n}\hat{p}^* - \hat{p}\frac{\partial\hat{p}^*}{\partial n}\right)d\Gamma_\infty + \int_\Gamma \left(\frac{\partial\hat{p}}{\partial n}\hat{p}^* - \hat{p}\frac{\partial\hat{p}^*}{\partial n}\right)d\Gamma + \int_\Omega \hat{p}\,(\nabla^2\hat{p}^*)d\Omega$$

Substitute in equation 5.9, and rearrange terms

$$\begin{aligned}
\int_\Omega (\nabla^2\hat{p}^* + k^2\hat{p}^*)\hat{p}\,d\Omega &= \int_{\Gamma_\infty} \hat{p} \overbrace{\left(\frac{\partial\hat{p}^*}{\partial n} - ik\hat{p}^*\right)}^{\substack{\text{since } p^* \text{ satisfiies Sommerfield B.C} \\ =0}} d\Gamma_\infty - \int_\Gamma \left(\frac{\partial\hat{p}}{\partial n}\hat{p}^* - \hat{p}\frac{\partial\hat{p}^*}{\partial n}\right)d\Gamma \\
&\qquad + \int_\Omega \hat{s}\,\hat{p}^* d\Omega
\end{aligned}$$

Hence,

$$\int_{\Omega}(\nabla^2\hat{p}^* + k^2\hat{p}^*)\hat{p}\,d\Omega = -\int_{\Gamma}\left(\frac{\partial\hat{p}}{\partial n}\hat{p}^* - \hat{p}\frac{\partial\hat{p}^*}{\partial n}\right)d\Gamma + \int_{\Omega}\hat{s}\,\hat{p}^*d\Omega$$

Using equation 5.9,

$$\int_{\Omega}(\nabla^2\hat{p}^* + k^2\hat{p}^*)\hat{p}d\Omega = \int_{\Omega}(-\Delta_i)\hat{p}d\Omega = -c_i\hat{p}_i$$

where

$$\begin{aligned} c_i &= 1 & x_i &\in \Omega \\ &= (1-\tfrac{\theta_i}{2\pi}) & x_i &\in \Gamma \end{aligned} \tag{5.13}$$

where θ_i is the corner angle at point "*i*"

Thus,

$$c_i\hat{p}_i = \int_{\Gamma}\left(\frac{\partial\hat{p}}{\partial n}\hat{p}^* - \hat{p}\frac{\partial\hat{p}^*}{\partial n}\right)d\Gamma - \int_{\Omega}\hat{s}\,\hat{p}^*d\Omega \tag{5.14}$$

Assume the source function in the form

$$\hat{s} = \sum_{l=1}^{L} \underbrace{g_l(k)}_{source\ strength}\ \delta(\mathbf{x} - \underbrace{\mathbf{x}_l}_{source\ location}) \tag{5.15}$$

Hence,

$$F_i = -\int_{\Omega}\hat{s}\,\hat{p}^*(k\,|\mathbf{x}-\mathbf{x}_i|)d\Omega = -\sum_{l=1}^{L} g_l(k)\ \hat{p}^*(k\,|\mathbf{x}_l - \mathbf{x}_i|) \tag{5.16}$$

Finally,

$$c_i\hat{p}_i = \int_{\Gamma}(\overline{q}\,\hat{p}^*(k\,|\mathbf{x}-\mathbf{x}_i|) - \hat{p}\,q^*(k\,|\mathbf{x}-\mathbf{x}_i|))d\Gamma + F_i \tag{5.17}$$

It should be noted that equation 5.17 applies for the case of a concentrated source at '*i*' and, consequently, the values of $\hat{p}$ and q^* are those corresponding to that particular position of source. For each other $\mathbf{x}_i$ position one will obtain a new integral equation.

5.4.2 Computational Method

To obtain an accurate discrete matrix representation of the boundary integral equation (equation 5.17), there are essentially three approximation problems: (i) the approximation of the geometry of the boundary surface Γ, (ii) the representation of the unknown boundary function $\hat{p}$, (iii) the treatment of the integrals that arise. Notice that it is assumed throughout that the fundamental solution is applied at a particular node '*i*', although this is not explicitly indicated in the $\hat{p}^*$ and q^* notation to avoid proliferation of indices.

5.4.2.1 Surface Approximation

If the boundary is divided into "*N*" segments or elements as shown in figure 5.4, equation 5.15 can be discretized for a given point '*i*' as follows

$$c_i \hat{p}_i = \sum_{j=1}^{N} \left(\int_{\Gamma_j} (\bar{q}\hat{p}^* - \hat{p}\, q^*) d\Gamma_j \right) + F \tag{5.18}$$

The point '*i*' is one of the boundary nodes. Γ_j is element *j* of the boundary. In this equation, there are two basic integrals to be carried out over the elements, i.e. those of the following types,

$$I_1 = \int_{\Gamma_j} \hat{p}\, q^* d\Gamma_j \quad ,and \quad I_2 = \int_{\Gamma_j} \bar{q}\, \hat{p}^* d\Gamma_j \tag{5.19}$$

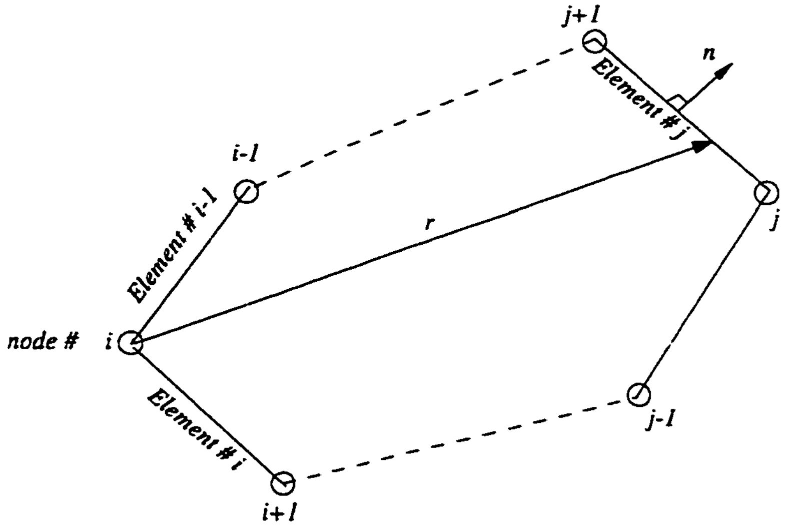
j+1
n
Element # j
i-1
Element # i-1
r
j
node # i
Element # i
j-1
i+1

Figure 5.4 Surface discretization.

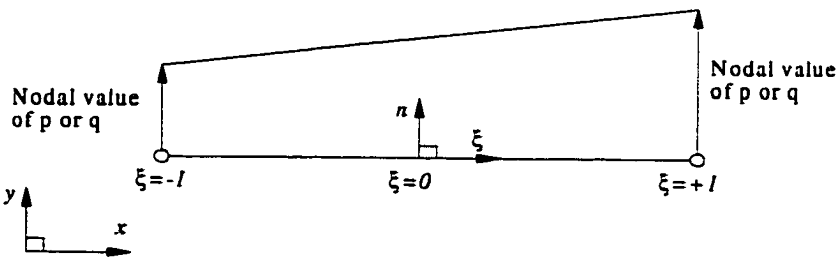
Nodal value of p or q
Nodal value of p or q
n
ξ
ξ=-1
ξ=0
ξ=+1
y
x

Figure 5.5 Linear element definitions.

Γ_j is assumed to be linear elements (see figure 5.5) as follows,

$$x = \phi_1 x_1 + \phi_2 x_2, \quad y = \phi_1 y_1 + \phi_2 y_2 \tag{5.20}$$

where

(x_1, y_1) and (x_2, y_2) are the end points or nodes of element j,

$\phi_1 = \frac{1}{2}(1-\xi)$ and $\phi_2 = \frac{1}{2}(1+\xi)$ are the linear shape functions,

ξ is the element *natural* coordinate [-1,1]

5.4.2.2 Solution Approximation

For linear elements, a linear variation of $\hat{p}$ and q is assumed along the element,

$$\hat{p} = \phi_1 \hat{p}_1 + \phi_2 \hat{p}_2, \text{and} \quad q = \phi_1 q_1 + \phi_2 q_2 \tag{5.21}$$

where $\phi_1 = \frac{1}{2}(1-\xi), \quad \phi_2 = \frac{1}{2}(1+\xi)$

5.4.2.3 Evaluation of Integrals

The integrals defined in equation 5.17 represent the effect of the node '*i*' where the fundamental solution is acting on any other node *j*. Hence, their resulting values are sometimes called influence coefficients. For linear elements, these integrals are evaluated as follows,

$$\begin{aligned} I_1 &= \int_{\Gamma_j} \lfloor \phi_1 \quad \phi_2 \rfloor \begin{pmatrix} \hat{p}_1 \\ \hat{p}_2 \end{pmatrix} q^* d\Gamma_j = \left\lfloor \int_{\Gamma_j} \phi_1 q^* d\Gamma_j \quad \int_{\Gamma_j} \phi_2 q^* d\Gamma_j \right\rfloor \begin{pmatrix} \hat{p}_1 \\ \hat{p}_2 \end{pmatrix} \\ &= \lfloor h_{ij}^1 \quad h_{ij}^2 \rfloor \begin{pmatrix} \hat{p}_1 \\ \hat{p}_2 \end{pmatrix}_j \end{aligned} \tag{5.22}$$

where

$$h_{ij}^1 = \int_{\Gamma_j} \phi_1 q^* d\Gamma_j, \quad h_{ij}^2 = \int_{\Gamma_j} \phi_2 q^* d\Gamma_j \tag{5.23}$$

Similarly,

$$I_2 = \lfloor g^1_{ij} \quad g^2_{ij} \rfloor \begin{Bmatrix} q_1 \\ q_2 \end{Bmatrix}$$

where

$$g^1_{ij} = \int_{\Gamma_j} \phi_1 \hat{p}^* d\Gamma_j, \quad g^2_{ij} = \int_{\Gamma_j} \phi_2 \hat{p}^* d\Gamma_j \tag{5.24}$$

Equation 5.15 becomes,

$$c_i p_i + \sum_{j=1}^{N} \lfloor h^1_{ij} \quad h^2_{ij} \rfloor \begin{Bmatrix} \hat{p}_1 \\ \hat{p}_2 \end{Bmatrix}_{along \ elemnt \ j} = \sum_{j=1}^{N} \lfloor g^1_{ij} \quad g^2_{ij} \rfloor \begin{Bmatrix} q_1 \\ q_2 \end{Bmatrix}_{along \ elemnt \ j} + F_i \tag{5.25}$$

Using continuity condition for both $\hat{p}$ and $\partial \hat{p} / \partial n$, this equation becomes,

$$c_i \hat{p}_i + \sum_{j=1}^{N} \bar{h}_{ij} \hat{p}_j = \sum_{j=1}^{N} \bar{g}_{ij} + F_i \tag{5.26}$$

where

$$\bar{h}_{ij} = h^1_{ij} + h^2_{i,j-1}, \quad \bar{g}_{ij} = g^1_{ij} + g^2_{i,j-1} \tag{5.27}$$

Or, in matrix form,

$$[\mathbf{H}]\{\hat{\mathbf{p}}\} = [\mathbf{G}]\{\mathbf{q}\} + \{\mathbf{F}\} \tag{5.28}$$

where

$$H_{ij} = c_i \delta_{ij} + \bar{h}_{ij} \quad , \quad G_{ij} = \bar{g}_{ij} \tag{5.29}$$

where δ_{ij} is the Kronecker delta.

In order to evaluate $h^1_{ij}, h^2_{i,j}, g^1_{ij}$, and $g^2_{i,j}$, a change of coordinates can be performed from (x,y) to the element natural coordinate system (ξ, n). The Jacobian of the transformation J is calculated as follows:

$$\frac{d\Gamma^2}{d\xi^2}=\frac{dx^2}{d\xi^2}+\frac{dy^2}{d\xi^2}$$

$$d\Gamma=\sqrt{(\frac{dx}{d\xi})^2+(\frac{dy}{d\xi})^2}\ d\xi$$

$$d\Gamma=\tfrac{1}{2}\sqrt{(x_2-x_1)^2+(y_2-y_1)^2}\ d\xi=J\ d\xi \tag{5.30}$$

Hence,

$$\int_{\Gamma_j} f(x,y)\, d\Gamma=\int_{-1}^{1} f(\xi)\ J\ d\xi \tag{5.31}$$

In this way, the above expressions can be calculated using numerical integration formulae (such as Gauss quadrature rules) for the case *i≠j*. In the case where *i* and *j* are on the same element (i.e. *i=j*), the presence on that element of the singularity due to the fundamental solution requires a more accurate integration. For these integrals it is recommended to use higher-order integration rules or a special formula that cancels the singularity. If a hard wall is considered, i.e. $\bar{q}=0$ along the surface, I_2 is always zero (no need to calculate g_{ij}^1 or g_{ij}^2). So, only $h_{ij}^1, h_{i,j}^2$ are needed:

$$h_{ij}^1=\int_{-1}^{1}-\frac{1}{2}(1-\xi)\frac{ik}{4}H_1^1(kr)\,(\frac{\partial r}{\partial x}n_x+\frac{\partial r}{\partial x}n_y)\,J\,d\xi \tag{5.32}$$

where

$r=\sqrt{(x-x_i)^2+(y-y_i)^2}$,

$\frac{\partial r}{\partial x}=\frac{(x-x_i)}{r}$, and $\frac{\partial r}{\partial y}=\frac{(y-y_i)}{r}$,

$x=\frac{1}{2}(1-\xi)x_1+\frac{1}{2}(1+\xi)x_2$, and $y=\frac{1}{2}(1-\xi)\,y_1+\frac{1}{2}(1+\xi)\,y_2$,

$$n_x = -\frac{y_2 - y_1}{\sqrt{(x_2 - x_1)^2 + (y_2 - y_1)^2}} \text{ , and } \quad n_y = \frac{x_2 - x_1}{\sqrt{(x_2 - x_1)^2 + (y_2 - y_1)^2}},$$

(x_1, y_1) and (x_2, y_2) are the end points (nodes) of element *j*.

Similar expressions can be deduced for $h^2_{i,j}$. It is noted here that since $H^1_1(kr)$ is singular at r=0, a problem occurs when point '*i*' is a node of the element '*j*', i.e., for the integral over element '*i*' and '*i-1*' (refer to figure 5.4). To address this singularity problem, consider the expansion of the first-order Hankel function of first kind, $H^1_1(kr) = -i\frac{1}{\pi}(2/kr) + \cdots$. As r→0, $H^1_1(kr)$ behaves as 1/*r*-function. Since the integrand in (5.32) has $\vec{r}.\vec{n}$ term, which behaves as linear *r*-function as *r*→0, this term cancels the singularity at *r*=0 and hence $h^1_{ii} = h^2_{ii} = 0$ and $h^1_{i,i-1} = h^2_{i,i-1} = 0$ since $\vec{r}.\vec{n} = 0$ for elements '*i*' and '*i-1*' (refer to figure 5.4). If g^1_{ij} and g^2_{ij} were to be calculated, a higher-order shape function or special formula should be used to cancel the singularity.

5.5 Noise Source Modeling

From the train noise spectrum shown in figure 5.2, the source term on the right hand side of equation 5.6 can be deduced. The idea is to consider the total acoustic pressure as a linear summation of the pressures produced by the octave frequency sources:

$$p(t) = \sum_{m=1}^{M} p_m(t) = \sum_{m=1}^{M} A_m \cos(\omega_m t + \phi_m) \tag{5.33}$$

Defining the average squared pressure as,

$$\overline{p}^2 = \lim_{T\to\infty} \frac{1}{T} \int_{\tau}^{\tau+T} p^2(t)dt \tag{5.34}$$

For large *T*, the total average squared pressure is,

$$\overline{p}^2 = \sum_{m=1}^{M} \overline{p}_m^2 = \sum_{m=1}^{M} \frac{A_m^2}{2} \tag{5.35}$$

Using the definition of the sound pressure level,

$$SPL_m = 10 \log(\overline{p}_m^2 / p_{ref}^2) \tag{5.36}$$

The average squared pressure components $\overline{p}_m^2$ can be obtained from noise spectrum. Assuming that the source amplitude is proportional to acoustic pressure, i.e. $\hat{s}_m \propto A_m$, the following relation is obtained:

$$\hat{s}_1 : \hat{s}_2 : \hat{s}_3 : \cdots : \hat{s}_M = \sqrt{\overline{p}_1^2} : \sqrt{\overline{p}_2^2} : \sqrt{\overline{p}_3^2} : \cdots : \sqrt{\overline{p}_M^2} \tag{5.37}$$

In this way, the ratio of the components of the sound source is known. Still one constant remains to be determined from scaling to match the absolute SPL_A calculated from equation 5.1. The final form of the source term is,

$$\hat{s} = a \sum_{m=1}^{M} \hat{s}_m \tag{5.38}$$

where $\hat{s}_m$ is the source strength at octave frequency f_m, and a is a scaling factor determined by the absolute value of SPL_A at given point. The train velocity is assumed to be 60 mph. Summarized in table 5.1 are the results of source strength calculations.

Frequency (Hz)	SPL_{OB}-SPL_A	SPL_{OB}	$\hat{s}_m / \hat{s}_1$
62.5	-7.049	74.249	1.000
125	-5.082	76.216	1.254
250	-4.754	76.544	1.302
500	-4.098	77.200	1.404
1000	-3.770	77.528	1.459
2000	-7.049	74.249	1.000
4000	-12.951	68.348	0.507

Table 5.1 Train noise source parameters.

5.6 Geometry and Grid

The numerical modeling uses linear approximation functions and elements of varying length. The number and the length of elements depend on the wavelength of the sound. A smooth change in element lengths is highly recommended to avoid kinks in the numerical solution. To represent a wave, a minimum of 3 elements per wavelength is needed. Since a low-order shape function is used, this number should be increased. The ground is represented in the model by considering the images of the source and the barrier, symmetric with respect to the plane of the ground.

In this study, both zero-elevation and elevated straight single track trains are considered. The term elevated means tracks are mounted on an elevated guideways. Figure 5.6 shows the geometry of the barrier and the deck. For track-on-ground case (zero-elevation), the source is located 54″ away from the barrier and 12.27″ above ground. The calibration point is 100 ft away from the center of track and 5 ft above ground. The sound level at that point is 81.3 dBA (using equation 5.1). For a train on an elevated track, the wayside A-weighted sound levels can be as much as 20 dBA greater than corresponding levels when the train runs on track at grade. This is primarily because of the radiation of sound from the vibration components of the elevated structure. For a concrete deck, a 3 dBA increase is assumed for the sound level. The calibration point is 100 ft away from the elevated structure and at the rail height. The sound level at that point is 84.3 dBA (adding 3 dBA to equation 5.1 output). The following reference parameters are used for non-dimensionalization: maximum barrier width (7.875″) for length, free stream speed of sound, (C_∞ =1140 ft/s) for velocity, and free stream density

(ρ_∞=1.225 kg/m^3) for density. Using these scales, the non-dimensional frequencies are 0.036, 0.072, 0.144, 0.288, 0.576, 1.151, and 2.303.

Surface and domain discretizations are demonstrated in figure 5.7. To enhance the efficiency of the computation, the surface grid is changed so that only a sufficient number of nodes is utilized for each frequency. This achieved a substantial reduction in the computer run times, since the covered frequency range is very wide (62.5 Hz to 4000 Hz) and the computational demands in terms of the number of surface nodes are very sparse. On the other hand, the domain grid is kept fixed for all frequencies to avoid interpolations. It should be noted that the smoothness of the change in element lengths is an important parameter to determine surface grid resolution. This is achieved using elements of varying length along each surface segment to match the element lengths in the adjacent surface segments.

A grid refinement study is conducted to determine the required number of surface grid points for each frequency. Figure 5.8 shows the results of this study for on-ground configuration at f=125 Hz. For this case, 48 points per wavelength are required (128 total grid points). One reason for this high PPW is the low-order approximation functions used (linear functions). Another reason is the smoothness requirement of the change in element length. The existence of a small corner in the right side of the barrier (refer to figure 5.7) makes a restriction on the grid resolution in the neighboring segments. Table 5.2 presents the results of the grid refinement study for on-ground configuration.

(a) Straight Single Track at Zero-Elevation

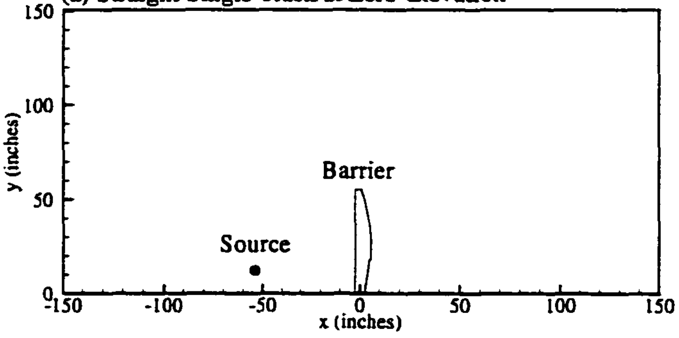
150
100
50
0
y (inches)
Barrier
Source
-150
-100
-50
0
50
100
150
x (inches)

(b) Straight Single Track on Elevated Deck (No Barrier)

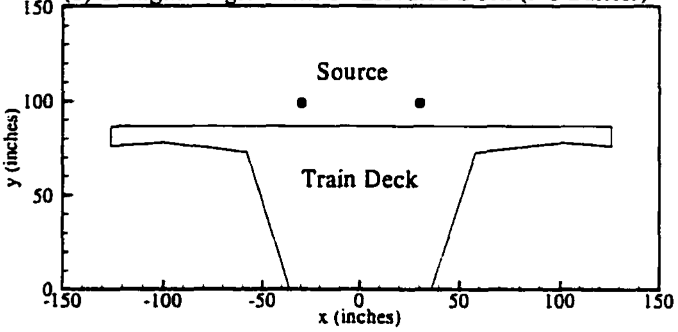
150
100
50
0
y (inches)
Source
Train Deck
-150
-100
-50
0
50
100
150
x (inches)

(c) Straight Single Track on Elevated Deck (with Barrier)

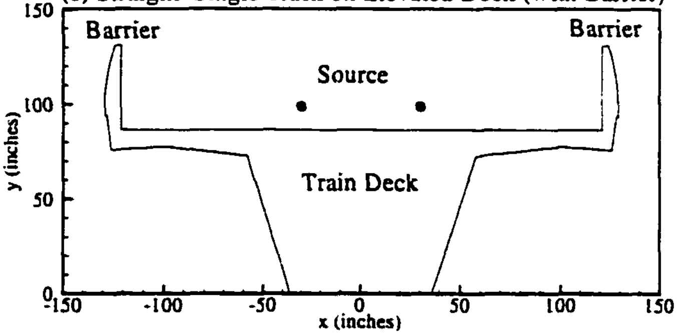
150
100
50
0
y (inches)
Barrier
Barrier
Source
Train Deck
-150
-100
-50
0
50
100
150
x (inches)

Figure 5.6 Geometry of barrier and train deck. (a) Track-on-ground case, (b) & (c) Elevated track.

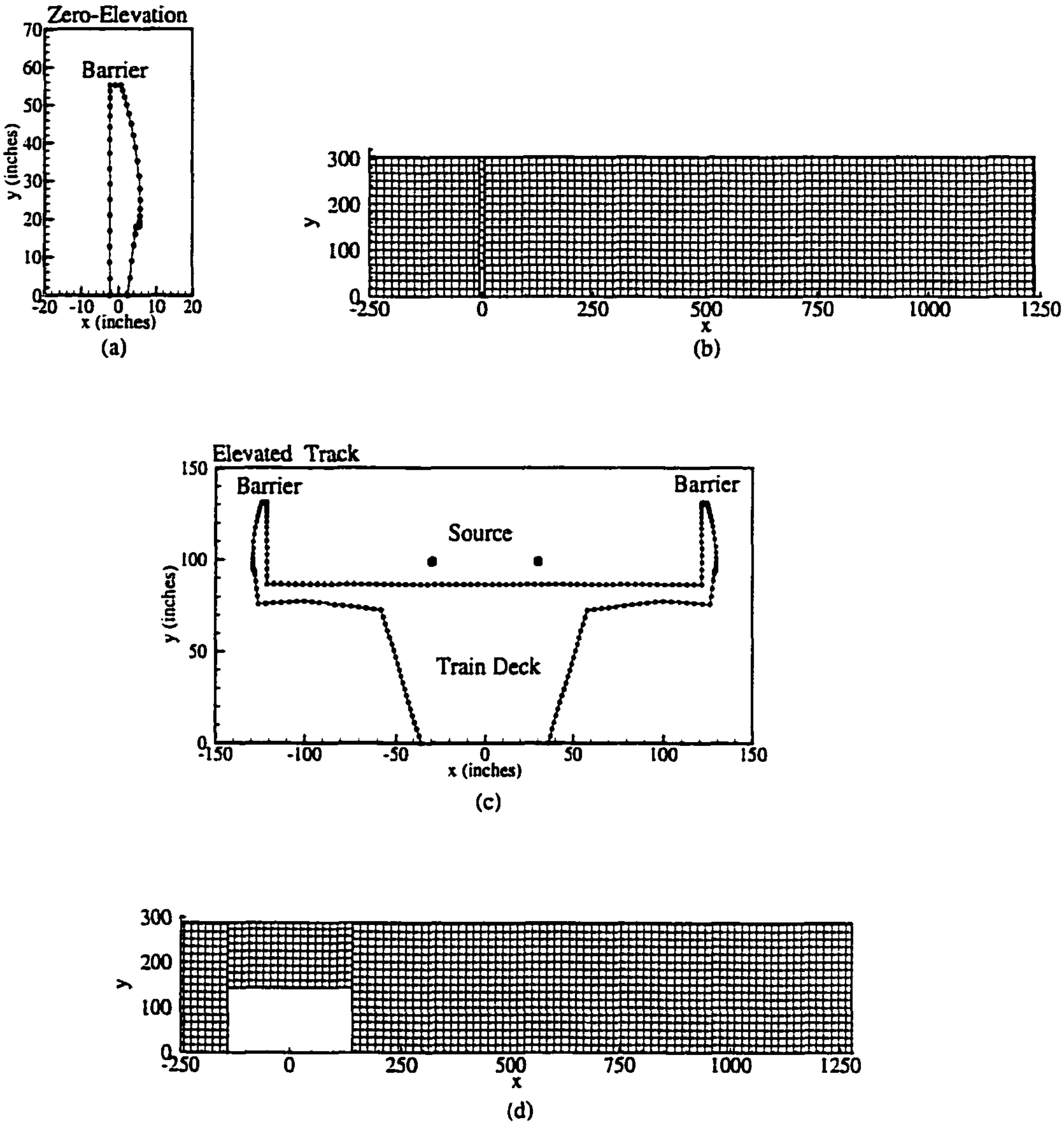
Zero-Elevation
Barrier
y (inches)
x (inches)
70
60
50
40
30
20
10
0
-20
-10
0
10
20
(a)
300
200
100
0
y
-250
0
250
500
750
1000
1250
x
(b)
Elevated Track
Barrier
Barrier
Source
Train Deck
y (inches)
x (inches)
150
100
50
0
-150
-100
-50
0
50
100
150
(c)
300
200
100
0
y
-250
0
250
500
750
1000
1250
x
(d)

Figure 5.7 Surface and domain grids. (a) & (b) Zero-elevation case; (c) & (d) Elevated case.

Frequency	62.5 Hz	125 Hz	250 Hz	500 Hz	1000 Hz	2000 Hz	4000 Hz
PPW	48	48	30	28	20	12	8
N	76	128	152	260	356	420	548

Table 5.2 Results of grid refinement study for on-ground configuration.

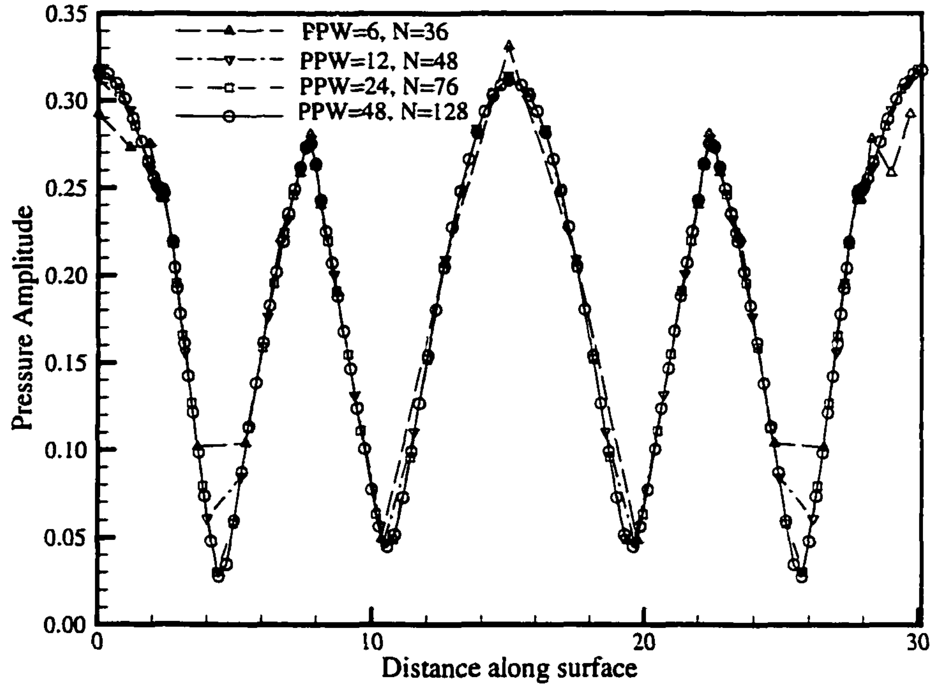

Figure 5.8 Grid refinement study for on-ground barrier at *f*=125 Hz.

5.7 Straight Single Track at Zero-Elevation

Demonstrated in figure 5.9 is the dependence of the noise reduction effectiveness of the barrier on the frequency of the noise. Shown in this figure is the insertion loss (IL), which is defined by,

$$IL=SPL_{\text{without barrier}}-SPL_{\text{with barrier}} \quad (5.39)$$

In front of the barrier (negative-x region), the interference between the incident and the reflected waves is strong. As a result of this interference, the pressure magnitude may increase (negative insertion loss) or decrease (positive insertion loss). It is obvious that the insertion loss has higher values for *f*=1000 Hz case. This indicates that the barrier is more effective at higher frequencies. This is a general trend and is not limited to the current example. This may be explained by the ability of the large wavelength waves (larger than barrier top) to bend over the top of the barrier. Thus, much of their energy is transferred to the shadow zone. For small wavelength waves (smaller than barrier top), the shadow zone has only the scattered waves which suffers from scattering energy loss.

A-weighted sound pressure levels are shown in figure 5.10. The level at the calibration point (obtained by equation 5.1) is used to adjust the free constant in the source term. In the far field inside the shadow zone, the insertion loss approximately equals 15 dBA. Negative values in the interference zone indicate higher noise intensity, which is reflected back to the train after the barrier is inserted.

5.8 Straight Single Track on Elevated Deck

With barriers inserted, pressure contours for low and high frequency cases are shown in figure 5.11. Between the two barriers, strong interference occurs among three types of waves: incident, reflected, and scattered waves. This process may enhance or decrease sound energy depending on the surface geometry and source location. For the high frequency case, there is a sharp border between the shadow zone and the interference zone, indicating that the sound energy is well-contained inside the interference zone. Similar to track-on-ground, this figure suggests a higher insertion loss for higher frequencies.

(a) Pressure Contours (f=250 Hz)

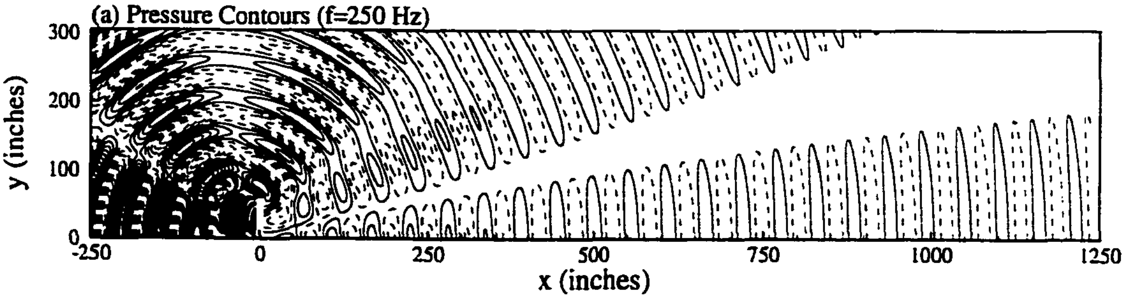

(b) Insertion Loss (f=250 Hz)

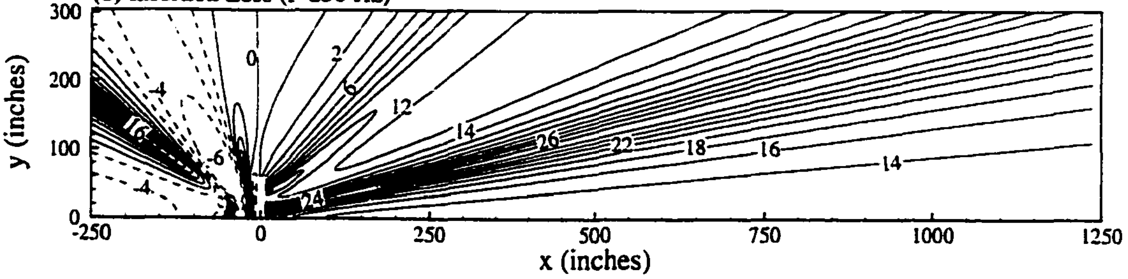

(c) Pressure Contours (f=1000 Hz)

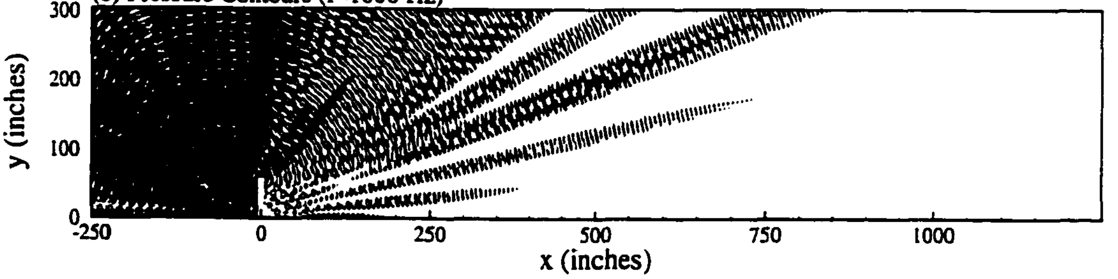

(d) Insertion Loss (f=1000 Hz)

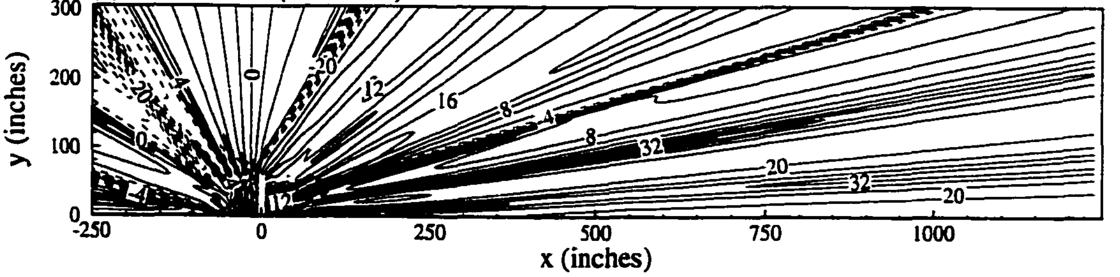

Figure 5.9 Straight single track at zero-elevation. Pressure contours and insertion loss in dB; (a) & (b) *f*=250 Hz; (c) & (d) *f*=1000 Hz. (dashed lines indicate negative values)

(a) SPL_A without Barrier

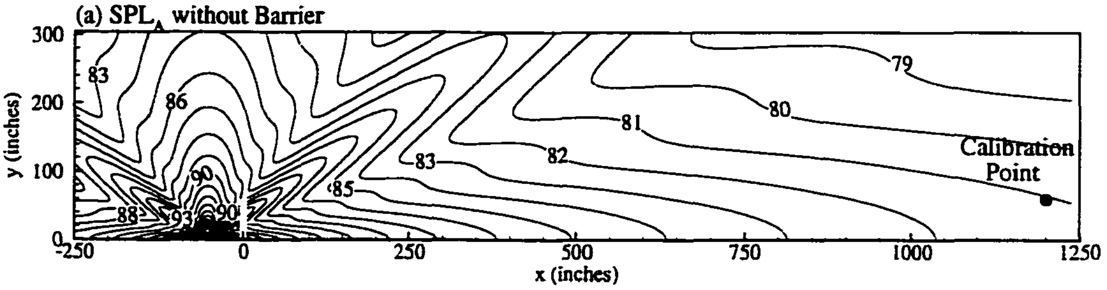

(b) SPL_A with Barrier

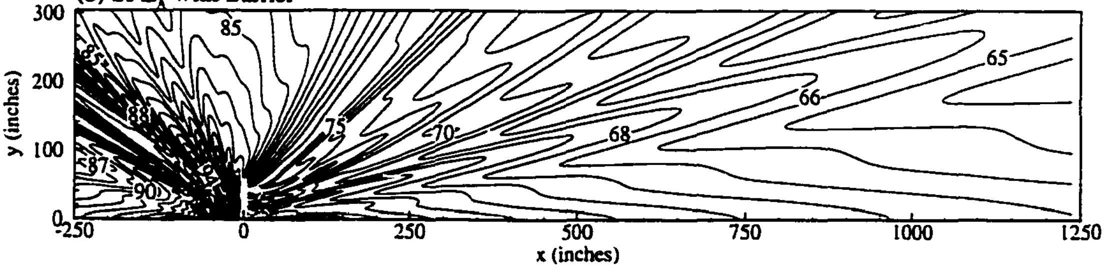

(c) Insertion Loss (dBA)

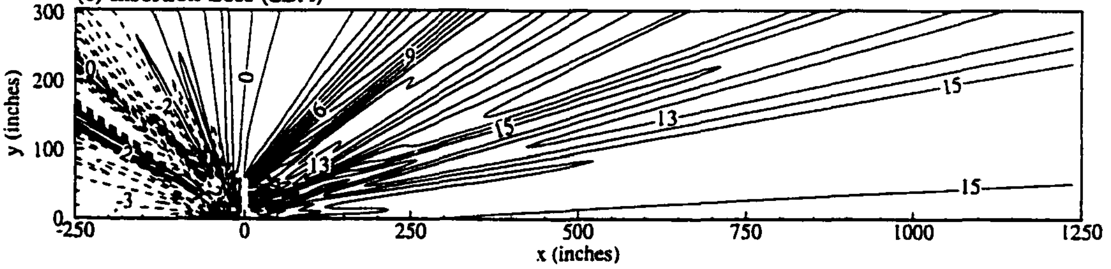

Figure 5.10 Straight single track at zero-elevation. Sound pressure levels in dBA without and with barrier and insertion loss in dBA: (a) SPL_A without barrier, (b) SPL_A with barrier, (c) Insertion loss. (dashed lines indicate negative values)

(a) Pressure Contours (f=250 Hz)

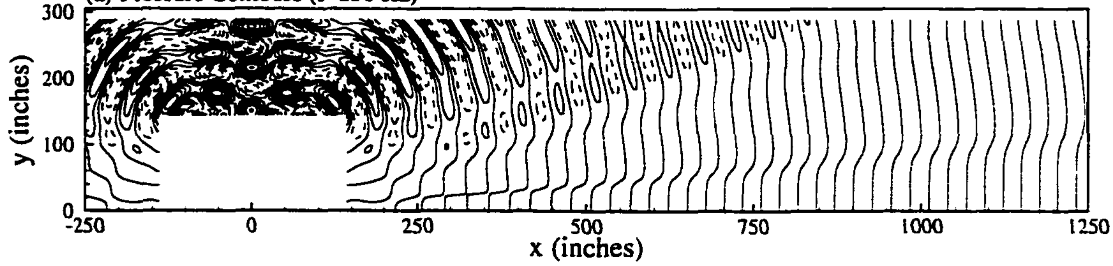

(b) Pressure Contours (f=1000 Hz)

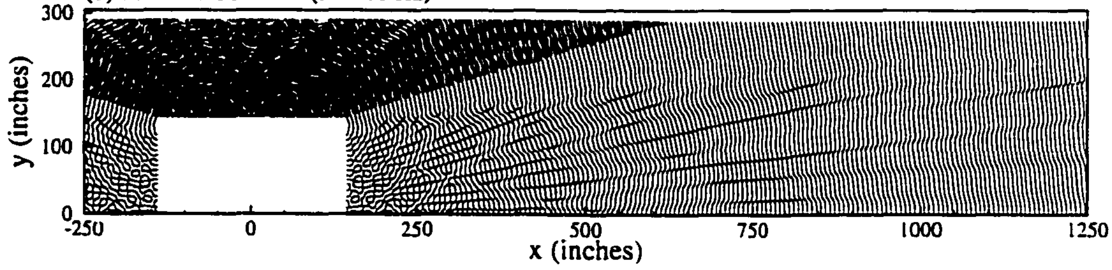

Figure 5.11 Straight single track on elevated deck. Pressure contours: (a) *f*=250 Hz, (b) *f*=1000 Hz.

A-weighted sound pressure levels are shown in figure 5.12. The insertion loss can be obtained from this figure by subtracting the values in figure 5.12-b from these in figure (5.12)-a. In the shadow zone, the insertion loss fluctuates around 4 dBA. This represents a significant reduction in the barrier efficiency as compared with track-on-ground case. A possible reason is the energy enhancement process inside the cavity-shaped space between the two barriers. Inside this space, the reflected waves from the deck surface and the two barriers are interfered with the source-emitted waves and the scattered waves from the barrier tops. Sound energy build-up is the outcome of this interference. Thus, the effective strength of the sound source is increased when the barriers are erected. In other words, the source strength that is felt by the barrier is a magnified version of the original source.

(a) SPL_A without Barrier

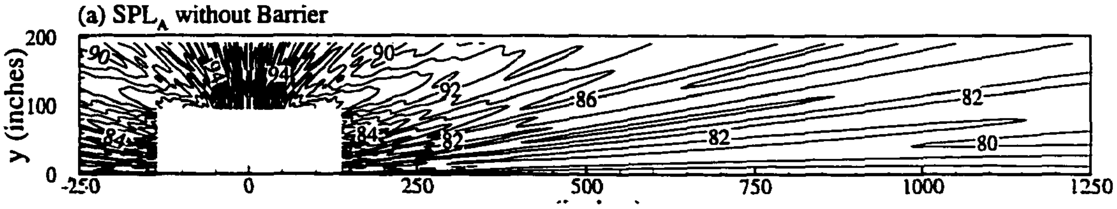

(b) SPL_A with Barrier

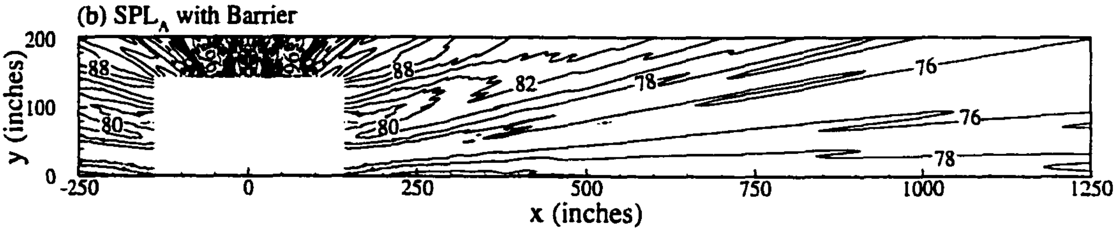

Figure 5.12 Straight single track on elevated deck. Sound pressure levels in dBA: (a) Without barrier, (b) With barrier.

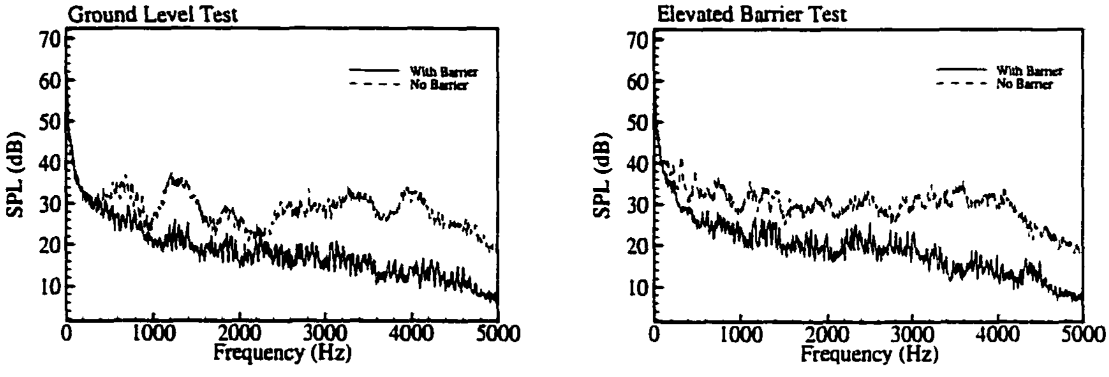

Figure 5.13 Measured sound pressure levels for white noise source. (from Baysal et al. 2000)

5.9 Comparison with Experiment

The sound pressure level at a fixed point in the shadow zone (50 feet from barrier and 5 feet above ground or train deck) was measured by Baysal et al. (2000). Both tonal source at octave frequencies (125 Hz to 1000 Hz) and white noise source were considered. The white noise results are shown in figure 5.13. The equivalent A-weighted sound pressure levels are calculated from these data. For zero-elevation track, the measured A-weighted insertion loss is 10.3 dBA compared with the computed value of 15.5 dBA extracted from the contours in figure 5.10. For the elevated deck case, the measured A-weighted insertion loss is 10.1 dBA compared with the computed value of 8.4 dBA extracted from the contours in figure 5.12. The agreement is deemed reasonable, considering that the experiment was conducted in an open field, which is subjected to all kinds of hazards (wind speed, background noise, reflection from various objects). Also, the train noise spectrum used in the calculations is different from the white noise source used in the experiment.

CHAPTER VI

CONCLUSIONS

6.1 Summary of the Present Work

The main focus in this research has been the computational modeling of noise-producing systems. Efficient CAA codes are developed using both finite difference and finite element methods. Dispersion-relation-preserving finite difference scheme is considered for the solution of the linear and nonlinear Euler equations. The boundary element technique is employed to solve the Helmholtz equation. Benchmark problems are considered to validate the finite difference method. Then, the method is employed to predict the supersonic jet noise. A railway noise barrier is analyzed using the boundary element method. The results compared favorably with available data. The results of this work are published in Baysal, Kaushik, and Idres (1997), Baysal and Idres (1998), and Baysal, Idres, and Kelly (2000).

The benchmark problems include propagation of initial pulse, reflection of pulse by a flat or a curved wall, reflection of time-periodic train of waves by a flat wall, and the solution of an oscillatory sink flow. The theoretical solutions for these problems are also developed. Both the nonreflecting and characteristic boundary conditions are tested. The wall boundary condition based on the ghost points concept is successfully implemented. The numerical results are compared with the theoretical solution and a complete matching is demonstrated.

The noise from the Mach 2.1 perfectly expanded two-dimensional supersonic jet (Troutt and McLaughlin, 1982) is computed using the finite difference method. The turbulent Reynolds averaged Navier-Stokes equations are used to obtain the mean flow. An implicit iterative procedure is employed. At the jet inlet, the instability waves, for Strouhal number of 0.2, are calculated using the compressible Rayleigh equation. Both the axisymmetric and the helical modes are considered. Azimuthal mode decomposition is used to eliminate θ-derivative from the linearized Euler equations. The resulting complex equations are solved for the complex perturbations. The grid is generated based on the curve fitting of the velocity profile. Multi-block time integration technique is developed. Laminar and turbulent mean flow predictions are compared with the experimental/theoretical results. The laminar equations failed to predict the actual growth of the shear layer. The turbulent solution was in good agreement with the experimental/theoretical solution. Discrete Fourier transform analysis of the acoustic field data showed that the numerical solution is free from spurious modes. The sound pressure levels are compared with the experimental data and the computation of Tam and Burton (1984b). Good qualitative agreement is obtained. The axisymmetric mode shows larger peaks of SPL than the helical mode. The multiple time scale integration technique has effectively reduced the computational time. The reduction is estimated to be as much as 75% of the single-block case.

The performance of a railway noise barrier is evaluated using the boundary element technique. First, the integral formulation of the Helmholtz equation is introduced. Linear elements on frequency-dependent surface meshes are used. At least six elements per wavelength are used. The Gauss quadrature method is used to calculate the integrals. The sound source is modeled as a combination of single frequency point sources at the octave values. The amplitudes of these sources are determined from a typical noise spectrum of trains. The elevated and ground-level tracks are analyzed. The barrier insertion loss is computed for the octave frequencies. Moreover, A-weighted sound pressure levels are computed (this weighting is used to calibrate the noise according to human ear sensitivity). As the sound source frequency increases, the insertion loss of the barrier decreases, indicating lower barrier efficiency in reducing noise. For the barrier configuration used in this study, an insertion loss of 15 dBA for the zero-elevation case and 4 dBA for the elevated case are obtained.

6.2 Concluding Remarks

- The resolution of the computational grid is dictated by three factors: (1) accurate representation of the mean flow, i.e., more grid points in high gradient regions; (2) number of grid points per wavelength (PPW), which should be more than 5 points; (3) sufficient resolution and isotropy of the acoustic source, which is ensured by using a sufficient number of grid points to represent the source (more than 6 points) and enforcing a uniform grid near the source.
- For periodic problems, time step is usually determined by the accuracy requirements rather than the stability limits of the numerical scheme. At least 100 time steps per period of oscillation should be used to ensure accurate solution. These small time steps call for the use of the DRP time integration scheme instead of the LDDRK scheme since the first has lower computational cost per time step.

- The failure of the non-reflecting characteristic boundary condition is noticed at the corners of the computational domain. This is due to the incompetence of these boundary conditions when the wave direction is inclined to the boundary.
- When both the mean flow and acoustic perturbations are calculated using the same set of equations, canceling-the-residual technique is recommended. First, the mean flow is obtained to an acceptable accuracy. Second, negatives of the residuals are added to the right hand side of the equations to reduce the residuals to machine zero. Third, the acoustic calculations are turned on.
- Turbulent calculations are important for accurate calculation of the mean flow of the supersonic jet. The laminar solution cannot predict the actual growth rate of the mixing layer.
- Non-axisymmetric mode noise calculations are made possible using the azimuthal mode decomposition technique. Only grids in the axisymmetric plane are required.
- The two-step strategy, based on separating the mean flow calculation from noise computation, has given flexibility and freedom for both steps. In the current work, an implicit low-order scheme is used for jet mean flow calculation, while, an explicit high-order scheme is used to compute the sound field.
- For mean flow with strong gradients, such as jet flow, generalized curvilinear coordinates formulation has given the flexibility and freedom for grid generation.
- For acoustic computations, where both the acoustic far and near fields are captured using the same set of equations, the multiple scales time integration algorithm has a substantial effect on the computational time. Approximately 75% of the single-block computational time has been eliminated in the jet noise problem.

- For problems with complex geometry, such as a noise barrier problem, the use of the boundary element method is the perfect choice. This method does not need domain grid generation and the wall boundary condition is implemented very easily. Without this method, it would be extremely difficult to calculate A-weighted sound pressure levels for the barrier problem.

6.3 Recommendations and Future Work

For the supersonic jet case, the centerline treatment is based on the symmetry boundary condition that requires the exclusion of the centerline grid line, which is the source of singularity in the cylindrical coordinate system. This weak treatment is a source of spurious waves that has to be damped as soon as they are generated. More rigorous treatments are based on the asymptotic form of the governing equations as $r \rightarrow 0$, where the singularity is removed through the use of L'Hopital's rule. The radial derivatives at the centerline are evaluated using one-sided finite difference formulae. This method was suggested by Griffin et al. (1979). They used this technique to simulate the flow field inside an internal combustion engine. The behavior near the centerline was studied by Shih et al. (1995) for three-dimensional supersonic jet calculations. They used three approaches: asymptotic, averaging and interior point. Mohseni and Colonius (1997) wrote a recent article on this subject. They used coordinate transformation to avoid the singularity at the centerline.

In the current research, only the noise from a perfectly expanded supersonic jet is considered. As discussed in section 2.2, there are two other sources of noise for an imperfectly expanded jet, namely, screech tones and broadband shock associated noise.

For such jets, ENO method has great advantages (refer to section 2.1.1.1). It is able to capture shock waves and remain high order in smooth regions of the flow. Several articles are available for consultation including Atkins (1991), Meadows et al. (1994), and Lockard et al. (1995).

Another subject that needs to be investigated is that of jet noise suppression methods. Supersonic jet noise abatement techniques fall inside two main concepts: (1) Geometric concepts, such as multielement suppressors at the nozzle exit plane, ejectors surrounding the jet in the vicinity of the nozzle exit, annular plug, and tabs at the nozzle exit plane and (2) Aerothermodynamic concepts, such as inverted-velocity profile (i.e., a higher velocity jet surrounding a lower velocity jet), thermal acoustic shield (i.e., surrounding either fully or partially the main jet with a jet having a high static temperature and low velocity). Although, these concepts have been investigated by many researchers, these investigations are either experimental or with approximate numerical methods. Gleibe (1980) has studied the noise from multichute suppressors. He concluded that this method does not substantially reduce the mixing noise, while it has major effect on the shock-cell broadband noise component. Tabs are used as vortex generators. They are used to alter the jet flow structure. They can be used to eliminate the screech noise. The effect of tabs has been investigated by Samimy et al. (1993), Wishart et al. (1993), and Tam and Zaman (1999). Tam (1998) and Tam & Zaman (1999) studied the jet noise from different nozzle geometries. They concluded that nozzle geometry modification might not be an effective method for jet noise suppression. The reduction of noise by the introduction of moving fluid layer is investigated by Dosanjh et al. (1971), Tanna (1980), Papamoschou

(1997), Dahl et al. (1998), Shih (1999), and Debiasi (1999). This method has shown great success. As much as 18 dB reduction could be obtained.

For the noise barrier problem, the train geometry is not considered. In more refined analysis, the train geometry should be included. The modeling of noise source would be taken as a line source, instead of point source, with variable intensity. Evaluation of different barrier configurations is required. This includes inclined, T-profiled, Y-profiled, and arrow-profiled barriers. Also, the effect of sound absorptive material needs to be investigated. Higher-order shape functions are needed to treat the singularity problem for the case of absorptive material coating since new singular integrals are introduced into the formulation.

REFERENCES

(In alphabetical order)

Amini, S., and Wilton, D.T., 1986, "An Investigation of Boundary Element Methods for the exterior Acoustic Problem," *Computational Methods in Applied Mechanical Engineering*, Vol. 54, pp. 49-65.

Antes, H, 1991, "Applications in Environmental Noise," *Boundary Element Methods in Acoustics* (R.D. Ciskowski, and C.A. Brebbia, Eds.), pp. 225-257, Computational Mechanics Publications, Boston.

Atkins, H.L., 1991, "High-order ENO Methods for The Unsteady Compressible Navier-Stokes Equations," AIAA Paper 91-1557.

Banaugh, R.P., and Goldsmith, W., 1963, "Diffraction of Steady Acoustic Waves by Surface of Arbitrary Shape," *Journal of Acoustical Society of America*, Vol. 35, pp. 1590-1601.

Bangalore, A., Morris, P.J. and Long, L., 1996, "A Parrallel Three-Dimensional Aeroacoustics Method Using Non-Linear Disturbance Equations," AIAA Paper 96-1728.

Bayliss, A., and Turkel, E., 1982, "Far Field Boundary Conditions for Compressible Flows," *Journal of Computational Physics*, Vol. 48, pp. 182-199.

Baysal, O., and Idres, M.M., 1998, "Euler Computation of Jet Noise: Instability Generated Waves and Their Propagation," AIAA Paper 98-2262.

Baysal, O., and Kaushik, D.K., 1996, "Computation of Acoustic Scattering by a Low-Dispersion Scheme," Second Computational Aeroacoustics Workshop on Benchmark Problems, Tallahassee, FL., NASA Conference Puplication 3352 (Eds. C.K.W. Tam, J.C. Hardin), pp. 57-68.

Baysal, O., Idres, M.M., and Kelly, J.J., 2000, "Acoustical Measurements and Computational Modeling to Evaluate Insertion Loss by Noise Barrier," submitted to 6th AIAA/CEAS Aeroacoustics Conference, Maui, HI.

Baysal, O., Kaushik, D.K, and Idres, M.M., 1997, "Low-Dispersion Scheme for Nonlinear Acoustic Waves in Nonuniform Flow," AIAA Paper 97-1582, Third AIAA/CEAS Aeroacoustics Conference, May 12-14, Atlanta, Georgia.

Baysal, O., Yen, G-W., and Fouladi, K., 1994, "Navier-Stokes Computations of Cavity Aeroacoustics with Suppression Devices," *Journal of Vibration and Acoustics*, Vol. 116, pp. 105-112.

Berenger, J.P., 1994, "A Perfectly Matched Layer for the Absorption of Electromagnetic Waves," *Journal of Computational Physics*, Vol. 114, pp. 182-200.

Casper, J., Shu, C.-W, and Atkins, H.L., 1994, "Comparison of two formulations for high-order accurate essentially non-oscillatory schems," *AIAA Journal*, Vol. 32, No. 10.

Chung, C., and Morris, P.J., 1995, "Acoustic Scattering from Two and Three-Dimensional Bodies," Proceedings of the First Joint CEAS/AIAA Aeroacoustics Conference, June 1995, Munich, Germany, pp. 55-63.

Colonius, T., Lele, S.K., and Moin, P., 1993, "Boundary Conditions for Direct Computation of Aerodynamic Sound Generation," *AIAA Journal*, Vol. 31, pp. 1574-1582.

Colonius, T., Lele, S.K., Moin, P., 1997, "Sound Generation in a Mixing Layer," *Journal of Fluid Mechanics*, Vol. 330, pp. 375-409.

Crighton, D.G., and Huerre, P., 1990, "Shear-Layer Pressure Fluctuations and Superdirective Acoustic Sources," *Journal of Fluid Mechanics*, Vol. 220, pp. 355-368.

Dahl, M.D., and Morris, P.J., 1997, "Noise From Supersonic Coaxial Jets, Part 1: Mean Flow Predictions," *Journal of Sound and Vibration*, Vol. 200, No. 5, pp. 643-663.

Dahl, M.D., Papamoschou, D., and Hixon, R., 1998, "Supersonic Coaxial Jets: Noise Predictions and Measurements," AIAA Paper 98-2294.

Debiasi, M., and Papamoschou, D., 1999, "Acoustics of Under- and Over-Expanded Coaxial Jets," AIAA Paper 99-0081, 37th AIAA Aerospace Sciences Meeting and Exhibit, January 11-14, Reno, NV.

Dosanjh, D.S., Yu, J.C., Abdelhamid, A.N., 1971, "Reduction of Noise from Supersonic Jet Flows," *AIAA Journal*, Vol. 9, No. 12, pp. 2346-2353.

Duhamel, D., Sergent, P., Hua, C., and Cintra, D., 1998, "Measurement of Active Control Efficiency Around Noise Barriers," *Applied Acoustics*, Vol. 55, No. 3, pp. 217-241.

Elmore, W.C., and Heald, M.A., 1969, *Physics of Waves*, McGraw-Hill, Tokyo.

Embleton, T.F.W., 1980, "Line Integral Theory of Barrier Attenuation," *Journal of Acoustical Society of America*, Vol. 67, pp. 42-45.

Engquist, B., and Majda, A., 1977, "Absorbing Boundary Conditions fot the Numerical Simulation of Waves," *Mathematics of Computation*, Vol. 31, pp. 629-651.

Farassat, F., 1996, "Introduction to Generalized Functions with Applications in Aerodynamics and Aeroacoustics," NASA Technical Paper 3428.

Freund, J.B., 1997, "Proposed Inflow/Outflow Boundary Condition for Direct Computation of Aerodynamic Sound," *AIAA Journal*, Vol. 35, pp. 740-742.

Givoli, D., 1991, "Non-reflecting Boundary Conditions," *Journal of Computational Physics*, Vol. 94, May 1991, pp. 1-29.

Gleibe, P.R., 1980, "Diagnostic Evaluation of Jet Noise Suppression Mechanisms," *Journal of Aircraft*, Vol. 17, No. 12, pp. 837-842.

Goldstein, M.E., 1984, "Aeroacoustics of Turbulent Shear Flows," *Annual Review of Fluid Mechanics*, Vol. 16, pp. 263-285.

Gottleib, D., and Turkel, E., 1976, "Disspative Two-Four Method for Time Dependent Problems," *Mathematics of Computation*, Vol. 30, No. 136, pp. 703-723.

Griffen, M.D., Jones, E., and Anderson, J., 1979, "A Computational Fluid Dynamic Technique Valid at the Centerline for Non-Axisymmetic Problems in Cylindrical Coordinates," *Journal of Computational Physics*, Vol. 30, pp. 352-360.

Habault, D., 1985, "Sound Propagation above an Inhomogeneous Plane: Boundary Integral Equations Methods, " *Journal of Sound and Vibration*, Vol. 100, pp. 55-67.

Hagstrom, T., and Hariharan, S.I., 1988, "Accurate Boundary Conditions for Exterior Problems in Gas Dynamics," *Mathematics of Computation*, Vol. 51, pp. 581-597.

Hanson, C.E., Saurenman, H.J., and Towers, D.A., 1994, "Rail Transport Noise and Vibration," Capter 46, *Handbook of Acoustical Measurements and Noise Control* (P. Harris, Ed.), McGraw Hill.

Hayder, M.E., and Turkel, E., 1996, "On Buffer Layers as Non-reflecting Computational Boundaries," AIAA Paper 96-0273.

Higdon, R.L., 1986, "Abosrbing Boundary Conditions for Difference Approximations to Multi-Dimensional Wave Equation," *Mathematics of Computation*, Vol. 47, pp. 629-651.

Hixon, R. , Shih, S.-H., and Mankbadi, R.R., 1995a, "Direct Prediction of the Three-Dimensional Acoustics Field of a Supersonic Jet Using Linearized Euler Equations", CEAS/AIAA-95-116, June 1995.

Hixon, R., 1997, "On Increasing The Accuracy of MacCormack schemes for Aeroacoustic Applications," AIAA 97-1586.

Hixon, R., Shih, S.-H, and Mankbadi, R.R., 1995b, "Numerical Simulation of the effect of Heating on Jet Noise," FED-Vol. 219, *Computational Aeroacoustics*, ASME, pp. 89-94.

Hixon, R., Shih, S.-H, and Mankbadi, R.R., 1996, "Effect of Inflow Disturbance on Linearized Euler Equation Prediction of Jet Noise," AIAA Paper 96-0752.

Hothersall, D.C., Crombie, D.H., and Chandler-Wilde, 1991, "The Performance of T-profile and Associated Noise Barriers," *Applied Acoustics*, Vol. 32, pp. 269-287.

Hu, F.Q., 1996a, "On Absorbing Boundary Conditions for Linearized Euler Equations by Perfectly Matched Layer," *Journal of Computational Physics*, Vol. 129, pp. 201-219.

Hu, F.Q., 1996b, "On Perfectly Matched Layer as an Absorbing Boundary Condition," AIAA Paper 96-1664.

Hu, F.Q., Hussaini, M.Y., and Manthey, J., 1994, "Application of Low Dissipation and Dispersion Runge-Kutta Schemes to Benchmark Problems in Computational Aeroacoustics," ICASE/LaRC Workshop on Benchmark Problems in Computational Aeroacoustics, Hampton, Virginia, Oct. 24-26, 1994.

Isei, T., 1980, "Absorbtive Noise Barrier on Finite Impedence Ground," *Journal of Acoustical Society of Japan*, Vol. 1.

Isei, T., Embleton, T.F., and Piercy, J.E., 1980, "Noise Reduction by Barriers on Finite Impedance Ground," *Journal of Acoustical Society of America*, Vol. 67, pp. 46-58.

Kaushik, D.K., and Baysal, O., 1996, "Algorithmic Extension of Low-Dispersion Scheme and Modeling Effects for Acoustic Wave Simulation," Proceedings of ASME Fluids Engineering Summer Meeting, FED-Vol. 238, pp. 503-510, The American Society of Mechanical Engineers, New York.

Keller, J.B., 1962, "Geometrical Theory of Diffraction," *Journal of Optical Society of America*, Vol. 52, pp. 116-130.

Kim, J.W, and Lee, D.J., 1996, "Optimized Compact Finite Difference Schemes with Maximum Resolution," *AIAA Journal*, Vol. 34, pp. 887-893.

Kosloff, R., and Kosloff, D., 1986, "Absorbing Boundaries for Wave Propagation Problems," *Journal Of Computational Physics*, Vol. 63, pp. 363-376.

Lau, J.C., Morris, P.J., and Fisher, M.J., 1979, "Measurements in subsonic and supersonic free jets using a laser velocimeter," *Journal of Fluid Mechanics*, Vol. 93, pp. 1-27.

Lele, S.K., 1989, "Direct Numerical Simulation of Compressible Free Shear Layer Flows," Paper 89-0374, 27th Aerospace Sciences Meeting, Reno, Nevada, Jan. 9-12, 1989.

Lele, S.K., 1992, "Compact Finite Difference Schemes with Spectral-like Resolution," *Journal of Computational Physics*, Vol. 103, pp. 16-42.

Lele, S.K., 1997, "Computational Aeroacoustics: A Review," AIAA 97-0018.

Li, Y., 1997, "Wavenumber-Extended High-order Upwind-Biased Finite Difference Schemes for Convective Scalar Transport," *Journal of Computational Physics*, Vol. 133, pp. 235-255.

Lighthill, M.J., 1952, "On Sound Generated Aerodynamically: 1. General Theory," *Proceeding of the Royal Society*, London, Vol. 211, pp. 564-587.

Lighthill, M.J., 1954, "On Sound Generated Aerodynamically: 2. Turbullence as A Source of Sound," *Proceeding of the Royal Society*, London, Vol. 267, pp. 1-32.

Lilley, G.M., 1974, "On the noise from Jets," AGARD CP-131.

Liu, J.T.C., 1974, "Developing Large-Scale Wavelike Eddies and the Near Jet Noise Field," *Journal of Fluid Mechanics*, Vol. 62, pp. 437-464.

Lockard, D.P., Brentner, K.S., and Atkins, H.L., 1995, "High-Accuracy Algorithms for Computational Aeroacoustics," *AIAA Journal*, Vol. 33, pp. 246-251.

MacCormack, R.W., 1969, "The Effect of Viscosity in Hypervelocity Impact Cratering," AIAA Paper 69-354.

Mankbadi, R.R., Hayder, M.E., and Povinelli, L.A., 1994, "Structure of Supersonic Jet Flow and Its Radiated Sound," *AIAA Journal*, Vol. 32, No. 5, pp. 897-906.

Mankbadi, R.R., Hixon, R., Shih, S-H., and Povinelli, L.A., 1995a, "On the Use of Linearized Euler Equatiosn in the Prediction of Jet Noise," AIAA Paper 95-0505.

Mankbadi, R.R., Hixon, R., Shih, S-H., and Povinelli, L.A., 1998, "Use of Linearized Euler Equations for Supersonic Jet Noise Prediction,"' *AIAA Journal*, Vol. 36, No. 2, pp. 140-147.

Mankbadi, R.R., Shih, S-H., Hixon, R., and Povinelli, L.A., 1995b, "Direct Computation of Sound Radiation by Jet Flow Using Large-Scale Equations," AIAA Paper 95-0680, 33rd AIAA Aerospace Sciences Meeting, Reno, NV, January, 1995.

May, D.N., and Osman, M.M., 1980, "Highway Noise Barriers: New Shapes," *Journal of Sound and Vibration*, Vol. 71, No. 1, pp. 73-101.

McLaughlin, D.K., Morrison, G.L., and Troutt, T.R., 1975, "Experiments on Instability Waves in a Supersonic Jet and Their Acoustic Radiation," *Journal of Fluid Mechanics*, Vol. 69, pp. 73-95.

McLaughlin, D.K., Morrison, G.L., and Troutt, T.R., 1977, "Reynolds Number Dependence in Supersonic Jet Noise," *AIAA Journal*, Vol. 15, pp. 526-532.

Meadows, K.R., Caughey, D.A., and Casper, J., 1994, "Computing Unsteady Shock Waves for Aeroacoustics Applications," *AIAA Journal*, Vol. 32, No. 7, pp. 1360-1366.

Mitchell, B.E., Lele, S.K., and Moin, P., 1996, "Direct Computation of the Sound Generated by Subsonic and Supersonic Axisymmetric Jets," Rep. TF-66, Thermoscience Division, Dept. of Mechanical Engineering, Stanford University.

Mohsni, K, and Colonius, T., 1997, "Numerical Treatment of Polar Coordinate Singularities in Finite Difference and Pseudo-spectral Schemes," to appear in Journal of Computational Physics.

Morris, P.J, Long, L.N., Scheidegger, T.E., Wang, Q., and Pilon, A.R., 1998, "High Speed Jet Noise Simulations," AIAA Paper 98-2290.

Morris, P.J., and Tam, C.K., 1979, "On the Radiation of Sound by Instability Waves of a Compressible Axisymmetric Jet," *Mechanics of Sound Generation in Flows*, Springer-Verlag, Berlin, p. 55.

Morris, P.J., Long, L.N., Bangalore, A., and Wang, Q., 1997, "A Parallel Three-Dimensional Computational Aeroacoustics Method Using Nonlinear Disturbance Equations," *Journal of Computational Physics*, Vol. 133, pp. 56-74.

Morrison, G.L., and McLaughlin, D.K., 1979, "The Noise Generated by Instabilities in Low Reynolds Number Supersonic Jets," *Journal of Sound and Vibration*, Vol. 65, No. 2, pp. 171-191.

Morrison, G.L., and McLaughlin, D.K., 1980, "Instability Process in Low Reynolds Number Supersonic Jets," *AIAA Journal*, Vol. 18, No. 7, pp. 793-800.

Oretel, H., 1979, "Mach Wave Radiation of Hot Supersonic Jets," *Mechanics of Sound Generation in Flows*, (ed. E.A. Muller), pp. 275-281, Springer.

Oretel, H., 1982, "Coherent Structures Producing Mach Waves Inside and Outside of the Supersonic Jet," *Structure of Complex Turbulent Shear Flow*, IUTAM Symp., Marseille.

Owis, F., 1999, "Jet Stability and Noise Computations Using Direct Numerical Simulation," Ph.D. Thesis, Department of Aerospace Engineering, Old Dominion University, Norfolk, VA.

Panda, J., Raman, G., and Zaman, K.B., 1997, "Uderexpanded Screeching Jets From Circular, Rectangular, and Elliptic Nozzles," AIAA Paper 97-1623.

Papamoschou, D., 1997, "Mach Wave Elimination in Supersonic Jets," *AIAA Journal*, Vol. 35, No. 10, pp. 1604-1611.

Poinsot, T.J and Lele, S.K., 1992, "Boundary Conditions for Direct Simulations of Compressible Viscous Flows," *Journal of Computational Physics*, Vol. 101, July 1992, pp. 104-129.

Samimy, M., Zaman, K.B., and Reeder, M.F., 1993, "Effects of Tabs on the Flow and Noise Field of an Axisymmetric Jet," *AIAA Journal*, Vol. 31, No. 4, pp. 609-619.

Sankar, L. N., Reddy, N. N., and Harihan, N., 1993, "A Comparative Study of Numerical Schemes for Aero-Acoustic Applications," *Computational Aero- and Hydro-Acoustics*, Vol. 147, Fluid Engineering Div., ASME, New York, pp. 35-40.

Scott, J.N., 1991, "Numerical Analysis of Noise Generation in Unsteady Jet Flow," AIAA Paper 91-2254.

Scott, J.N., 1992, "Acoustic Analysis Using Numerical Solutions of Navier-Stokes Equations," AIAA Paper 92-0506, 30th Aerospace Sciences Meeting, Reno, NV, Jan. 6-9, 1992.

Seiner, J.M., Baht, T.R.S., and Ponton, M.K., 1993, "Mach Wave Emission from a High Temperature Supersonic Jets," AIAA Paper 93-0734.

Shaw, R.P., 1991, "A Brief History of Boundary Integral Equation/Element Methods in Acoustics," *Boundary Element Methods in Acoustics* (R.D. Ciskowski, and C.A. Brebbia, Eds.), pp. 1-9.

Shaw, R.P., Fukui, T., and Wang, H.C., 1988, "Boundary Integral Equation/Element Methods in Computational Acoustics," *Computational Acoustics Wave Propagation* (D. Lee, M.A. Sternberg and M.H. Schultz, Eds.), pp. 157-176, Elsevier, Amsterdam.

Shih, C., Alvi, F.S., and Washigton, D.M., 1999, "Effects of Counterflow on the Aroacoustic Properties of a Supersonic Jet," *Journal of Aircraft*, Vol. 36, No. 2, pp. 451-457.

Shih, S.H., Hixon, D.R., Mankbadi, R.R., 1995, "Three Dimensional Structure in a Supersonic Jet: Behavior Near Centerline," AIAA Paper 95-0681, 33rd Aerospace Sciences Meeting and Exhibit, January 9-12, Reno, NV.

Shih, S.H., Hixon, D.R., Mankbadi, R.R., and Povinelli, L.A., 1998, "Large-Scale Simulation of Supersonic Jet Noise," AIAA Paper 98-3014.

Sinha, N., Dash., S.M., York, B.J., and Lee, R.A., 1991, "Prediction of Jet Mean Flow Structure in Support of HSCT Noise Suppression Concepts," AIAA Paper 91-2253.

Ta'asan, S., and Nark, D.M., 1995, "An Absorbing Buffer Zone Technique for Acoustic Wave Propagation," AIAA Paper 95-0164.

Tam, C.K., 1998, "Influence of Nozzle Geometry on the Noise of High-Speed Jets," AIAA Paper 98-2255.

Tam, C.K., and Zaman, K.B, 1999, "Subsonic Jet Noise from Non-Axisymmetric and Tabbed Nozzles," AIAA Paper 99-0077, 37th AIAA Aerospace Sciences Meeting and Exhibit, January 11-14, Reno, NV.

Tam, C.K.W, and Dong, Z., 1994, "Wall Boundary Conditions for High-Order Finite Difference Schemes in Computational Aeroacoustics," AIAA Paper 94-0457.

Tam, C.K.W., 1997, "Advances in Numerical Boundary Conditions for Computational Aeroacoustics," AIAA Paper 97-1774.

Tam, C.K.W., and Burton, D.E., 1984a, "Sound Generated by Instability Waves of Supersonic Flows. Part 1. Two-Dimensional Mixing Layers," *Journal of Fluid Mechanics*, Vol. 138, pp. 249-271.

Tam, C.K.W., and Burton, D.E., 1984b, "Sound generated by instability waves of supersonic flows. Part 2. Axisymmetric jets," *Journal of Fluid Mechanics*, Vol. 138, pp. 273-295.

Tam, K.W., and Shen, H., 1993, "Direct Computation of Nonlinear Acoustic Pulse Using High Order Finite Difference Schemes," AIAA Paper 93-4325.

Tam, K.W., and Webb, J.C., 1993, "Dispersion-Relation-Preserving Finite Difference Schemes for Computational Acoustics," *Journal of Computational Physics*, Vol. 107, pp. 262-283.

Tanna, H.K., 1980, "Coannular Jets: Are They Realy quit and Why?," Journal of Sound and Vibration, Vol. 72, No. 1, pp. 97-118.

Thomasson, S.I.,1977, *Theory and Experiments on Sound Propagation above an Impedance Boundary*, Rep. 75, Division of Building Technology, Lund Inst. Technology, Lund, Seweden.

Thompson, K.W., 1987, "Time-dependent Boundary Conditions for Hyperbolic Systems," *Journal of Computational Physics*, Vol. 68, pp. 1-24.

Thompson, K.W., 1990, "Time-dependent Boundary Conditions for Hyperbolic Systems II," *Journal of Computational Physics*, Vol. 89, 1990, pp. 439-461.

Troutt, T.R., 1978, "Measurements on The Flow and Acoustic Properties of a Moderate-Reynolds-Number Supersonic Jet," Ph.D. thesis, Oklahoma State University.

Troutt, T.R., and McLaughlin, D.K., 1982, "Experiments on the flow and acoustic properties of a moderate Reynolds number supersonic jet," *Journal of Fluid Mechanics*, Vol. 116, pp. 123-156.

Vanel, F.O, and Baysal, O., 1997, "Investigation of Dispersion-Relation-Preserving Scheme and Spectral Analysis Methods for Acoustic Waves," *Journal of Vibration and Acoustics*, Vol. 119, pp. 250-257.

Vichenevetsy, R., and Bowels, J.B., 1982, *Fourier Analysis of Numerical Approximations of Hyperbolic Equations*, SIAM, Philadelphia.

Viswanathan, K., and Sankar, L.N., 1995, "Toward the Direct Calculation of Noise: Fluid/Acoustic Coupled Simulation," *AIAA Journal*, Vol. 33, pp. 2271-2279.

Webb, J.C., 1993, "Finite Difference Algorithms for Computational Acoustics and a Numerical 2-D Supersonic Jet Simulation," Ph.D. Thesis, Department of Mathematics, Florida State University, Tallahassee, FL.

Wishart, D.P., Krothapalli, A., and Mungal, M.G., 1993, "Supersonic Jet Control Via Point Disturbances Inside the Nozzle," *AIAA Journal*, Vol. 31, No. 7, pp. 1340-1341.

APPENDIX A

FINITE DIFFERENCE SCHEME

A.1 Dispersion-Relation-Preserving Scheme

This scheme was introduced by Tam and Webb (1993). The following is a summary of the steps used to develop the scheme.

(1) Consider the approximation of the first derivative,

$$\left(\frac{\partial f}{\partial x}\right)_\ell = \frac{1}{\Delta x}\sum_{j=-N}^{M} a_j f_{\ell+j} \tag{A.1}$$

(2) Apply Fourier transform,

$$i\alpha\tilde{f} = \frac{1}{\Delta x}\sum_{j=-N}^{M} a_j e^{i\alpha j\Delta x}\tilde{f} \tag{A.2}$$

(3) Define the *effective* wave number of the space discretization scheme as,

$$\overline{\alpha} = \frac{-i}{\Delta x}\sum_{j=-N}^{M} a_j e^{i\alpha j\Delta x} \tag{A.3}$$

(4) Coefficients, a_j, are obtained as one-parameter family using the traditional Taylor series method (to insure desired accuracy). The remaining coefficient is obtained from minimizing the following integrated error

$$E = \int_{\varepsilon}^{\varepsilon} |\alpha\Delta x - \overline{\alpha}\Delta x| \, d(\alpha\Delta x) \tag{A.4}$$

where $\varepsilon = 2\pi\Delta x/\lambda_{\min}$; $\lambda_{\min}$ is the shortest wavelength to be simulated. Since at least five grid points are needed to represent a wave, $\lambda_{\min} \geq 4\Delta x$, i.e. $\varepsilon \leq \pi/2$. The coefficients of the fourth-order DRP scheme is listed in table A.1 for $\varepsilon = \pi/2$.

A.1.2 Time Integration

(1) Consider four-level time integration,

$$q(t+\Delta t)-q(t)=\Delta t\sum_{k=0}^{3} b_k \frac{d}{dt}U(t-k\Delta t) \qquad \text{(A.5)}$$

(2) Apply Laplace transform,

$$(e^{-i\omega\Delta t}-1)\tilde{q}=(\Delta t\sum_{k=0}^{3} b_k e^{ik\omega\Delta t})(-i\omega\tilde{q}) \qquad \text{(A.6)}$$

(3) Define the *effective* angular frequency of the time discretization scheme as,

$$\bar{\omega}=\frac{i(e^{-i\omega\Delta t}-1)}{\Delta t\sum_{k=0}^{3} b_k e^{ik\omega\Delta t}} \qquad \text{(A.7)}$$

(4) Coefficients, b_k, are obtained as one-parameter family using the traditional Taylor series method (to ensure desired accuracy). The remaining coefficient is obtained from minimizing the integrated error,

$$E=\int_{-0.5}^{0.5}\{\sigma[\mathrm{Re}(\bar{\omega}\Delta t-\omega\Delta t)]^2+(1-\sigma)[\mathrm{Im}(\bar{\omega}\Delta t-\omega\Delta t)]^2\}d(\omega\Delta t) \qquad \text{(A.8)}$$

where σ is the weight on the real part. The coefficients of the 4-stage DRP time integration scheme are listed in table A.2.

A.2 The Low Dispersion and Dissipation Runge-Kutta Time Integration Scheme

Hu et al. (1996) developed this scheme by minimizing the dissipation and dispersion errors. For p-stage scheme,

$$\begin{aligned} &\bar{q}^{k}=q^{n}+b_k\Delta t\frac{d\bar{q}^{k-1}}{dt}\ ; \qquad && k=0,1,2,\ldots,p-1 \\ &q^{n+1}=\bar{q}^{p-1} && \end{aligned} \qquad \text{(A.9)}$$

where $b_0=0$ and b_k is obtained from

$$c_k = \prod_{m=2}^{k} b_{p-m+1}; \qquad k=2,\cdots,p \qquad \text{(A.10)}$$

where c_k are obtained by dispersion error minimization in addition to the Taylor series conditions to assure accuracy. The coefficients of the 5-stage LDDRK scheme are listed in table A.2.

A.3 Numerical Stability

The CFL condition for DRP scheme is (Tam and Webb 1993)

$$\Delta t \le \frac{CFL}{1.75[M+\sqrt{(1+(\frac{\Delta x}{\Delta y})^2}]} \qquad \text{(A.11)}$$

where

M is the axial Mach number,

$$CFL = \begin{cases} 0.4 & DRP(O(\Delta x^4), O(\Delta t^3)) \\ 2.14 & DRP(O(\Delta x^4))\ and\ LDDRK(O(\Delta t^2)) \end{cases}$$

To minimize numerical damping introduced by time integration, the CFL number is reduced to,

$$CFL = \begin{cases} 0.19 & DRP(O(\Delta x^4), O(\Delta t^3)) \\ 1.17 & DRP(O(\Delta x^4))\ and\ LDDRK(O(\Delta t^2)) \end{cases} \qquad \text{(A.12)}$$

Damping coefficients, d_k, and multiple time scales time integration coefficients, $b_k^{(\delta)}$, are listed in table A.3 and table A.4 respectively.

N	a_N	a_{N+1}	a_{N+2}	a_{N+3}	a_{N+4}	a_{N+5}	a_{N+6}
-6 (Fully Backward)	-2.192280	4.748611	-5.108852	4.461567	-2.833499	1.128329	-0.203876
-5	-0.209338	-1.084876	2.147776	-1.388928	0.768950	-0.281815	0.048230
-4	0.049042	-0.468840	-0.474761	1.273275	-0.518485	0.166139	-0.026369
-3 (Central)	-0.026520	0.189413	-0.799266	0.000000	0.799266	-0.189413	0.026520
-2	0.026369	-0.166139	0.518485	-1.273275	0.474761	0.468840	-0.049042
-1	-0.048230	0.281815	-0.768950	1.388928	-2.147776	1.084876	0.209338
0 (Fully Forward)	0.203876	-1.128329	2.833499	-4.461567	5.108852	-4.748611	2.192280

Table A.1 DRP coefficients for 7-point stencil fourth-order scheme.

scheme	b_0	b_1	b_2	b_3	b_4
DRP ($O(\Delta t^3)$, σ=0.36)	2.302558	-2.491007	1.574340	-0.385891	-
LDDRK ($O(\Delta t^2)$, 5-stage)	0.000000	0.193492	0.242361	0.325994	0.500000

Table A.2 Time integration coefficients.

N	d_N	d_{N+1}	d_{N+2}	d_{N+3}	d_{N+4}	d_{N+5}	d_{N+6}
-3	0.023853	0.106304	-0.226147	0.287393	-0.226147	0.106304	-0.023853
-2	-	0.0625	-0.25	0.375	-0.25	0.0625	-
-1	-		-0.25	0.5	-0.25	-	-

Table A.3 Selective damping coefficients.

δ	b_0	b_1	b_2	b_3
1/4	0.313198	-0.108864	0.059385	-0.013719
1/2	0.776002	-0.494674	0.286340	-0.067669
3/4	1.425785	-1.253919	0.761731	-0.183598
1	2.302558	-2.491007	1.574340	-0.385891

Table A.4 Multiple time integration coefficients.

APPENDIX B

EXACT SOLUTIONS OF THE LINEARIZED EULER EQUATIONS

B.1 Gaussian pulse in uniform mean flow in x-direction

For the initial value problem:

At $t=0$: $$u=v=0 \quad \text{and} \quad p=\rho=\varepsilon e^{-\alpha((x-x_s)^2+(y-y_s)^2)} \qquad \text{(B.1)}$$

Where ε is the pulse amplitude, α is the spreading parameter and (x_s,y_s) is the pulse location. The exact solution of the linearized Euler equations is (Tam and Webb, 1993),

$$u=\frac{\varepsilon(x-M_0t)}{2\alpha\eta}\int_0^\infty e^{-\frac{\xi^2}{4\alpha}}\sin(\xi t)\,J_1(\xi\eta)\,\xi\,d\xi \qquad \text{(B.2)}$$

$$v=\frac{\varepsilon y}{2\alpha\eta}\int_0^\infty e^{-\frac{\xi^2}{4\alpha}}\sin(\xi t)\,J_1(\xi\eta)\,\xi\,d\xi \qquad \text{(B.3)}$$

$$p=\rho=\frac{\varepsilon}{2\alpha}\int_0^\infty e^{-\frac{\xi^2}{4\alpha}}\cos(\xi t)\,J_0(\xi\eta)\,\xi\,d\xi \qquad \text{(B.4)}$$

where

$\eta=[(x-x_s-M_0t)^2+(y-y_s)^2]^{1/2}$,

J_0 and J_1 are Bessel functions,

M_0 is the mean flow Mach number.

B.2 Gaussian pulse in uniform mean flow in x-direction reflected from flat wall

For an initial conditions as in B.1, and wall along y=0 line, using image method, the exact solution of the linearized Euler equations is,

$$u = \frac{\varepsilon(x - M_0 t)}{2\alpha} \int_0^\infty e^{-\frac{\xi^2}{4\alpha}} \sin(\xi t)\left(\frac{J_1(\xi\eta)}{\eta} + \frac{J_1(\xi\eta')}{\eta'}\right)\xi \, d\xi \tag{B.5}$$

$$v = \frac{\varepsilon y}{2\alpha} \int_0^\infty e^{-\frac{\xi^2}{4\alpha}} \sin(\xi t)\left(\frac{J_1(\xi\eta)}{\eta} + \frac{J_1(\xi\eta')}{\eta'}\right)\xi \, d\xi \tag{B.6}$$

$$p = \rho = \frac{\varepsilon}{2\alpha} \int_0^\infty e^{-\frac{\xi^2}{4\alpha}} \cos(\xi t)\left(J_0(\xi\eta) + J_0(\xi\eta')\right)\xi \, d\xi \tag{B.7}$$

where

$\eta = [(x - x_s - M_0 t)^2 + (y - y_s)^2]^{1/2}$, and $\eta' = [(x - x_s - M_0 t)^2 + (y + y_s)^2]^{1/2}$

B.3 Periodic Source Reflected from Flat Wall at y=0

For no mean flow and periodic source term added to the energy equation, the linearized Euler equations are,

$$\frac{\partial \rho}{\partial t} + \frac{\partial u}{\partial x} + \frac{\partial v}{\partial y} = 0 \tag{B.8}$$

$$\frac{\partial u}{\partial t} + \frac{\partial p}{\partial x} = 0 \tag{B.9}$$

$$\frac{\partial v}{\partial t} + \frac{\partial p}{\partial y} = 0 \tag{B.10}$$

$$\frac{\partial p}{\partial t} + \frac{\partial u}{\partial x} + \frac{\partial v}{\partial y} = s(x, y, t) \tag{B.11}$$

where

$$s(x, y, t) = \varepsilon e^{-\alpha((x - x_s)^2 + (y - y_s)^2)} \cos(\omega t) \tag{B.12}$$

By eliminating u and v, the wave equation for p is,

$$\frac{\partial^2 p}{\partial t^2}-(\frac{\partial^2 p}{\partial x^2}+\frac{\partial p}{\partial y^2})=\frac{\partial s(x,y,t)}{\partial t}$$

$$=\varepsilon e^{-\alpha((x-x_s)^2+(y-y_s)^2)}(-\omega\sin(\omega t))$$

$$=\varepsilon e^{-\alpha((x-x_s)^2+(y-y_s)^2)}\operatorname{Im}(\omega e^{-i\omega t})$$

The solution for pressure, p, can be written as,

$$p(x,y,t)=\operatorname{Im}(\hat{p}(x,y)e^{-i\omega t}) \tag{B.13}$$

Thus, the wave equation becomes

$$\frac{\partial^2 \hat{p}}{\partial x^2}+\frac{\partial \hat{p}}{\partial y^2}+\omega^2\hat{p}=-\omega\varepsilon e^{-\alpha((x-x_s)^2+(y-y_s)^2)} \tag{B.14}$$

Equation B.14 is the non-homogeneous Helmholtz equation. To solve this equation, we use polar coordinates (r_s, θ_s) originated at source location. The equation reduces to the non-homogeneous Bessel equation,

$$\frac{d^2\hat{p}}{dr_s^2}+\frac{1}{r_s}\frac{d\hat{p}}{dr_s{}^2}+\omega^2\hat{p}=-\omega\varepsilon e^{-\alpha r_s^2} \tag{B.15}$$

We consider periodic source in free space (no solid boundaries) with radiation boundary condition as $r_s\to\infty$ and bounded solution at r_s=0. The Greens function for this system is

$$G(r_s,\xi)=\begin{cases}-i\frac{\pi}{2}\xi J_0(\omega r_s)H_0^1(\omega\xi), & 0\le r_s\le\xi\\ -i\frac{\pi}{2}\xi J_0(\omega\xi)H_0^1(\omega r_s), & \xi\le r_s\le\infty\end{cases} \tag{B.16}$$

where J_0 and H_0^1 are the zeroth order Bessel and Hankel functions, respectively.

The solution for $\hat{p}(r_s)$ is,

$$\hat{p}(r_s)=\int_0^\infty G(r_s,\xi)(-\omega\varepsilon e^{-\alpha\xi^2})d\xi \tag{B.17}$$

Using image method, the solution for periodic source near a solid wall at y=0 can be deduced as

$$\hat{p}(r) = \int_0^\infty (G(r_s,\xi) + G(r_s',\xi))(-\omega\varepsilon e^{-\alpha\xi^2})d\xi \tag{B.18}$$

where

$r_s = \sqrt{(x-x_s)^2 + (y-y_s)^2}$, and $r_s' = \sqrt{(x-x_s)^2 + (y+y_s)^2}$

B.4 Oscillatory Sink Flow

B.4.1 Steady Sink Flow

With respect to a polar coordinate system (r,θ) centered at (x_s,y_s), the nondimensionalized Euler equations are,

$$\frac{1}{r}\frac{\partial(\rho V r)}{\partial r} = \bar{s} \tag{B.19}$$

$$\frac{1}{r}\frac{\partial(\rho V^2 r)}{\partial r} + \frac{\partial p}{\partial r} = 0 \tag{B.20}$$

$$V\frac{\partial p}{\partial r} + \gamma p \frac{1}{r}\frac{\partial(Vr)}{\partial r} = \frac{\gamma p}{\rho}\bar{s} \tag{B.21}$$

where

$$\bar{s} = \begin{cases} -Q & r < r_s \\ -Qe^{-\sigma(r-r_s)^2} & r > r_s \end{cases} \tag{B.22}$$

These equations are non-dimensionalized by the following reference parameters: length by L (length scale), velocity by C_∞, density by ρ_∞, and pressure by $\rho_\infty C_\infty^2$. The source term satisfies the isentropic condition $p = \frac{1}{\gamma}\rho^\gamma$ and V is the radial velocity.

Equation B.19 can be integrated to give,

$$\rho V r \equiv F(r) = \begin{cases} -\dfrac{Qr^2}{2} & r < r_s \\ -\dfrac{Q}{2}[r_s^2 - \dfrac{1}{\sigma}(e^{-\sigma(r-r_s)^2} - 1) + r_s(\dfrac{\pi}{\sigma})^{\frac{1}{2}} erf(\sigma^{\frac{1}{2}}(r - r_s))] & r > r_s \end{cases} \tag{B.23}$$

where *erf*( ) is the error function.

By substitution of B.23 into B.20, a single equation for ρ can be found. This equation can be written in the form,

$$(\frac{F^2}{r^2\rho^2} - \rho^{\gamma-1})\frac{d\rho}{dr} = \frac{F}{\rho r^2}(2\frac{dF}{dr} - \frac{F}{r}) \tag{B.24}$$

For $r<r_s$, equation B.24 can be integrated in closed form to give,

$$r^2 = -\frac{8}{3(\gamma+\frac{1}{3})}\frac{\rho^{\gamma+1}}{Q^2} + c\rho^{\frac{1}{3}} \tag{B.25}$$

where c is the constant of integration.

For $r \to \infty$, equation B.24 can be integrated to yield the following asymptotic solution

$$\rho = 1 - \frac{F(\infty)^2}{2r^2} + \cdots \tag{B.26}$$

where $F(\infty) = Q/2\pi$.

To solve B.24 numerically for $r>r_s$, a straightforward way is to start at a large value of r using B.26 as the starting solution and integrate equation B.24 by Runge-Kutta method until $r=r_s$ is reached. Choose c of B.25 so that ρ matches the value of the numerical solution at $r=r_s$. With ρ determined, V and p can be found as,

$$V = \frac{F(r)}{r\rho} \quad \text{and} \quad p = \frac{1}{\gamma}\rho^{\gamma} \tag{B.27}$$

B.4.2 Acoustic wave solution associated with an oscillatory sink flow

Consider small amplitude acoustic disturbances generated by a time periodic source in the presence of a time independent sink flow. The governing equations are the linearized Euler equations. The solution may be written in the form

$$\begin{pmatrix} \rho' \\ V' \\ p' \end{pmatrix} = \mathrm{Re}\left\{ \begin{pmatrix} \hat\rho(r) \\ \hat V(r) \\ \hat p(r) \end{pmatrix} e^{-i\omega t} \right\} \tag{B.28}$$

where a prime denotes the perturbation variables and ω is the angular frequency of the source. On denoting the mean sink flow variables by overbar, the disturbance equations written in polar coordinates centered at the source location are

$$-i\omega\hat\rho + \frac{1}{r}(\bar\rho\hat v + \hat\rho\bar V) + \bar\rho\frac{d\hat v}{dr} + \bar V\frac{d\hat\rho}{dr} + \hat\rho\frac{d\bar V}{dr} = \varepsilon e^{-\alpha r^2} \tag{B.29}$$

$$\begin{aligned} -i\omega\bar\rho\hat v - i\omega\bar V\hat\rho + \frac{1}{r}(2\bar\rho\bar V\hat v + \hat\rho\bar V^2) + 2\bar\rho\bar V\frac{d\hat v}{dr} + 2\bar\rho\hat v\frac{d\bar V}{dr} + 2\bar V\hat v\frac{d\bar\rho}{dr} + \bar V^2\frac{d\hat\rho}{dr} \\ + 2\bar V\hat\rho\frac{d\bar V}{dr} = -(\bar\rho^{\gamma-1}\frac{d\hat\rho}{dr} + \bar\rho^{\gamma-2}\hat\rho\frac{d\bar\rho}{dr}) \end{aligned} \tag{B.30}$$

In deriving these equations, the isentropic relation has been used to eliminate $\hat p$ in favor of $\hat\rho$. Equations B.29 and B.30 are to be solved with the boundedness condition at *r*→*0* and the outgoing wave condition at *r*→∞.

For *r*→*0*, the mean flow solution can be expanded in a power series in the form,

$$\left.\begin{aligned} \bar V &= v_1 r + \cdots \\ \bar\rho &= \rho_0 + \rho_2 r^2 + \cdots \\ \bar p &= p_0 + p_2 r^2 + \cdots \end{aligned}\right\} \tag{B.31}$$

On substitution of B.31 into B.30, a power series solution of the acoustic disturbance which is bounded at *r*→*0* can be obtained in a straightforward way. The solution has the form

$$\left.\begin{aligned} \hat{\rho} &= \beta_0 + \beta_2 r^2 + \cdots \\ \hat{v} &= \lambda_1 r + \cdots \end{aligned}\right\} \tag{B.32}$$

where β_0 is arbitrary constant and

$$\beta_2 = -\{(2\frac{\gamma p_0}{\rho_0}\rho_2 - i\omega v_1 + 3v_1^2)\beta_0 - \frac{1}{2}(6v_1 - i\omega)[\varepsilon + (i\omega - 2v_1)\beta_0]\}\frac{\rho_0}{2\gamma p_0},$$

$$\lambda_1 = \frac{[\varepsilon + (i\omega - 2v_1)\beta_0]}{2\rho_0}$$

For $r \to \infty$, the mean flow quantities in B.30 may be replaced by the asymptotic sink flow solution of B.26. In this limit, the following asymptotic outgoing wave solution of B.29 and B.30 can be established after some algebra,

$$\lim_{r\to\infty}\begin{pmatrix}\hat{\rho}\\ \hat{V}\end{pmatrix} \to \begin{pmatrix}\tilde{\rho}\\ \tilde{V}\end{pmatrix} e^{i\omega(\Phi(r)-t)} \tag{B.33}$$

where

$$\Phi(r) = \int_{r_1}^{r} \frac{dr}{(\frac{\gamma\bar{p}}{\bar{\rho}})^{\frac{1}{2}} + \bar{V}} \tag{B.34}$$

$$\tilde{\rho} = A[\frac{1}{r^{\frac{1}{2}}} + (-\frac{i}{8\omega} + F(\infty))\frac{1}{r^{\frac{3}{2}}} + O(\frac{1}{r^{\frac{5}{2}}})] \tag{B.35}$$

$$\tilde{v} = A[\frac{1}{r^{\frac{1}{2}}} + (\frac{3i}{8\omega} + F(\infty))\frac{1}{r^{\frac{3}{2}}} + O(\frac{1}{r^{\frac{5}{2}}})] \tag{B.36}$$

and *A* is arbitrary constant.

To find the linearized acoustic wave solution numerically, one may use B.32 as a starting solution and integrate B.29 and B.30 outward using the Runge-Kutta method. Simultaneously use B.33-B.36 as the starting solution at $r=r_{max}$ where r_{rmax} is very large and integrate B.29 and B.30 inward. The two pieces of solution must match at some intermediate value of r. These matching conditions determine the two unknowns A and β_0. In this way, the exact numerical solution is found.

APPENDIX C

TROUTT & MCLAUGHLIN 2.1 MACH JET

Tam & Burton (1987) used analytical functions to fit the measured profile of the mean flow axial velocity in the three streamwise regimes of a supersonic jet: the potential core, transitional, and fully developed regimes. For the jet from Troutt & Mclaughlin (1982) experiment, the core region extends over the first five diameters of the jet. The developed region begins at about eight diameters downstream of the nozzle exit. A half-Gaussian curve is used to fit the velocity profile in the following form,

$$U(x,r)=\begin{cases} U_c(x) & r<h(x) \\ U_c(x)\,\exp[-(\ln 2)(\dfrac{r-h(x)}{b(x)})^2] & r\geq h(x) \end{cases} \tag{C.1}$$

where $U_c(x)$ is the centerline velocity, $h(x)$ is the radius of the uniform core and $b(x)$ is the half-width of the annular mixing layer, i.e. the radial distance from the outer edge of the uniform core to the half-velocity point. The velocity is normalized by the jet exit velocity U_j.

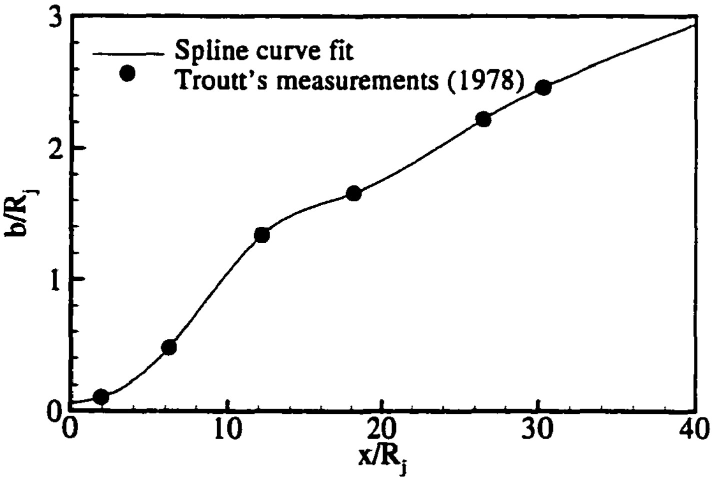

Figure C.1 Axial distribution of mean velocity profile parameter, b(x).

In the core region, the mean flow is uniform in the central part of the jet with $U_c(x)=1$ for $r<h(x)$. In the fully developed region, $h(x)=0$. As shown in figure C.1, a cubic spline curve is used to fit the axial distribution of $b(x)$ measured by Troutt (1978).

The property of momentum-flux conservation is used in the following form,

$$\int_0^\infty \rho U^2 r dr = \frac{1}{2} \tag{C.2}$$

where the density is normalized by the exit centerline density and distances by the nozzle radius. In the core region, since both $U_c(x)$ and $b(x)$ are known, this relation is used to obtain $h(x)$. In the fully developed region, since both $h(x)$ and $b(x)$ are known, the constant axial flux equation is used to obtain $U_c(x)$. For the transitional region, $b(x)$ and $h(x)$ are obtained using cubic spline fit that matches the values of $b(x)$ and $h(x)$ and their derivatives at the two ends of the region.

Invoking boundary-layer type approximation to the mean flow equations shows that mean flow pressure can be taken to be uniform in the jet. Under such assumption, the continuity equation for axisymmetric flow is,

$$\frac{\partial V}{\partial r} + \frac{V}{r} + \frac{\partial U}{\partial x} = 0 \tag{C.3}$$

From which, the radial velocity is obtained as,

$$V(r) = -\frac{1}{r}\int_0^r \frac{\partial U}{\partial x} r' dr' \tag{C.4}$$

The total temperature is assumed constant, which is used to obtain the static temperature profile in terms of the velocity as follows:

$$T = 1 + \frac{\gamma-1}{2} M_j^2 - \frac{\gamma-1}{2} M_j^2 U^2 \tag{C.5}$$

where temperature and velocity is normalized by jet exit conditions. The equation of state is then used to obtain the density profile in terms of temperature profile,

$$\rho=\frac{1}{T} \tag{C.6}$$

APPENDIX D
TURBULENCE MODEL

The mixing length model constants C_l and C_2 are given by the following relations (from Dahl and Morris, 1997),

$$C_1 = \frac{A + B\sqrt{\alpha} + C\alpha}{(1+\sqrt{\alpha})(1+\beta\sqrt{\alpha})} \quad \text{(D.1)}$$

where

$\alpha = \rho_2 / \rho_1$ is the density ratio across the shear layer,

$\beta = U_2 / U_1$ is the velocity ratio across the shear layer,

For $\beta < 1$: $A = 10^{-2} \times (6.5919 + 11.918\beta - 4.1855\beta^2)$

$B = 10^{-2} \times (10.88 - 2.3578\beta + 6.5642\beta^2)$

$C = 10^{-2} \times (3.1013 + 16.42\beta - 5.8217\beta^2)$

For $\beta > 1$: $A = 10^{-3} \times (101.95 + 51.507\beta - 1.6\beta^2)$

$B = 10^{-3} \times (60.287 + 75.16\beta + 1.3818\beta^2)$

$C = 10^{-4} \times (723.97 + 753.34\beta - 6.2101\beta^2)$

$$C_2 = 1 + 0.4959[\exp(-1.4593M_c^2 + 0.0427M_c^3 - 0.3658M_c^4) - 1] \quad \text{(D.2)}$$

where

M_c is the convective Mach number defined by,

$$M_c = M_1 \frac{\sqrt{\alpha}\,|1-\beta|}{1+\sqrt{\alpha}} \quad \text{(D.3)}$$

APPENDIX E

ENVIRONMENTAL ACOUSTICS TERMINOLOGY

E.1 Sound Pressure Level

Although sound pressure amplitudes can be measured, it is customary in many contexts to measure and report a quantity varying linearly as the logarithm, base 10, of the mean squared pressure. This quantity is the *sound pressure level* and is defined by

$$SPL = 10 \log \frac{\overline{p}^2}{p_{ref}^2} \qquad \text{(E.1)}$$

The resulting number has the units of *decibels* (dB). The denominator factor p_{ref} represents a reference pressure, which is usually taken as 2×10^{-5} Pa for airborne sound.

E.2 A-weighted Sound Pressure Level

The simplest and probably most widely used measure of environmental noise is the A-weighted sound pressure level SPL_A, expressed in dBA. A-weighting assigns to each frequency a "weight" that is related to the sensitivity of the ear at that frequency. The frequencies to which the human ear is less sensitive are weighted less than those to which the ear is more sensitive. This weighting is intended to be such that sounds of different frequencies giving the same decibel reading with A-weighting would be equally loud. The frequency-weighted mean squared pressure $\overline{p}_A^2$ is obtained as,

$$\overline{p}_A^2 = \sum_{n=1}^{N} W(f_n)\overline{p}_n^2 \qquad \text{(E.2)}$$

where $W(f_n)$ is the weighting function at frequency f_n. The weighting functions are obtained from the curve in figure E.1 (the curve spans the audible frequency range from 20 Hz to 20 kHz).

$$W(f) = 10^{\Delta L_A(f)/10} \tag{E.3}$$

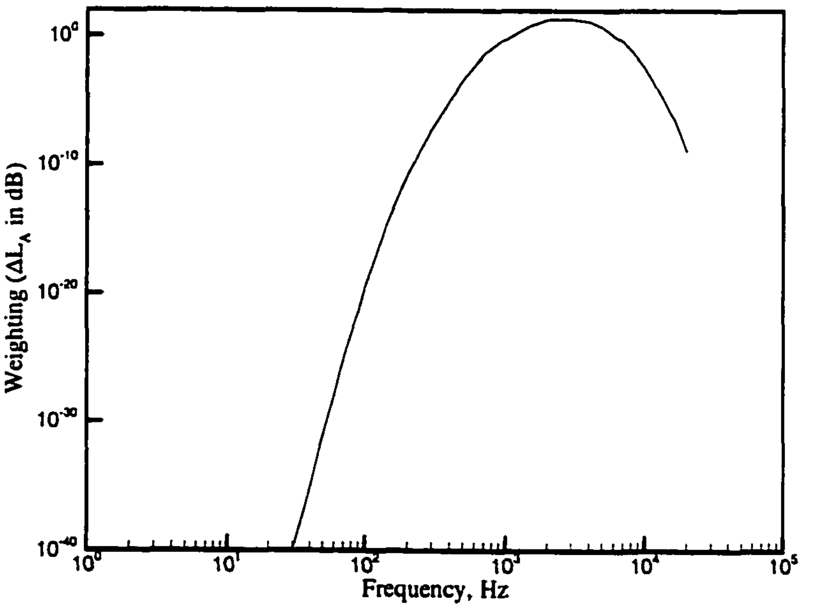

Figure E.1 Weighting function for A-weighted sound pressure level.

VITA

Moumen Idres was born in Egypt on November 18, 1969. He joined the Aerospace Engineering Department at Cairo University in 1987. In 1992, he earned a Bachelor of Science degree with distinction. After graduation, Mr. Idres joined the Aerospace faculty at Cairo University as an instructor. He worked in the field of propulsion with Prof. Ali Hashem and Prof. Mohammed Shabaka. In 1995, he received his Master's degree from the Aerospace Department, Cairo University.

In 1996, Mr. Idres joined the Aerospace Department at Old Dominion University as a research assistant. He worked in the field of aeroacoustics under the supervision of Prof. Oktay Baysal. He anticipates completing all the requirements for the Ph.D. in Engineering Mechanics by December of 1999. Following graduation, Mr. Idres will occupy a postdoctoral position in the Engineering Science and Mechanics Department at Virginia Polytechnic Institute of Technology, Blacksburg, Virginia. There, he will work closely with Prof. Ali Nayfeh.